# The Impact of Ice Coverage on the Tidal Water Motion in Estuaries: a 2DV Modeling Study

**Bradley van Hooff**

A thesis presented for the degree of Master of Science in Applied Mathematics.

To be defended publicly on Monday September 15, 2025 at 16:00 (UTC+2).

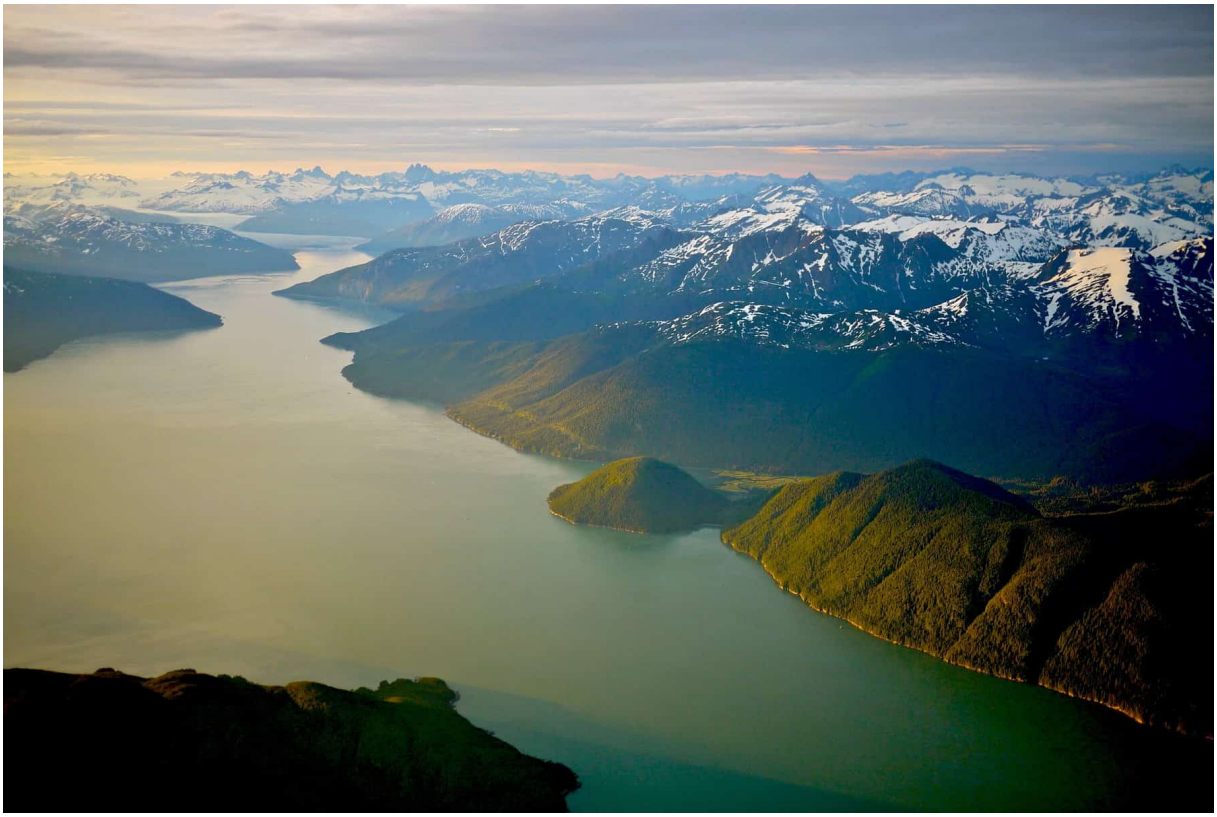

DIAM
TU Delft
The Netherlands

| | | |
|---|---|---|
| Student number: | 5348803 | |
| Thesis committee members: | Dr. H.M. Schuttelaars | TU Delft (DIAM), *supervisor* |
| | Dr. ir. M. Verlaan | Stichting Deltares, *supervisor* |
| | Dr. ir. J.H. Weber | TU Delft (DIAM) |

The source for the front page's picture is: Alaska (2025). It is a picture of Cook Inlet.

# Summary

An estuary is a semi-enclosed coastal body of water, having both a free connection to the open sea and a connection to fresh water coming from land-regions. Cook Inlet is an estuary in Alaska, and a major part of the Alaskan citizens live near its shores. The inlet is an important shipping route for oil, gas and petroleum products, and the port of Anchorage, near the head of the estuary, serves approximately 80% of the Alaskan population.

The tidal waves and currents in Cook Inlet can be quite strong. To ensure the safety of local communities and to assess the risks of the transport of goods and raw materials through Cook Inlet, it is important that the local water velocity and tidal currents can be predicted. However, Cook Inlet is often covered by ice, and the influence of ice on the tidal water motion is not thoroughly investigated yet. The ice cover varies seasonally, and with climate change, these variations will be even larger. To increase our understanding of the influence of ice on the tidal water motion in high-latitude estuaries such as Cook Inlet, this thesis will focus on modelling and analysing the ice-water interaction within estuaries. To investigate the most important processes that determine the ice-water interactions, an idealised modelling approach is used.

In estuaries, one generally distinguishes two types of ice: landfast ice, and ice floes. Landfast ice is a stationary type of ice that finds itself on the surface of the estuary. This type of ice causes a frictional force at the interface between the water and the ice. Ice floes are drifting sheets of ice, that interact with both the water and each other. In this thesis, we focus on the effect of ice floes that drift relatively freely, so that the interaction between floes is negligible, and their velocity is close to the velocity of the water.

The effect of landfast ice and ice floes on the water motion are analysed separately, and the time-dependency of both model both models is solved by a Fourier/method. The model for landfast ice allowed for analytical solutions to be found under the assumption of and exponentially converging estuary-width and a constant estuary-depth. Using these analytical solutions, the effect of the percentage of landfast ice coverage in general estuaries is analysed. This analysis led to the conclusion that landfast ice covers can either increase or decrease the height of tidal waves, depending on the length of the estuary and the convergence of its width.

The model for ice floes without vertical stresses cannot be solved analytically, since the horizontal viscosity can no longer be neglected due to the presence of ice floes. As a first step, the depth is assumed to be constant. In the numerical solution method, the vertical structure of the longitudinal water velocity is approximated by depth-dependent eigenfunctions. The surface level and amplitudes of the eigenfunctions, which vary over the longitudinal coordinate, are solved using a finite difference method. The effect of the percentage of ice floe coverage in general estuaries is analysed using these approximations. It is found that an increased ice cover could either attenuate or amplify the waterlevel, depending on the length of the estuary.

# Acknowledgements

I want to thank my daily supervisors Henk Schuttelaars and Martin Verlaan, for helping me with the project. Also, my thanks to Steve Dykstra for proposing the project, and for listening to my presentations.

Thank you to all the friends I made in Mathematics, for studying with me and for having fun as well! Also, I am thankful for all the friends I made in DSZ WAVE!

Furthermore, I want to express my gratitude towards Stichting Deltares for taking me in as an intern.

And I want to say thank you to George Schramkowski and Yoeri Dijkstra for answering my questions when I had them!

Lastly, I want to thank my family for supporting me!!

# Contents

# Chapter 1

# Introduction

## 1.1 Estuaries

An estuary is a semi-enclosed coastal body of water, having both a free connection to salt water from the open sea and to fresh water coming from landward regions (Pritchard, 1967). Cook Inlet is an example of an estuary, and is situated in Alaska (see Figure 1.1). The port of Anchorage, which finds itself near the northern end of this inlet, is Alaska's largest commercial, industrial, recreational and transportational center. The estuary serves year-round as a shipping route for oil, natural gas and petroleum products. Approximately 80% of Alaska's population and its four largest military bases are served through Anchorage's port. Furthermore, the behaviour of the tidal water motion in Cook Inlet is quite unique. At the port of Anchorage, the height of the tidal waves can reach up to 9 meters, and tidal currents can be twice as strong as typical tidal currents (Mulherin et al., 2001, p.2), making Cook Inlet the estuary with the world's second most extreme tidal variations.


Figure 1.1: A map of Alaska, with the estuary Cook Inlet indicated in the southern parts (Guide, 2025).

Since approximately half of Alaska's population resides near its shores (Mulherin et al., 2001, p.2), being able to predict flood risks is of the utmost importance for the safety of the Alaskan society. Therefore, accurate predictions of only the waterlevel and of the strength and direction of tidal currents is essential. Furthermore, these water motions greatly influence local ecologies, both through natural processes and in combination with human interference. For example, the transport of oil and gas through Cook Inlet poses a threat for local ecologies, communities and the Alaskan economy, as shown by the Exxon Valdez oil spill in 1989 (see Figure 1.2). In order to accurately assess the risk of transporting oil and gas through estuaries such as Cook Inlet, one has to be able to predict the behaviour of the water-driven transport of particulate matter. To be able to do so, an understanding of the processes influencing the large-scale water motion is necessary.

Figure 1.2: The Exxon-Valdez oil spill in 1989, having major consequences for the local communities, ecology and economy (HISTORY, 2025).

## 1.2 Ice in Estuaries

The tidal motion in estuaries at higher latitudes such as Cook Inlet, is influenced by the coverage of ice. In Cook Inlet, this ice coverage can range from about 10% to 50% in the coldest months of the year (see Figure 1.4). In estuaries, one often distinguishes three types of ice: landfast ice, ice floes in the vertical shear region and ice floes in the horizontal shear region, (see Figure 1.5). Landfast ice is stationary and attached to the shore, and ice floes are defined as sheets of ice that float on the surface of the estuary's water. In the vertical regions, ice floes are close together and exert strong stresses on each other, so that the velocity of the ice floes decreases, causing a strong vertical shear stress within the underlying water. In the horizontal shear region, the floes are drifiting more freely, having little to no interaction. In this region, their velocity is close to the water's velocity, so that the vertical shear stress is negligible (Vasulkar, 2024, p.75-77).

With climate change, the ice coverage in high-latitude coastal systems such as Cook Inlet is prone to change and become more variable (Overeem et al., 2022). While the effect of ice on oceanic water motions has been studied intensively, its effect on tidal water motions within estuaries remains poorly investigated (Irrgang et al., 2022). Therefore, this thesis aims to make improve our understanding of the effects of ice on watermotion in high-latitude estuaries.

## 1.3 Idealised Modelling Approach

Mathematical models describing geophysical processes, such as the dynamic behaviour of water in estuaries, can be classified from complex, simulational models to highly simplified, exploratory models (Murray, 2003, p.1). The simulational models are focused on creating quantitatively accurate results, and are created to duplicate systems as thoroughly as possible. These models are generally computationally expensive, and require an extensive calibration of parameters. Such models are not well-suited for exploring the processes and interactions within a poorly investigated phenomenon, such as the effect of ice on tidal motions in estuaries. Indeed, the calibration of parameters in simulation models can be shown to be accurate for the situation without ice, but it is not abvious that these parameters are still optimal when ice is introduced (Schuttelaars et al., 2013, p.71). However, changing the parameters systematically over a wide range of values is not feasible for the complex models, due to their computationally expensive nature.

On the other hand, the aim of highly simplified, exploratory models is to find a clear and transparent explanation for poorly understood physical phenomena. This is acheived by including only those processes that are deemed essential to reproduce the aspects of interest (Murray, 2003, p.1). Due to the simplicity of the models, computational times can be much shorter than in simulational models, allowing for the parameter values to be varied over a large range of values in a systematic way. Since the effect of ice on the tidal water motion in high-latitude estuaries is still poorly investigated, this thesis uses an idealised modelling approach to distinguish the important features of ice-water interactions in high-latitude estuaries.

## 1.4 Research Questions

The focus of this thesis will lie in answering the following questions:

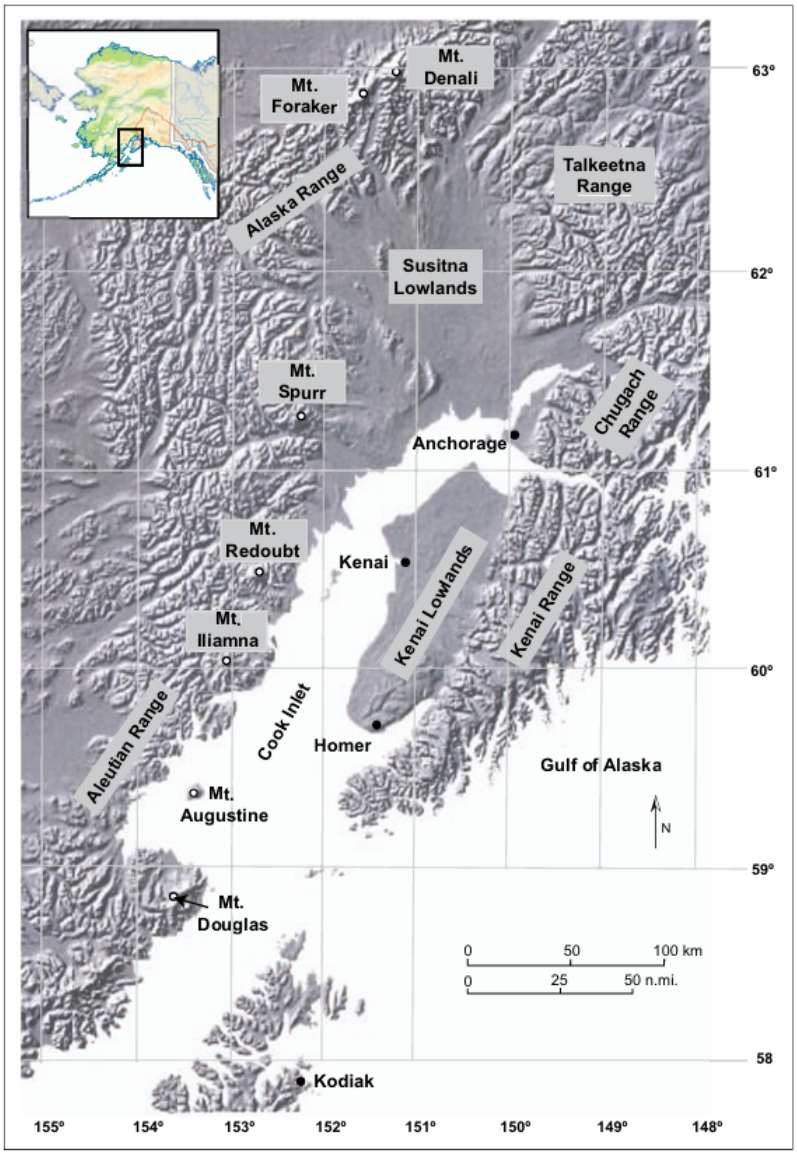


Figure 1.3: A bird's eye view of Cook Inlet and the surrounding area (Mulherin et al., 2001, p.4).

1. What are the important physical processes that influence the large-scale longitudinal hydrodynamics (i.e. water motion) in an estuary?
2. How can we include landfast ice and ice floes in the horizontal shear region parametrically in our idealised model?
3. How does landfast ice influence an estuary's hydrodynamics?
4. How do ice floes in the horizontal shear region influence an estuary's hydrodynamics?

## 1.5 Outlook

The above questions will be answered in the upcoming chapters. First of all, in Chapter 2, a model is developed that parametrically includes the influence of landfast ice and ice floes on the large-scale water motion, with a focus on describing the important physical processes. To allow the analysis of landfast ice and ice floes in the horizontal shear zone separately, two models in which these effects are isolated are developed in Chapter 3. Chapter 4 describes the solution methods that are used to derive the solutions and approximations to these models. In Chapter 5, the properties and parameter-sensitivities of the solution to the model without ice are analysed. With this knowledge, Chapter 6 analyses the effect of landfast ice on the estuary's water motion. Then, Chapter 7 discusses the effect of ice floes in the horizontal shear region. Finally, Chapter 8 will summarise all conclusions drawn from these results, and provide an overview of future work that is deemed useful within this research topic.

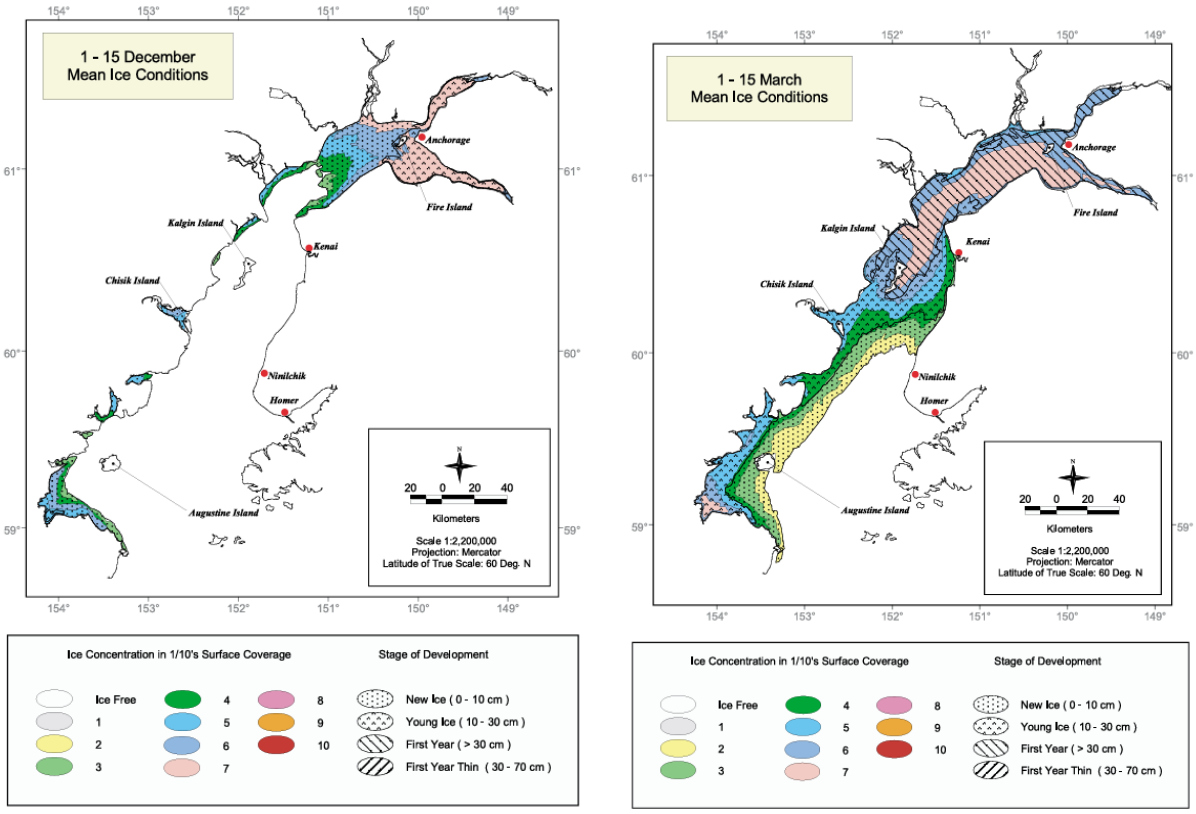


(a) An ice coverage of about 10% in the first half of December.

(b) An ice coverage of about 10% in the first half of March.

Figure 1.4: The mean ice coverage and development stage in Cook Inlet for given time periods (Mulherin et al., 2001, p.26-34).

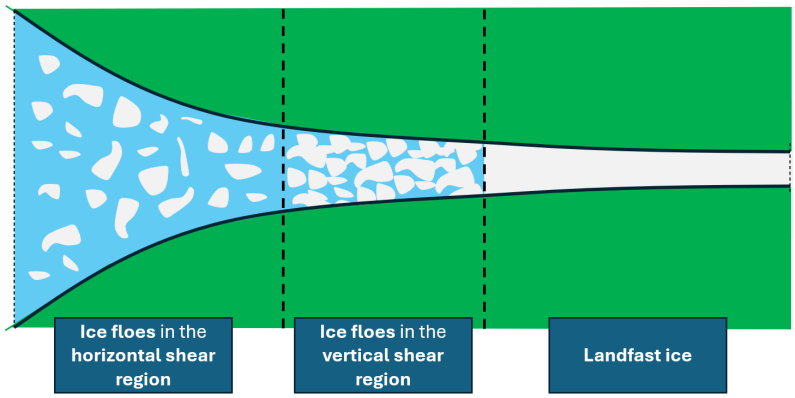


Figure 1.5: The three types of ice that are distinguished in Cook Inlet. Ice is given a white colour.

# Chapter 2

# The Width- and Reynolds-Averaged Shallow-Water Equations Including Landfast Ice and Ice Floes

In this chapter, an idealised model describing the influence of both landfast ice and ice floes on the longitudinal and vertical velocity profiles and weterlevel within an estuary is presented. The model is attained by deriving the width- and Reynolds-averaged Shallow Water Equations, and including landfast ice and ice floes. Special attention is paid to the assumptions and conditions for validity of the equations, allowing for an understanding of the physical assumptions made in deriving of the equations and helping to build a framework in which the results of upcoming chapters can be interpreted.

To derive the width- and Reynolds-Averaged Shallow Water equations, one starts with the Navier-Stokes equations, which are based on merely the physical principles of mass- and momentum balances (assuming that water can be modelled as a continuous medium). In section 2.1 slightly simplified form of the Navier-Stokes Equations is taken as the starting point of the model description, after which a Reynolds-averaging procedure is applied, allowing us to focus on the large-scale hydrodynamics. In section 2.2, the assumption of hydrostatic pressure is discussed and in section 2.3, the equations are averaged over the estuary's width, leading to a two-dimensional set of equations. In section 2.4, the consequences of only modelling the core region of the flow are discussed. Subsequently, in section 2.5, the parametrisations for landfast ice and ice floes are introduced. Lastly, the boundary conditions that are required to complete the model are given in section 2.6.

## 2.1 Navier-Stokes Equations

Typically, in modelling the dynamics of water motion, water is considered to be a Newtonian fluid. Furthermore, incompressibility is usually assumed, density-variations in all terms except the pressure- and gravitational term (the Boussinesq-assumption) are neglected, and the reciprocal Coriolis-forces are neglected. The Navier-Stokes Equations under these assumptions read:

$$\begin{cases} u_x + v_y + w_z = 0, & \text{(2.1a)} \\ u_t + uu_x + vu_y + wu_z = fv - \dfrac{1}{\rho_0} p_x + \nu(u_{xx} + u_{yy} + u_{zz}), & \text{(2.1b)} \\ v_t + uv_x + vv_y + wv_z = -fu - \dfrac{1}{\rho_0} p_y + \nu(v_{xx} + v_{yy} + v_{zz}), & \text{(2.1c)} \\ w_t + uw_x + vw_y + ww_z = -\dfrac{g\rho}{\rho_0} - \dfrac{1}{\rho_0} p_z + \nu(w_{xx} + w_{yy} + w_{zz}). & \text{(2.1d)} \end{cases}$$

Here, we defined the following variables, which are used to describe the hydrodynamics in the Navier-Stokes equations.

- $\mathbf{u}(x,y,z) = \begin{bmatrix} u(x,y,z) \\ v(x,y,z) \\ w(x,y,z) \end{bmatrix}$ is the velocity vector, describing the velocities in the longitudinal, lateral and vertical directions, respectively, in meters per second.
- $\rho(x,y,z)$ denotes the density of the water in kilogram per cubic meter.

- $p(x, y, z)$ gives the local pressure in Pascal (Newton per square meter).
- $f := 2\Omega^z = 2\Omega \sin(\varphi)$ is the Coriolisparameter in Newton per kilogram (Cushman-Roisin and Beckers, 2011, p.49). Here, $\varphi$ is the latitude.

Since we are mostly interested in gaining insight in the longitudinal hydrodynamics, we model the estuary as if it had a straight middle-axis, which we denote by the $x$-axis. This axis runs from the sea to the riverine side. The (vertical) $z$-axis is pointed upwards, so that the (lateral) $y$-axis points to the right with respect to the $x$-axis; see Figure 2.1 for a schematic overview. As shown in this figure, the longitudinal coordinate $x$ varies between $x = 0$ at the seaside and $x = L$ at the riverside. The lateral coordinate $y$ varies between $y = B_1(x)$ and $y = B_2(x)$. We define the width as $\Delta(x) := B_2(x) - B_1(x)$. The vertical coordinate $z$ varies between $z = -H(x) - z_0$ and the free surface at $z = \zeta(x, y, t)$. Note that the free surface level $\zeta$ is an unknown and follows from the internal dynamics.

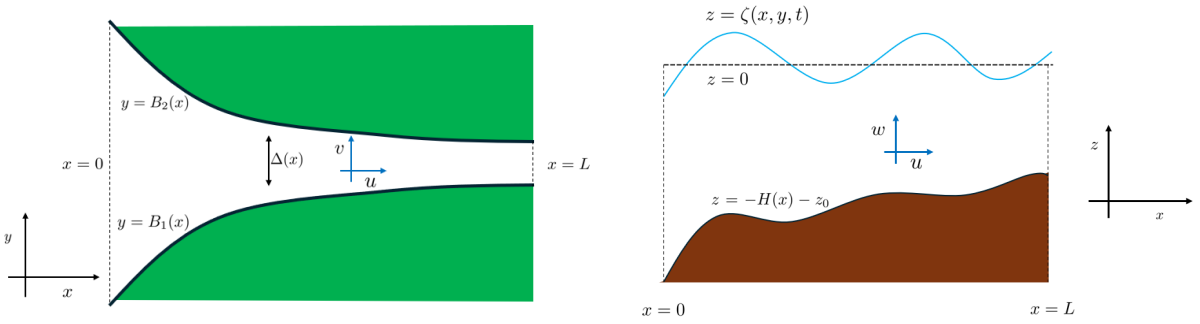


(a) A top-view.

(b) A side-view.

Figure 2.1: A top-view (a) and a side-view (b) of the estuary considered. For an explanation of the symbols, see the main text.

To focus on the large-scale water flow without solving the small-scale turbulent processes, a *Reynolds-averaging* is applied to the equations. The Reynolds-average of the velocity field is defined as a so-called *ensemble average*, making use of the statistical character of turbulence (Nieuwstadt et al., 2016, p.76):

$$\langle \mathbf{u} \rangle (x, y, z, t) := \lim_{N \to \infty} \frac{1}{N} \sum_{1=1}^{N} \mathbf{u}^{(\mathbf{i})}(x, y, z, t), \tag{2.2}$$

where $\left(\mathbf{u}^{(\mathbf{i})}\right)_{i=1}^{\infty}$ are experiments with the same inital conditions and under the same external forces. Using this average, one can derive the Reynolds-averaged Navier-Stokes Equations (see Appendix A.1).

Due to the nonlinear advection-terms, the effect of turbulence on the Reynolds-averaged flow is shown by the *correlation terms*. To turn the model into a set of solvable differential equations, we must either set up a new set of equations describing the turbulent motion ($u_i'$, $i = 1, 2, 3$), or introduce a closing hypothesis that parametrises the turbulent effects on the Reynolds-averaged velocity field. Since our aim is to create a simpler model rather than a more complex one, we decide upon the second option, and do so by applying the *Boussinesq closure hypothesis*. This hypothesis uses the empirical knowledge that the main effect of turbulence in liquids is dissipation, and therefore the turbulent influence is modelled as a viscous effect: the *eddy viscosity* (Cushman-Roisin and Beckers, 2011, p.93). Furthermore, for this hypothesis to be applicable, the length-scales on which eddies develop must be much smaller than the length-scales upon which the Reynolds-averaged velocity field varies. Thus, letting $\mathcal{L}$ and $\mathcal{H}$ denote the length-scales for the horizontal and vertical eddies, and $L_0$ and $H_0$ the length-scales for the vertical and horizontal dimensions of the estuary, we require that (Nieuwstadt et al., 2016, p.84)

$$\frac{\mathcal{L}}{L_0} \ll 1 \quad \text{and} \quad \frac{\mathcal{H}}{H_0} \ll 1. \tag{2.3}$$

Turbulent motions in the horizontal plane cover a much larger distance than in the vertical direction, and therefore, the dissipative effect of turbulence in the horizontal direction is much larger than in the vertical one. This leads to a distinction between the *horizontal eddy viscosity* $A_{\mathrm{h}}(x, y, z, t)$ and the *vertical eddy viscosity* $A_{\mathrm{v}}(x, y, z, t)$, where $A_{\mathrm{h}}(x, y, z, t) \gg A_{\mathrm{v}}(x, y, z, t)$ (Cushman-Roisin and Beckers, 2011, p.93). Now, we define $\mathcal{A}_{\mathrm{h}} := A_{\mathrm{h}} + \nu$ en $\mathcal{A}_{\mathrm{v}} := A_{\mathrm{v}} + \nu$,

which leads to the following **Reynolds-Averaged Navier-Stokes Equations**.

$$\begin{cases} u_x + v_y + w_z = 0, & \text{(2.4a)} \\ u_t + \left(u^2\right)_x + (vu)_y + (wu)_z = fv - \dfrac{1}{\rho_0} p_x + (\mathcal{A}_{\mathrm{h}} u_x)_x + (\mathcal{A}_{\mathrm{h}} u_y)_y + (\mathcal{A}_{\mathrm{v}} u_z)_z, & \text{(2.4b)} \\ v_t + (uv)_x + \left(v^2\right)_y + (wv)_z = -fu - \dfrac{1}{\rho_0} p_y + (\mathcal{A}_{\mathrm{h}} v_x)_x + (\mathcal{A}_{\mathrm{h}} v_y)_y + (\mathcal{A}_{\mathrm{v}} v_z)_z, & \text{(2.4c)} \\ w_t + (uw)_x + (vw)_y + \left(w^2\right)_z = -\dfrac{g\rho}{\rho_0} - \dfrac{1}{\rho_0} p_z + (\mathcal{A}_{\mathrm{h}} w_x)_x + (\mathcal{A}_{\mathrm{h}} w_y)_y + (\mathcal{A}_{\mathrm{v}} w_z)_z. & \text{(2.4d)} \end{cases}$$

Here, the ensemble averaging symbol $\langle \cdot \rangle$ is omitted for readability.

## 2.2 Hydrostatic Pressure

As a next step in simplifying the model euations, hydrostatic pressure is assumed. For this assumption to be valid, the following requirements must be satasfied (Pedlosky, 2013, p.57-63).

1. The influence of stratification on the estuary's water motion is negligible.
2. Horizontal variations happen over a much larger length-scale than in the vertical direction,[1] i.e.

$$\frac{H_0}{L_0} \ll 1. \tag{2.5}$$

Under these assumptions, the local pressure can be approximated by

$$p(x, y, z) = \int_z^\zeta \rho(x, y, \hat{z})\, d\hat{z}, \tag{2.6}$$

leading to the so-called **Reynolds-Averaged Shallow-Water Equations**

$$\begin{cases} \partial_x u + \partial_y v + \partial_z w = 0, & \text{(2.7a)} \\ u_t + \left(u^2\right)_x + (vu)_y + (wu)_z = fv - \dfrac{g}{\rho_0} \left( \displaystyle\int_z^\zeta \rho\, d\hat{z} \right)_x + +(\mathcal{A}_{\mathrm{h}} u_x)_x + (\mathcal{A}_{\mathrm{h}} u_y)_y + (\mathcal{A}_{\mathrm{v}} u_z)_z, & \text{(2.7b)} \\ v_t + (uv)_x + \left(v^2\right)_y + (wv)_z = -fu - \dfrac{g}{\rho_0} \left( \displaystyle\int_z^\zeta \rho\, d\hat{z} \right)_y + (\mathcal{A}_{\mathrm{h}} v_x)_x + (\mathcal{A}_{\mathrm{h}} v_y)_y + (\mathcal{A}_{\mathrm{v}} v_z)_z & \text{(2.7c)} \end{cases}$$

## 2.3 Width-Averaging

In order to further simplify the model, without losing the depth-dependency - which may prove insightful in modelling the effects of ice layers on the water's surface - we average the model over the width. For this, we assume that *lateral variations have a negligible effect on the general behaviour of the width-averaged hydrodynamics in the vertical and longitudinal direction.* This leads to, among others, the assumption that the width-averaged lateral velocity component vanishes:

$$\{v\} = 0, \tag{2.8}$$

where, $\{\cdot\}$ denotes the width-averaging operator, defined by:

$$\{\cdot\}: \quad \{\alpha : K \times [0, \infty) \text{ s.t. } K \subset \mathbb{R}^3 \text{ is bounded and } \alpha < \infty\} \to \{\alpha : K \times [0, \infty) \text{ s.t. } K \subset \mathbb{R}^2 \text{ is bounded and } \alpha < \infty\},$$

$$\{\alpha\}(x, z, t) := \frac{1}{\Delta(x)} \int_{B_1(x,z)}^{B_2(x,z)} \alpha(x, y, z, t) dy.$$

We furthermore assume that the influence of the lateral momentum balance is not of significant importance. These approximations are valid if the following two requirements are satisfied (Ianniello, 1977, p.758).

1. The Coriolis terms must be of negligible importance. This is the case if the *Kelvin number* is small, i.e.

$$K_E := \frac{f\Delta}{\sqrt{gH}} \ll 1. \tag{2.9}$$

[1] For Cook Inlet, the depth of the estuary is of the order of ten of meters, i.e. $H_0 = \mathcal{O}(10)$ m, while the length is of the order of hundreds of kilometers, i.e. $L_0 = \mathcal{O}(10^5)$ m. Thus, in Cook Inlet, $\frac{H_0}{L_0} \sim 10^{-4}$.

2. The importance of the lateral velocity in the lateral momentum balance has to be negligible. This is satisfied if the *horizontal aspect ratio* $\delta$ is small ($\delta^2 \ll 1$), where

$$\delta := \frac{\sigma\Delta}{\sqrt{gH}}. \tag{2.10}$$

This allows us to focus on the (width-averaged) continuity equation and longitudinal momentum balance. A detailed description width-averaging procedure can be found in Appendix A.2.2. The form of the Reynolds- and Width-Averaged Shallow Water Equations that we will use is given by

$$\begin{cases} u_x + w_z + \dfrac{\Delta_x}{\Delta} u = 0, & \text{(2.11a)} \\ u_t + uu_x + wu_z + g\zeta_x + \dfrac{g}{\rho_0}\displaystyle\int_z^\zeta \rho_x \, d\hat{z} = \left(\hat{\mathcal{A}}_{\mathrm{h}} u_x\right)_x + \left(\hat{\mathcal{A}}_{\mathrm{v}} u_z\right)_z, & \text{(2.11b)} \end{cases}$$

where the width-averaging symbol $\{\cdot\}$ is omitted for readability. In deriving these equations, we have used that:

1. the walls at $y = B_1(x)$ and $y = B_2(x)$ are impermeable, i.e.

$$\mathbf{u} \cdot \begin{bmatrix} -B_i' \\ 1 \\ 0 \end{bmatrix} = 0 \quad \text{for} \quad y = B_i(x) \quad \text{with} \quad i = 1, 2; \tag{2.12}$$

2. the influence of the pressure and the eddy viscosity at the lateral boundaries are assumed to be negligible.

## 2.4 Modeling the Core Region

The water-flow along a boundary can be divided into multiple layers, of which the most important are: The core region, the wall region and the viscous sublayer (see Figure 2.2). In the wall region, eddies are smaller than in the core-regoin; in the viscous sublayer, the influence of turbulence is much smaller than the influence of viscosity (Nieuwstadt et al., 2016, p.89-94).[2]

Since the thickness of the viscous sublayer and the wall region are much smaller than the core region, we will focus on the hydrodynamics in the core region. To do so, we must introduce a boundary condition that finds itself at the top of the wall layer. This is often done through a parametrisation of the shear stress, given by the so-called *quadratic bottom stress*:

$$\tau_{\mathrm{bottom},x} = \rho_0 c_d |u| u, \quad \text{at} \quad z = -H(x), \tag{2.13}$$

where $-H(x)$ is now the $z$-coordinate at the top of the wall layer (see Figure 2.2), and $c_d$ is the *drag coefficient*. To further simplify our model, we linearise this condition, leading to the so-called *partial-slip condition*:

$$\tau_{\mathrm{bottom},x} = s_F u, \tag{2.14}$$

where $s_F$ is the *bottom friction coefficient*. This linearisation was first implemented by H.A. Lorentz, who applied an iterative process to update the bottom friction coefficient $s_F$, leading to qualitatively fitting predictions of the tidal flow in the Waddenzee (De Swart, 2009, p.40). We will, however, not apply this itarative process, but leave $s_F$ constant. Since in our model, the shear stress is parametrised as $\tau_x = \hat{\mathcal{A}}_{\mathrm{v}} \partial_z u$, we find the following expression for the partial-slip condition near the bottom:

$$\hat{\mathcal{A}}_{\mathrm{v}} u_z = s_F u \quad \text{for} \quad z = -H(x). \tag{2.15}$$

The value of the eddy viscosity scales with the size $\mathcal{L}$ of the eddies and the flow velocity $\mathcal{U}$ within the eddies (Nieuwstadt et al., 2016, p.84):

$$\hat{\mathcal{A}}_{\mathrm{v}} \propto \mathcal{L}\mathcal{U}. \tag{2.16}$$

The eddy viscosity decreases as the flow nears the bottom (or a wall), since the eddies get smaller. Also, near the water surface, it is expected to be smaller than in the core of the flow (Ianniello, 1977, p. 759). Since we are interested in the qualitative behaviour of the current, the vertical eddy viscosity is taken to be independent of the depth, which will simplify our mathematical analysis (De Swart, 2009, p.22). Thus, from now on, $\hat{\mathcal{A}}_{\mathrm{v}}$ is considered to be a constant parameter, both in time and space.

[2] An estimate of the thickness of the combination of the viscous sublayer and the wall layer is given by $100 \cdot \nu/u_*$ (Nieuwstadt et al., 2016, p.94), where $u_*$ is the wall friction velocity (Nieuwstadt et al., 2016, p.88). The order of magnitude of the kinematic viscosity of water is given by $\nu \sim 10^{-12}$ m$^2$/s (Batchelor, 2000, p.597). $u_* = \sqrt{\frac{\tau_s}{\rho_0}}$, with $\tau_s$ is the wall friction stress (Nieuwstadt et al., 2016, p.88). The density is $\rho_0 \sim 10^3$ kg/m$^3$ (Batchelor, 2000, p.597).

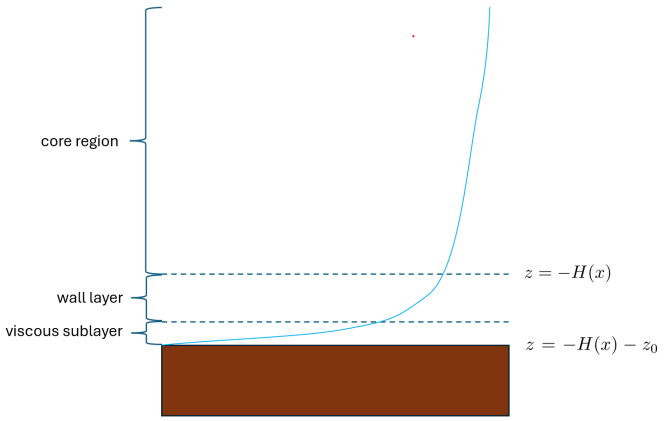


Figure 2.2: The three layers in which the sizes of eddies are notably different.

## 2.5 Modelling Ice

Figure 2.3 shows three ice-covered regions, as already meantoned in the introduction (Chapter 1): a region with landfast ice (right), a region with ice floes floating relatively freely, which we call the horizontal shear region (left), and a region in which ice has a strong internal friction, which we call the vertical shear region (middle). According to Vasulkar (2024, p.5), in the horizontal shear region, the vertical stresses are small compared to the horizontal shear, so that the vertical stresses do not influence the ice-water interaction considerably and can be neglected. In the vertical shear region, however, the vertical stresses are larger due to the interactions between ice floes. Therefore, vertical shears can not be neglected in this region. As a start, we focus on modelling ice floes in the horizontal shear region.

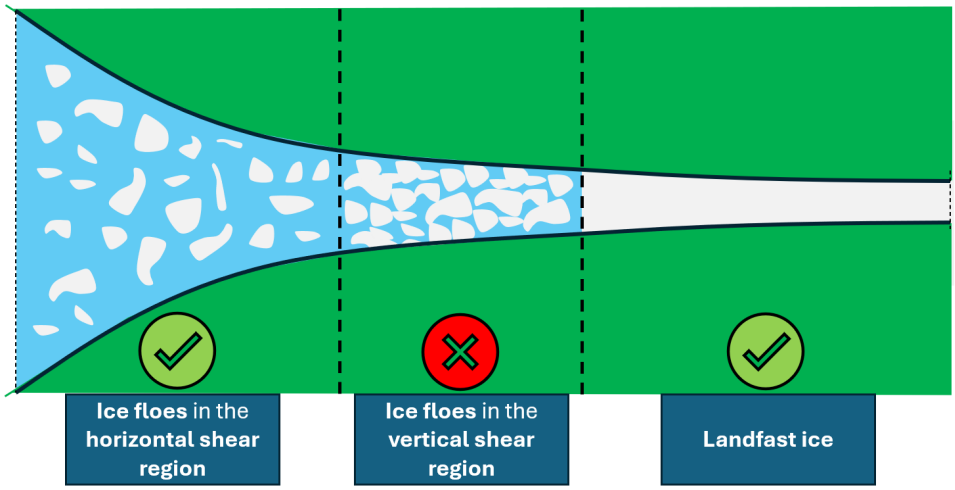


Figure 2.3: The three types of ice that we distinguish are shown schematically: ice floes with negligible vertical stresses (left), ice floes with strong vertical stresses (middle), and landfast ice (right). The ice floes in the horizontal shear region and landfast ice are analysed in the upcoming Chapters.

### 2.5.1 Modelling Landfast Ice

Since landfast ice is stationary, Burchard et al. (2023, p.61) models landfast ice as a no-slip condition at the surface, similar to the way bottom friction is often included in hydrodynamic models:

$$u = 0 \quad \text{for} \quad z = \zeta. \tag{2.17}$$

However, this condition requires us to solve not only the general Reynolds-averaged hydrodynamics in the core-region of the estuary, but also to solve the small-scale hydrodynamics in the boundary layers near the ice. For bottom friction, we have parametrised and idealised the influence of the boundary layer by applying a partial slip condition (see equation (2.14)). By applying the same reasoning, we will model the influence of landfast ice by

applying a partial slip condition at the surface, introducing the *ice friction parameter* $s_I$ (m/s):

$$\hat{\mathcal{A}}_{\mathrm{v}} u_z = -s_I u \quad \text{for} \quad z = \zeta. \tag{2.18}$$

### 2.5.2 Modelling Ice Floe in the Horizontal Shear Regions

The rheology of ice floes is, in general, assumed to be two-dimensional: the influence of vertical stresses within the ice is one order of magnitude less than that of horizontal stresses. There are many models that describe the ice's rheology, and all take into account different properties of ice (Leppäranta, 2005, p.116-131). One such model is introduced by Hibler III (1979, p.818), describing the ice as a nonlinear viscous compressible fluid. This model has been applied in a simplified way by Vasulkar (2024, p.74-78), who assumes that there is a relatively strong vertical shear force between the ice floes and the underlying water, which allows for the assumption that the velocity of the ice floes equals the water's velocity. The main effect of the ice layer on the water motion is then accounted for by including the internal horizontal stress as an additional frictional term in a depth-averaged hydrodynamic model. Furthermore, it is assumed that the internal friction of the ice floes can be approximated as linearly viscous.

To describe this linear viscous behaviour, Hibler III (1979) defines the ice floes' horizontal viscosity $\eta$ as follows:

$$\eta = \frac{P^* h_I e^{-C(1-A)}}{4 D_0 e_c^2}, \tag{2.19}$$

where $P^*$ is the compressive strength of compact ice of unit thickness, $h_I$ is the ice thickness, $C$ is a strength reduction constant for lead opening, $A$ is the ice compactness, $D_0$ is the maximum viscous creep parameter, and $e_c$ is the aspect ratio of the yield ellipse of the ice's rheology. The model of Hibler III (1979) and the simplifications done by Vasulkar (2024) function as the inspiration for our idealised way of modelling the ice floes' influence. Following these authors, we will assume that the ice floes' internal friction can be described as

$$\boldsymbol{\sigma} = \eta \begin{bmatrix} u_x^I & \frac{1}{2}\left(u_y^I + v_x^I\right) \\ \frac{1}{2}\left(u_y^I + v_x^I\right) & v_y^I \end{bmatrix}, \tag{2.20}$$

where $u^I$ and $v^I$ are the longitudinal and lateral ice velocities, respectively. This leads to the following force component in the longitudinal momentum-balance for the ice velocity field:

$$F_1 := \partial_x \sigma_{11} + \partial_y \sigma_{12} \tag{2.21}$$

$$= \left(\eta u_x^I\right)_x + \frac{1}{2}\left(\eta\left(u_y^I + v_x^I\right)\right)_y. \tag{2.22}$$

Applying the width-averaging procedure, it is found that:

$$\{F_1\} = \frac{1}{2\Delta}\left[B_2\left(\eta\left(u_y^I + v_x^I\right)\right)\Big|_{y=B_2} - B_1\left(\eta\left(u_y^I + v_x^I\right)\right)\Big|_{y=B_1}\right] \tag{2.23}$$

$$+ \frac{1}{\Delta}\left[\left(\{\eta\}\left[\left(\Delta\{u^I\}\right)_x + B_1' u^I\big|_{y=B_1} - B_2' u^I\big|_{y=B_2}\right]\right)_x + B_1'\left(\eta u_x^I\right)\Big|_{y=B_1} - B_2'\left(\eta u_x^I\right)\Big|_{y=B_2}\right], \tag{2.24}$$

where it is supposed that the width-variations of $\eta$ have a negligible influence on the large-scale wdth-averaged ice-dynamics. A full derivation of this expression can be found in Appendix A.2.4. Furthermore, assuming that - as a first modelling step - the influence of the boundary onto the width-averaged ice floe-behaviour is negligible, this expression simplifies to:

$$\{F_1\} = \frac{1}{\Delta}\left(\eta\left(\Delta\{u^I\}\right)_x\right)_x. \tag{2.25}$$

As sketched in Figure 2.4, we make use of the fact that ice floes only find themselves in a layer close to the water's surface. Within this layer, and within the horizontal shear region, we assume that the vertical coupling between the floes and the water is strong. Therefore, the width-averaged ice velocity is close to the width-averaged water velocity, allowing us to neglect the vertical shear force at the boundary, described by equation (2.18). Moreover, this strong coupling inspires us to model the influence of the internal ice floe stress (2.25) as an additional viscosity term in the layer in which ice floes find themselves. This leads to the following longitudinal momentum equation:

$$u_t + g\zeta_x - \hat{\mathcal{A}}_{\mathrm{v}} u_{zz} - \left(\hat{\mathcal{A}}_{\mathrm{h}} u_{xx} + \frac{F}{\Delta}\left(\eta\left(\Delta u\right)_x\right)_x\right) = 0, \tag{2.26}$$

where $F$ is a $z$-dependent parameter that accounts for the occurrence of enhanced horizontal viscosity due to the presence of ice floes in the upper layer. Outside this layer, the horizontal eddy viscosity will be equal to the eddy viscosity as discussed earlier. The exact size of the layer is unknown, and therefore, $F$ will be taken as a smooth function that vanishes as $z$ moves out of the ice-floe-layer.

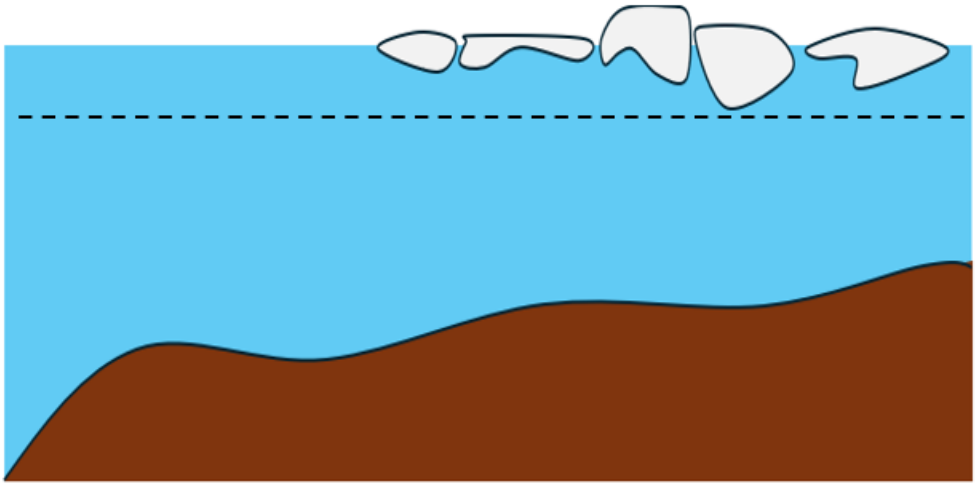

Figure 2.4: A schematic side-view of ice floes in the top layer of the water in the estuary.

## 2.6 Additional Boundary Conditions

In addition to the boundary condition (2.18) at the surface (either a partial slip condition for landfast ice ($s_I \neq 0$), or a no-slip condition for ice floes ($s_I = 0$)) and the partial slip condition (2.15) for bottom friction, we require more boundary conditions for the system to be solvable. In this section, we introduce the boundary conditions boundary:

**The Free Surface ($z = \zeta$)**

The free surface at $z = \zeta$ is defined as the top of the water layer;

1. The coordinates at the surface of the water, must remain at the surface. This leads to the *kinamatic boundary condition at the water's surface*,
$$w = u\zeta_x \quad \text{for} \quad z = \zeta(x,t). \tag{2.27}$$
Note that we assume here that there are no overturning waves, which is consistent with the length-scales of tidal waves (Cushman-Roisin and Beckers, 2011, p.103).

2. We assume that the pressure at the surface equals the atmospheric pressure:
$$p = p_{\text{atm}} \quad \text{for} \quad z = \zeta(x,t), \tag{2.28}$$
Where the pressure is assumed to be spatially uniform. Furthermore, we neglect the surface tension, which is only of importance for short water-waves with wavelengths of only a few centimetres (Cushman-Roisin and Beckers, 2011, p.104).

**The Bottom**

1. A commonly used assumption is that the flow is parallel to the bottom; in other words, the flow is perpendicular to the normal vector at the bottom. This translates into the following *impermeable bottom condition* (Cushman-Roisin and Beckers, 2011, p.103):
$$\mathbf{u} \cdot \begin{bmatrix} H_x \\ 0 \\ 1 \end{bmatrix} = 0 \quad \text{for} \quad z = -H(x). \tag{2.29}$$

**Seaward Side**

1. At the seaward side, we prescribe the influence of tides on the water height. The $M_2$-tide, with a period of twelve hours and twenty-five minutes is often dominant (De Swart, 2009, p.31), we will focus on the dynamics of this tidal constituent. We will also include the $M_4$-tide, which can be used to analyse the residual transport of particulate matter or sediments (Chernetsky, 2012). This transport, however, is not part of the scope of this thesis
$$\zeta = A_{M_2}\cos(\sigma t) + A_{M_4}\cos(2\sigma t) \quad \text{for} \quad x = 0, \tag{2.30}$$
where $\sigma \approx 1.406 \cdot 10^{-4}$ s$^{-1}$ is the frequency of the semi-diurnal ($M_2$) tide, and $A_{M_2}$ its amplitude; $A_{M_4}$ is the amplitude of the $M_4$-tide.

2. The behaviour of the longitudinal water velocity at the seaward side is highly dependent on the dynamics in the adjacent sea and the internal, estuarine dynamics, and therefore, it is difficult to determine a physically correct boundary condition. To circumvent this issue, we prescribe the following condition,

$$u_x = 0 \quad \text{for} \quad x = 0, \quad z \in [-H, \zeta]. \tag{2.31}$$

Since this boundary condition is not consistent with the internal dynamics, a non-physical boundary region near $x = 0$ will be formed. Hence, we will not base any conclusions on the behaviour of the estuary's hydrodynamics near $x = 0$.

**Riverine Side**

1. We assume that pointwise in $z$, the longitudinal water velocity vanishes at the riverine side, i.e.

$$u = 0 \quad \text{for} \quad x = L, \quad z \in [-H, \zeta]. \tag{2.32}$$

# Chapter 3

# Model Formulations

In this chapter, models are derived that separate the effects of landfast ice and ice floes in the horizontal shear region. In section 3.1, a perturbative method is applied to the model that was created in the previous chapter, allowing us to separate the effects of various tidal consitutents. The so-called leading order model that follows is linear, and only forced at the seaward side by the $M_2$-tidal consituent. In sections 3.2 and 3.3, this model is used to derive the equations describing the hydrodynamics in an estuary under the influence of either landfast ice or ice floes in the horizontal shear region.

## 3.1 Separating Tidal Constituents

If an estuary is not vertically stratified and if it its depth is large compared to the amplitude of the tide, it is expected that the influence of nonlinear terms in the longitudinal momentum balance is relatively small (Ianniello, 1977, p.756). Nonlinearly induced currents scale with the ratio of the tidal amplitude and the depth, i.e. $\varepsilon = A_{M_2}/H$. Using this ratio, a decomposition of the model equations into leading order equations and equations of smaller order can be created. Since the resulting ordered system of equations is linear at leading order, allows for a systematic way to study various tidal constitutents (Chernetsky, 2012, p.25-32). This *perturbative method* requires the definition of asymptotic expansions of our variables:

$$u = u^0 + \varepsilon\, u^1 + \varepsilon^2\, u^2 + ..., \tag{3.1}$$

$$w = w^0 + \varepsilon\, w^1 + \varepsilon^2\, w^2 + ..., \tag{3.2}$$

$$\zeta = \zeta^0 + \varepsilon\, \zeta^1 + \varepsilon^2\, \zeta^2 + .... \tag{3.3}$$

In order for this method to be valid, the following requirements must be satisfied (Chernetsky, 2012, p. 120-123).

1. The water's horizontal velocity is much smaller than the velocity required to travel through the full estuary within one $M_2$-oscillation, i.e. $\frac{U}{\sigma L} = \mathcal{O}(\varepsilon)$.
2. The density-driven residual circulation's velocity is much smaller than the water's horizontal velocity.
3. The amplitude of the other tidal constituent at the seaward side is much smaller than the amplitude of the $M_2$-tide at the seaward side, i.e. $\frac{A_{M_4}}{A_{M_2}} = \mathcal{O}(\varepsilon)$.
4. The river discharge at the riverine side is much smaller than the cross-sectional flow within the river, i.e. $\frac{Q}{UH_0B_0(L)} = \mathcal{O}(\varepsilon)$.

Assuming that the above requirements are met, one can derive the equations corresponding to the various orders by substituting the asymptotic expansions into the contiuity equation, longitudinal momentum balance and the boundary conditions. Focusing on the leading order model, we observe that it is only forced by the $M_2$-tide at the seaward side. Since the leading order equations are linear, all variables oscillate with the same $M_2$-frequency $\sigma$. This allows us to write

$$\begin{bmatrix} u^0(x,z,t) \\ w^0(x,z,t) \\ \zeta^0(x,t) \end{bmatrix} = \mathrm{Re}\left( \begin{bmatrix} \hat{u}^0(x,z) \\ \hat{w}^0(x,z) \\ \hat{\zeta}^0(x) \end{bmatrix} e^{i\sigma t} \right) \tag{3.4}$$

Resulting in the following linear partial differential equations for $\hat{u}^0$, $\hat{\zeta}^0$ and $\hat{w}^0$:

$$\begin{cases} \hat{u}^0_x + \hat{w}^0_z + \dfrac{\Delta_x}{\Delta}\hat{u}^0 & = 0, \quad (3.5a) \\ i\sigma\hat{u}^0 + g\hat{\zeta}^0_x - \hat{\mathcal{A}}_{\mathrm{v}}\hat{u}^0_{zz} - \left(\hat{\mathcal{A}}_{\mathrm{h}}\hat{u}^0_{xx} + \dfrac{F}{\Delta}\left(\eta\left(\Delta\hat{u}^0\right)_x\right)_x\right) & = 0, \quad (3.5b) \end{cases}$$

with the boundary conditions:

$$\begin{cases} \hat{\mathcal{A}}_{\mathrm{v}}\hat{u}^0_z = -s_I\hat{u}^0 & \text{for} \quad \mathrm{z} = 0, \quad (3.6a) \\ \hat{w}^0 = i\sigma\hat{\zeta}^0 & \text{for} \quad \mathrm{z} = 0, \quad (3.6b) \\ \hat{w}^0 + H_x\hat{u}^0 = 0 & \text{for} \quad \mathrm{z} = \text{-H(x)}, \quad (3.6c) \\ \hat{\mathcal{A}}_{\mathrm{v}}\hat{u}^0_z = s_F\hat{u}^0 & \text{for} \quad \mathrm{z} = \text{-H(x)}, \quad (3.6d) \\ \hat{\zeta}^0 = A_{M_2} & \text{for} \quad \mathrm{x}=0, \quad (3.6e) \\ \hat{u}^0_x = 0 & \text{for} \quad \mathrm{x} = 0, \quad (3.6f) \\ \hat{u}^0 = 0 & \text{for} \quad \mathrm{x} = \mathrm{L}. \quad (3.6g) \end{cases}$$

A detailed derivation of these equations without ice can be found in Chernetsky (2012, p. 120-127).

## 3.2 Landfast Ice

To focus on the effect of landfast ice, one removes the ice floes' horizontal viscosity by setting $F \equiv 0$. This leads to the following partial differential equations:

$$\begin{cases} \hat{u}^0_x + \hat{w}^0_z + \dfrac{\Delta_x}{\Delta}\hat{u}^0 & = 0, \quad (3.7a) \\ i\sigma\hat{u}^0 + g\hat{\zeta}^0_x - \hat{\mathcal{A}}_{\mathrm{v}}\hat{u}^0_{zz} - \hat{\mathcal{A}}_{\mathrm{h}}\hat{u}^0_{xx} & = 0. \quad (3.7b) \end{cases}$$

The longitudinal momentum balance can be simplifiedy neglecting the horizontal viscosity term. Indeed, the magnitude of the viscosity terms can be estimated as follows:

$$\left(\hat{\mathcal{A}}_{\mathrm{h}}u_x\right)_x \sim \frac{\hat{\mathcal{A}}_{\mathrm{h}}}{L_0^2} \quad \text{and} \quad \left(\hat{\mathcal{A}}_{\mathrm{v}}u_z\right)_z \sim \frac{\hat{\mathcal{A}}_{\mathrm{v}}}{H_0^2}. \quad (3.8)$$

Using that $\hat{\mathcal{A}}_{\mathrm{h}} \sim 0.1 - 10$ m$^2$/s, $\hat{\mathcal{A}}_{\mathrm{v}} \sim 10^{-4} - 10^{-2}$ m$^2$/s (De Swart, 2009, p.21) and $L_0/H_0 \sim 10^5/10 = 10^4$, it follows that

$$\left(\hat{\mathcal{A}}_{\mathrm{h}}u_x\right)_x \ll \left(\hat{\mathcal{A}}_{\mathrm{v}}u_z\right)_z. \quad (3.9)$$

Therefore, when ice floes are omitted from the model, the horizontal viscosity term is negligible. However, by neglcting the horizontal viscosity term, we cannot prescribe pointwise velocity boundary conditions at $x = 0$ and $x = L$ (i.e. $\hat{u}^0_x = 0$ for $x = 0$ and $\hat{u}^0 = 0$ for $x = L$). Instead of the pointwise boundary condition at $x = L$, a condition on the depth-integrated velocity at $x = L$ is prescribed:

$$\int_{-H}^{0} \hat{u}^0 dz = 0 \quad \text{for} \quad x = L \quad (3.10)$$

This leads to the following model, describing the effect of landfast ice on the estuary's leading order hydrodynamics.

**The Leading Order Model for Landfast Ice** is given by

$$\begin{cases} \hat{u}^0_x + \hat{w}^0_z + \dfrac{\Delta_x}{\Delta}\hat{u}^0 & = 0, \quad (3.11a) \\ i\sigma\hat{u}^0 + g\hat{\zeta}^0_x - \hat{\mathcal{A}}_{\mathrm{v}}\hat{u}^0_{zz} & = 0, \quad (3.11b) \end{cases}$$

with the following boundary conditions:

$$\begin{cases} \hat{\mathcal{A}}_{\mathrm{v}}\hat{u}^0_z = -s_I\hat{u}^0 & \text{for} \quad \mathrm{z} = 0, \quad (3.12a) \\ \hat{w}^0 = i\sigma\hat{\zeta}^0 & \text{for} \quad \mathrm{z} = 0, \quad (3.12b) \\ \hat{w}^0 + H_x\hat{u}^0 = 0 & \text{for} \quad \mathrm{z} = \text{-H(x)}, \quad (3.12c) \\ \hat{\mathcal{A}}_{\mathrm{v}}\hat{u}^0_z = s_F\hat{u}^0 & \text{for} \quad \mathrm{z} = \text{-H(x)}, \quad (3.12d) \\ \hat{\zeta}^0 = A_{M_2} & \text{for} \quad \mathrm{x}=0, \quad (3.12e) \\ \displaystyle\int_{-H}^{0} \hat{u}^0 dz = 0 & \text{for} \quad \mathrm{x}=\mathrm{L}. \quad (3.12f) \end{cases}$$

To remove the effects of ice altogether, one additionally takes the limit $s_I \downarrow 0$ in equation (3.12a).

## 3.3 Ice Floes in the Horizontal Shear Region

By omitting the vertical shear friction caused by landfast ice, the leading order model can be simplified to describe only the effect of ice floes in the horizontal shear region. The depth-profile of the longitudinal water velocity is approximated by $z$-dependent eigenfunctions. The free surface level and the amplitudes of the eigenfunctions are approximated by means of a finite difference method in the $x$-direction.

### 3.3.1 The Leading Order Equations for Only Ice Floes in the Horizontal Shear Region

In the region with ice floes where the vertical shear is negligible with respect to the horizontal shear, the leading order model is simplified by taking $s_I \downarrow 0$ in the partial slip boundary condition in (3.6a). This leads to the following model.

**The Leading Order Model for Ice Floes in the Horizontal Shear Zone** is given by

$$\begin{cases} u^0_x + w^0_z + \dfrac{\Delta_x}{\Delta}u^0 & = 0, \quad (3.13a) \\ u^0_t + g\zeta^0_x - \hat{\mathcal{A}}_{\mathrm{v}}u^0_{zz} - \hat{\mathcal{A}}_{\mathrm{h}}\hat{u}^0_{xx} - F\left(\eta u^0_x\right)_x & = 0, \quad (3.13b) \end{cases}$$

with the boundary conditions,

$$\begin{cases} \hat{\mathcal{A}}_{\mathrm{v}}\hat{u}^0_z = 0 & \text{for} \quad \mathrm{z} = 0, \quad (3.14a) \\ \hat{w}^0 = i\sigma\hat{\zeta}^0 & \text{for} \quad \mathrm{z} = 0, \quad (3.14b) \\ \hat{w}^0 + H_x\hat{u}^0 = 0 & \text{for} \quad \mathrm{z} = \text{-H(x)}, \quad (3.14c) \\ \hat{\mathcal{A}}_{\mathrm{v}}\hat{u}^0_z = s_F\hat{u}^0 & \text{for} \quad \mathrm{z} = \text{-H(x)}, \quad (3.14d) \\ \hat{\zeta}^0 = A_{M_2} & \text{for} \quad \mathrm{x}=0, \quad (3.14e) \\ \hat{u}^0_x = 0 & \text{for} \quad \mathrm{x} = 0, \quad (3.14f) \\ \Delta\displaystyle\int_{-H}^{0} \hat{u}^0 dz = 0 & \text{for} \quad \mathrm{x}=\mathrm{L}, \quad (3.14g) \\ \hat{u}^0 = 0 & \text{for} \quad \mathrm{x} = \mathrm{L}. \quad (3.14h) \end{cases}$$

# Chapter 4

# The Solution Methods

This chapter describes the methods that are used to derive solutions to the models that were given in the previous chapter. For the models with landfast ice and without ice, analytical solutions are derived in section 4.1. For the model describing the influence of ice floes in the horizontal shear zone, the solutions can no longer be determined analytically. A numerical method to approximate solutions to this model is described in section 4.2.

In this thesis, we will focus on computing the longitudinal water velocity and the waterlevel, and we will not determine the vertical water velocity. Indeed, writing $W_0$ and $U_0$ for the magnitudes of the width-averaged vertical and longitudinal water velocities, repectively, the width-averaged continuity equation implies that

$$\frac{U_0}{L_0} \sim \frac{W_0}{H_0}. \tag{4.1}$$

Since it is assumed that the horizontal length-scale $L_0$ is much smaller than the vertical length-scale $H_0$ (i.e. $H_0 \ll L_0$), it follows that $W_0 \ll U_0$. In other words, the longitudinal velocities are assumed to be much larger than the vertical velocities, and thus the latter are of much less significance.

## 4.1 Landfast Ice and No Ice

The analytical solutions to the models for landfast ice and no ice can be computed in a similar way, and therefore, the description of these methods is combined in this section. The longitudinal momentum balance (3.11b) is an ordinary differential equation for $\hat{u}^0$ with $\hat{\zeta}_x^0$ an inhomogeneous term. Solving this differential equation leads to the following general solution for the leading order longtudinal water velocity:

$$\hat{u}^0 = \frac{g\hat{\zeta}_x^0}{i\sigma}\left(-1 + \alpha_1 \cosh(\beta z) + \alpha_2 \sinh(\beta z)\right), \tag{4.2}$$

where

$$\beta = \sqrt{\frac{\sigma}{2\hat{\mathcal{A}}_{\mathrm{v}}}}\,(1+i). \tag{4.3}$$

The expressions for the coefficients $\alpha_1$ and $\alpha_2$ can be determined by applying the partial slip conditions at the bottom and at the surface. These coefficients read:

$$\alpha_1 = \frac{-s_F\hat{\mathcal{A}}_{\mathrm{v}}\beta - s_I\left(\hat{\mathcal{A}}_{\mathrm{v}}\beta\cosh(-\beta H) - s_F\sinh(-\beta H)\right)}{\hat{\mathcal{A}}_{\mathrm{v}}\beta\left(\hat{\mathcal{A}}_{\mathrm{v}}\beta\sinh(-\beta H) - s_F\cosh(-\beta H)\right) - s_I\left(\hat{\mathcal{A}}_{\mathrm{v}}\beta\cosh(-\beta H) - s_F\sinh(-\beta H)\right)}, \tag{4.4}$$

$$\alpha_2 = \frac{s_I\left(\hat{\mathcal{A}}_{\mathrm{v}}\beta\sinh(-\beta H) - s_F\cosh(-\beta H)\right) + s_I s_F}{\hat{\mathcal{A}}_{\mathrm{v}}\beta\left(\hat{\mathcal{A}}_{\mathrm{v}}\beta\sinh(-\beta H) - s_F\cosh(-\beta H)\right) - s_I\left(\hat{\mathcal{A}}_{\mathrm{v}}\beta\cosh(-\beta H) - s_F\sinh(-\beta H)\right)}. \tag{4.5}$$

To derive an ordinary differential equation that is satisfied by the leading order waterlevel, the continuity equation in (3.11a) is integrated over the depth (i.e. from $z = -H$ until $z = 0$). Applying Leibniz' integral rule, the kinematic boundary condition for the surface and the impermeable bottom conditon, the following expression is found:

$$\hat{U}_x^0 + i\sigma\hat{\zeta}^0 + \frac{\Delta_x}{\Delta}\hat{U}^0 = 0, \tag{4.6}$$

where

$$\hat{U}^0 := \int_{-H}^{0} \hat{u}^0 \, dz \tag{4.7}$$

$$= -\frac{g\hat{\zeta}_x^0}{i\sigma}\left(H + \frac{1}{\beta}\left[\alpha_1 \sinh(-\beta H) + \alpha_2\left(1 - \cosh(-\beta H)\right)\right]\right). \tag{4.8}$$

For notational convience, we define the *frictional wave velocity* as

$$c_{FI}^2 := gH + \frac{g}{\beta}\left[\alpha_1 \sinh(-\beta H) + \alpha_2\left(\cosh(-\beta H) - 1\right)\right]. \tag{4.9}$$

With this definition, one can write

$$\hat{U}^0 = -\frac{c_{FI}^2 \hat{\zeta}_x^0}{i\sigma}, \tag{4.10}$$

and

$$\hat{U}_x^0 = -\frac{1}{i\sigma}\left(\hat{\zeta}_{xx}^0 \, c_{FI}^2 + \hat{\zeta}_x^0 \left(c_{FI}^2\right)_x\right). \tag{4.11}$$

Substituting these expressions into (4.6) leads to the following ODE for $\hat{\zeta}^0$:

$$c_{FI}^2 \hat{\zeta}_{xx}^0 + \left(\left(c_{FI}^2\right)_x + \frac{\Delta_x}{\Delta} c_{FI}^2\right)\hat{\zeta}_x^0 + \sigma^2 \hat{\zeta}^0 = 0. \tag{4.12}$$

This equation requires two boundary conditions for $\hat{\zeta}^0$, the first of which is given by the $M_2$-forcing at the seawrd side:

$$\hat{\zeta}^0 = A_{M_2} \quad \text{for} \quad x = 0. \tag{4.13}$$

The second boundary condition is found by substituting (4.10) into the boundary condition (3.10):

$$\hat{U}^0 = -\frac{c_{FI}^2 \hat{\zeta}_x^0}{i\sigma} = 0 \quad \text{for} \quad x = L. \tag{4.14}$$

Since $c_{FI}^2/(i\sigma) \neq 0$, this condition reduces to:

$$\hat{\zeta}_x^0 = 0 \quad \text{for} \quad x = L. \tag{4.15}$$

The differential equation (4.12) is too complex to solve with analytical methods. To simplify it into an equation that can be solved analytically, it is assumed that the depth $H$ and the friction parameters $s_I$ and $s_F$ are constant, and that the estuary-width is exponentially converging with convergence length $L_b$:

$$\Delta(x) = B_0 e^{-\frac{x}{L_b}}. \tag{4.16}$$

These assumptions lead to the following system for $\hat{\zeta}^0$:

$$\begin{cases} \hat{\zeta}_{xx}^0 - \dfrac{1}{L_b}\hat{\zeta}_x^0 + \dfrac{\sigma^2}{c_{FI}^2}\hat{\zeta}^0 = 0, & & \text{(4.17a)} \\ \hat{\zeta}^0 = A_{M_2} & \text{for} \quad \text{x=0}, & \text{(4.17b)} \\ \hat{\zeta}_x^0 = 0 & \text{for} \quad \text{x=L}. & \text{(4.17c)} \end{cases}$$

We will solve this system for three cases: one where the estuary is fully covered by landfast ice, one where there is no ice, and one in which the estuary is partially covered in landfast ice.

In case of a full landfast ice cover, the general solution to equation (4.17a) is given by

$$\hat{\zeta}^0 = \tilde{a}_1 e^{\lambda_2^{FI}(x-L)} + \tilde{a}_2 e^{\lambda_1^{FI}(x-L)}, \tag{4.18}$$

where

$$\lambda_{1,2}^{FI} = \frac{1}{2L_b} \pm i\sqrt{\frac{\sigma^2}{c_{FI}^2} - \left(\frac{1}{2L_b}\right)^2}. \tag{4.19}$$

Applying the boundary conditions leads to the following expression for the leading order waterlevel:

$$\hat{\zeta}^0 = A_{M_2} \frac{\lambda_1^{FI} e^{\lambda_2^{FI}(x-L)} - \lambda_2^{FI} e^{\lambda_1^{FI}(x-L)}}{\lambda_1^{FI} e^{-\lambda_2^{FI} L} - \lambda_2^{FI} e^{-\lambda_1^{FI} L}}. \tag{4.20}$$

The solution for a constant estuary-width is found by taking the limit $L_b \to \infty$, leading to the following expression:

$$\hat{\zeta}^0 = \frac{A_{M_2} \cos\left(\frac{\sigma(x-L)}{c_{FI}}\right)}{\cos\left(\frac{\sigma L}{c_{FI}}\right)}. \tag{4.21}$$

The solutions without ice can be found by setting taking the limit $s_I \downarrow 0$. This leads to similar expressions for the leading order waterlevel as given by (5.13), (4.20) and (4.21), with the only difference being that $c_{FI}$ is replaced by

$$c_F^2 = \lim_{s_I \downarrow 0} c_{FI}^2 = gH + \frac{g\alpha \sinh(-\beta H)}{\beta}, \tag{4.22}$$

where

$$\alpha = \frac{s_F}{s_F \cosh(-\beta H) - \hat{\mathcal{A}}_{\mathrm{v}} \beta \sinh(-\beta H)}. \tag{4.23}$$

These solutions without ice agree with the solutions given by Chernetsky (2012).

In case of a partial ice cover, a new parameter $x_I$ is introduced, splitting the longitudinal axis in two parts: part I corresponding to $0 < x < x_I$, where there is no ice, and part II corresponding to $x_I < x < L$, where there is a landfast ice cover; see Figure 4.1. This leads to the following landfast ice boundary condition at the water's surface:

$$\hat{\mathcal{A}}_{\mathrm{v}} \hat{u}_z^0 = \begin{cases} 0, & \text{if } 0 < x < x_I, \quad (4.24a) \\ -s_I \hat{u}^0, & \text{if } x_I < x < L, \quad (4.24b) \end{cases}$$

for $z = 0$. In each part, the ODE (4.17a) for the waterlevel is solved. However, two additional boundary conditions

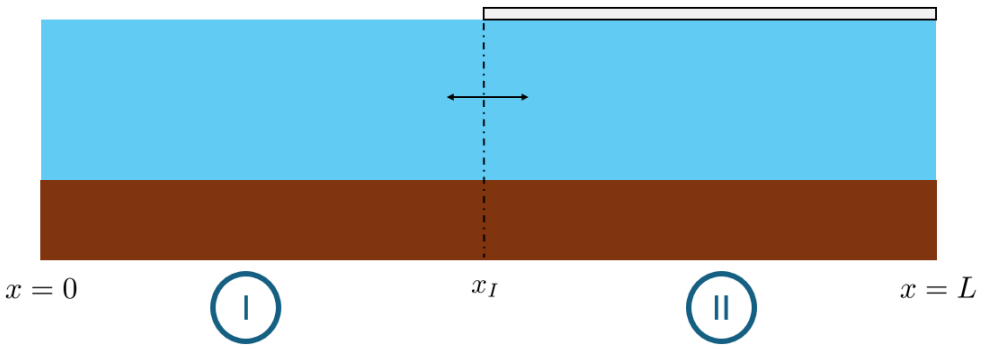


Figure 4.1: A schematic side-view of the partial ice cover model. For $0 < x < x_I$ (part I), there is no ice, and for $x_I < x < L$ (part II), the estuary is covered in landfast ice.

are required, linking the no-ice solution (in part I) to the ice-solution (in part II) at $x = x_I$. This is done by demanding continuity of both the waterlevel and the total discharge at $x = x_I$:

$$\begin{cases} \lim\limits_{x \uparrow x_I} \hat{\zeta}^0 = \lim\limits_{x \downarrow x_I} \hat{\zeta}^0, & (4.25a) \\ \lim\limits_{x \uparrow x_I} \int_{z=-H}^{0} \hat{u}^0(x,z)\, dz = \lim\limits_{x \downarrow x_I} \int_{z=-H}^{0} \hat{u}^0(x,z)\, dz. & (4.25b) \end{cases}$$

By applying (4.10), the second condition reduces to

$$c_F \lim_{x \uparrow x_I} \hat{\zeta}_x^0 = c_{FI} \lim_{x \downarrow x_I} \hat{\zeta}_x^0, \tag{4.26}$$

so that the system for this situation is given by

$$\begin{cases} \hat{\zeta}^0_{xx} - \dfrac{1}{L_b}\,\hat{\zeta}^0_x + \dfrac{\sigma^2}{c_{FI}^2}\hat{\zeta}^0 = 0, & (4.27a)\\ \hat{\zeta}^0 = A_{M_2} \quad \text{for} \quad x = 0, & (4.27b)\\ \hat{\zeta}^0_x = 0 \quad \text{for} \quad x = L, & (4.27c)\\ \lim\limits_{x\uparrow x_I} \hat{\zeta}^0 = \lim\limits_{x\downarrow x_I} \hat{\zeta}^0, & (4.27d)\\ c_F \lim\limits_{x\uparrow x_I} \hat{\zeta}^0_x = c_{FI} \lim\limits_{x\downarrow x_I} \hat{\zeta}^0_x. & (4.27e) \end{cases}$$

A solution to this system is given by

$$\hat{\zeta}^0(x) = \begin{cases} \tilde{a}_1^F e^{\lambda_1^F (x-x_I)} + e^{\lambda_2^F x_I}\left(A_{M_2} - \tilde{a}_1^F e^{-\lambda_1^F x_I}\right) e^{\lambda_2^F (x-x_I)}, & \text{if } 0 < x < x_I, \quad (4.28a)\\ \tilde{a}_1^{FI} e^{\lambda_1^{FI}(x-x_I)} - \tilde{a}_1^{FI}\dfrac{\lambda_1^{FI}}{\lambda_2^{FI}} e^{\left(\lambda_1^{FI}-\lambda_2^{FI}\right)(L-x_I)} e^{\lambda_2^{FI}(x-x_I)}, & \text{if } x_I < x < L, \quad (4.28b) \end{cases}$$

where $\lambda^F_{1,2} = \lim_{s_I\downarrow 0} \lambda^{FI}_{1,2}$ and the coefficients are given by

$$\tilde{a}_1^F = \frac{\left(-e^{\lambda_2^F x_I} A_{M_2}\right)\left(-c_{FI}^2\lambda_1^{FI} + c_{FI}^2\lambda_1^{FI} e^{\left(\lambda_1^{FI}-\lambda_2^{FI}\right)(L-x_I)}\right) - \left(-1 + \frac{\lambda_1^{FI}}{\lambda_2^{FI}} e^{\left(\lambda_1^{FI}-\lambda_2^{FI}\right)(L-x_I)}\right)\left(-c_F^2\lambda_2^F e^{\lambda_2^F x_I} A_{M_2}\right)}{\left(1 - e^{\left(\lambda_2^F-\lambda_1^F\right)x_I}\right)\left(-c_{FI}^2\lambda_1^{FI} + c_{FI}^2\lambda_1^{FI} e^{\left(\lambda_1^{FI}-\lambda_2^{FI}\right)(L-x_I)}\right) - \left(-1 + \frac{\lambda_1^{FI}}{\lambda_2^{FI}} e^{\left(\lambda_1^{FI}-\lambda_2^{FI}\right)(L-x_I)}\right)\left(c_F^2\lambda_1^F - c_F^2\lambda_2^F e^{\left(\lambda_2^F-\lambda_1^F\right)x_I}\right)}, \quad (4.29)$$

$$\tilde{a}_1^{FI} = \frac{\left(1 - e^{\left(\lambda_2^F-\lambda_1^F\right)x_I}\right)\left(-c_F^2\lambda_2^F e^{\lambda_2^F x_I} A_{M_2}\right) - \left(-e^{\lambda_2^F x_I} A_{M_2}\right)\left(c_F^2\lambda_1^F - c_F^2\lambda_2^F e^{\left(\lambda_2^F-\lambda_1^F\right)x_I}\right)}{\left(1 - e^{\left(\lambda_2^F-\lambda_1^F\right)x_I}\right)\left(-c_{FI}^2\lambda_1^{FI} + c_{FI}^2\lambda_1^{FI} e^{\left(\lambda_1^{FI}-\lambda_2^{FI}\right)(L-x_I)}\right) - \left(-1 + \frac{\lambda_1^{FI}}{\lambda_2^{FI}} e^{\left(\lambda_1^{FI}-\lambda_2^{FI}\right)(L-x_I)}\right)\left(c_F^2\lambda_1^F - c_F^2\lambda_2^F e^{\left(\lambda_2^F-\lambda_1^F\right)x_I}\right)}. \quad (4.30)$$

For a constant estuary-width, this expression can be simplified by taking the limit $L_b \to \infty$, leading to:

$$\hat{\zeta}^0 = \begin{cases} a_1^F \cos\left(\dfrac{\sigma(x-x_I)}{c_F}\right) + a_2^F \sin\left(\dfrac{\sigma(x-x_I)}{c_F}\right), & \text{if } 0 < x < x_I, \quad (4.31a)\\ a_1^F \cos\left(\dfrac{\sigma(x-x_I)}{c_{FI}}\right) + \dfrac{c_F}{c_{FI}}\, a_2^F \sin\left(\dfrac{\sigma(x-x_I)}{c_{FI}}\right), & \text{if } x_I < x < L, \quad (4.31b) \end{cases}$$

where the coefficients are given by

$$a_1^F = \frac{c_{FI} A_{M_2} \cos\left(\frac{\sigma(L-x_I)}{c_{FI}}\right)}{c_F \cos\left(-\frac{\sigma x_I}{c_F}\right)\cos\left(\frac{\sigma(L-x_I)}{c_{FI}}\right) + c_{FI}\sin\left(-\frac{\sigma x_I}{c_F}\right)\sin\left(\frac{\sigma(L-x_I)}{c_{FI}}\right)}, \quad (4.32)$$

$$a_2^F = \frac{c_F A_{M_2} \sin\left(\frac{\sigma(L-x_I)}{c_{FI}}\right)}{c_F \cos\left(-\frac{\sigma x_I}{c_F}\right)\cos\left(\frac{\sigma(L-x_I)}{c_{FI}}\right) + c_{FI}\sin\left(-\frac{\sigma x_I}{c_F}\right)\sin\left(\frac{\sigma(L-x_I)}{c_{FI}}\right)}. \quad (4.33)$$

The solutions for full ice covers have been checked by comparing to the numerical solution, described in Appendix B. The solution for constant width and a partial ice cover is checked by relating it to the solution for full ice covers; see Appendix C.

## 4.2 Ice Floes in the Horizontal Shear Region

Due to the importance of the horizontal viscosity in the model describing the effect of ice floes in the horizontal shear region, one cannot first solve for the vertical profile of $\hat{u}^0$ and then for $\hat{\zeta}^0$. Instead, both the longitudinal water velocity and the waterlevel must be solved simultaneously. This implies that both the horizontal and the vertical direction have to be discretised, and this discretised system will be solved to get approximations for $\hat{u}^0$ and $\hat{\zeta}^0$.

As a first step, it is assumed that the estuary-depth $H$ is constant. In this case, the $z$-coordinate does not have to be rescaled.

The vertical dependency of $u$ is discretised using a spectral method:

$$\hat{u}^0(x,z) = \sum_{n=1}^{\infty} a_n(x)\phi_n(z), \quad (4.34)$$

where $(\phi_n)_{n=1}^{\infty}$ are the eigenfunctions. Using information from the longitudinal momentum balance, the free slip and the partial bottom slip boundary conditions, it is natural to require that these eigenfunctions satisfy the following boundary value problem:

$$\begin{cases} \phi_n''(z) + \lambda_n \phi_n(z) = 0, & \text{(4.35a)} \\ \phi_n'(0) = 0, & \text{(4.35b)} \\ \hat{\mathcal{A}}_{\mathrm{v}} \phi_n'(-H) = s_F \phi_n(-H). & \text{(4.35c)} \end{cases}$$

This leads to the following expression for the eigenfunctions,

$$\phi_n(z) := \cos\left(z\sqrt{\lambda_n}\right), \tag{4.36}$$

where the eigenvalues $(\lambda_n)_{n=1}^{\infty}$ satisfy the following condition:

$$\tan\left(-H\sqrt{\lambda_n}\right) = -\frac{s_F}{\hat{\mathcal{A}}_{\mathrm{v}}\sqrt{\lambda_n}}. \tag{4.37}$$

No closed expressions for these $\lambda_n$ exist. Therefore, the eigenvalues are approximated numerically using a bisection method. The approximations for the first eleven eigenvalues are shown with green dots in Figure 4.2a, and - based on these approximations - the first 11 eigenfunctions are shown in Figure 4.2b. To be able to apply the spectral method

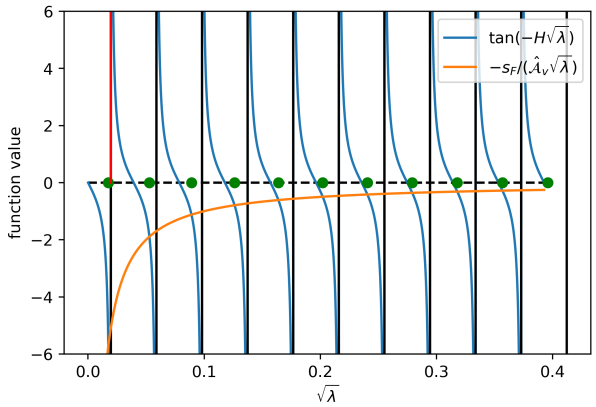


(a) The approximations of the square-roots of the first eleven eigenvalues.

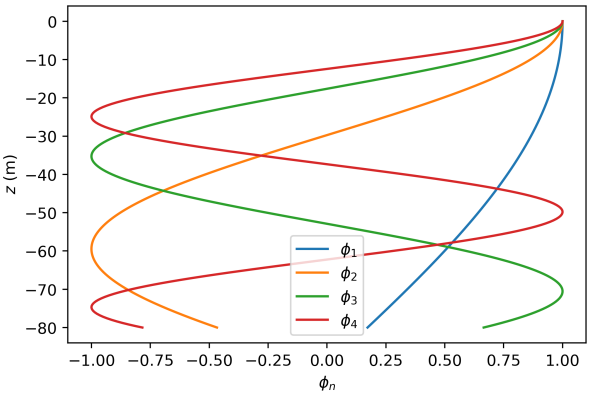


(b) The first four eigenfunctions $(\phi_n)_{n=1}^{4}$.

Figure 4.2: The approximations of the eigenvalues are done by a bisection method applied to the function $\tan\left(-H\sqrt{\lambda}\right) + \frac{s_F}{\hat{\mathcal{A}}_{\mathrm{v}}\sqrt{\lambda}}$, where the stopping criterion is that the absolute value of this function is smaller than $10^{-14}$.

in a numerical setting, we will cut off the infinite sum representation of $\hat{u}^0$ after $n = N_a$, leading to the following approximation:

$$\hat{u}^0(x,z) \approx \sum_{n=1}^{N_a} a_n(x)\phi_n(z). \tag{4.38}$$

To determine the $x$-dependent coefficients $(a_n)_{n=1}^{N_a}$, we substitute the spectral approximation (4.38) in the longitudinal momentum balance, and using that $\phi_n''(z) = -\lambda_n \phi_n(z)$, we find that

$$\sum_{n=1}^{N_a} \left[ \left( i\sigma + \hat{\mathcal{A}}_{\mathrm{v}}\lambda_n \right) a_n(x)\phi_n(z) + \hat{\mathcal{A}}_{\mathrm{h}} a_n''(x)\phi_n(z) \right] + g\hat{\zeta}_x^0 \tag{4.39}$$

$$- \frac{F(z)}{\Delta} \sum_{n=1}^{N_a} \left[ (\eta_x \Delta_x + \eta \Delta_{xx})\, a_n(x) + (\eta_x \Delta + 2\eta \Delta_x)\, a_n'(x) + \eta \Delta a_n''(x) \right] \phi_n(z) = 0. \tag{4.40}$$

Multiplying by $\phi_m$ for some $m \in \{1, ..., N_a\}$, integrating over $z$ from $-H$ until 0 and using orthogonality of eigenfunctions leads to the following equations:

$$\left( i\sigma + \hat{\mathcal{A}}_{\mathrm{v}}\lambda_m \right) a_m(x)\langle \phi_m, \phi_m \rangle + \hat{\mathcal{A}}_{\mathrm{h}} a_m''(x)\langle \phi_m, \phi_m \rangle + g\langle 1, \phi_m \rangle \hat{\zeta}_x^0 \tag{4.41}$$

$$- \sum_{n=1}^{N_a} \left[ (\eta_x \Delta_x + \eta \Delta_{xx})\, a_n(x) + (\eta_x \Delta + 2\eta \Delta_x)\, a_n'(x) + \eta \Delta a_n''(x) \right] \frac{\langle F\phi_n, \phi_m \rangle}{\Delta} = 0, \tag{4.42}$$

where the inner product is defined as

$$\langle a(z), b(z) \rangle := \int_{-H}^{0} a(z) b(z)\, dz, \tag{4.43}$$

and ' means differentiating with respect to $x$. These equations come with the following boundary conditions for $m = 1, ..., N_a$:

$$a'_m(0) = 0, \tag{4.44}$$

$$a_m(L) = 0. \tag{4.45}$$

Integrating the continuity equation (3.13a) from $z = -H$ to $z = 0$ leads to the following equation:

$$\hat{U}^0_x + \frac{\Delta_x}{\Delta} \hat{U}^0 + i\sigma \hat{\zeta}^0 = 0, \tag{4.46}$$

where $\hat{U}^0$ is defined as in (4.7). Substituting the spectral approximation (4.38) in equation (4.46) leads to the following equation:

$$\sum_{n=1}^{N_a} \left[ \left( a'_n(x) + \frac{\Delta_x}{\Delta} a_n(x) \right) \langle 1, \phi_n(z) \rangle \right] + i\sigma \hat{\zeta}^0 = 0. \tag{4.47}$$

For $\hat{\zeta}^0$, the following boundary conditions are also imposed:

$$\hat{\zeta}^0(0) = A_{M_2}, \tag{4.48}$$

$$\hat{\zeta}^0_x(L) = 0. \tag{4.49}$$

The unknowns $\left( a_1(x), ..., a_{Na}(x), \hat{\zeta}^0(x) \right)$ in equations (4.41) and (4.47), together with the appropriate boundary conditions abtained using a finite-difference approach. To that end, we define the grid $x_j = jh$ for $j = 0, ..., N_x$, with $h = L/N_x$. The derivatives are approximated as follows:

1. The gradient of the waterlevel is approximated by a central difference, i.e. for $j = 1, ..., N_x - 1$,

$$\hat{\zeta}^0_x(x_j) = \frac{\hat{\zeta}^{0,j+1} - \hat{\zeta}^{0,j-1}}{2h} + \mathcal{O}(h^2), \tag{4.50}$$

   where $\hat{\zeta}^{0,j} := \hat{\zeta}^0(x_j)$.

2. The first-order derivatives of the coefficients $(a_n)_{n=1}^{N_a}$ are approximated by a right-sided first-order finite difference, to make sure numerical oscillations do not occur. This reads:

$$a'_n(x_j) = \frac{a_n^{j+1} - a_n^j}{h} + \mathcal{O}(h), \tag{4.51}$$

   for $n = 1, ..., N_a$ and $j = 1, ..., N_x - 1$, where $a_n^j := a_n(x_j)$.

3. The diffusive terms are approximated by central difference scheme:

$$a''_n(x_j) = \frac{a_n^{j+1} - 2a_n^j + a_n^{j-1}}{h^2} + \mathcal{O}(h^2), \tag{4.52}$$

   for $n = 1, ..., N_a$.

4. The Neumann boundary conditions are approximated by first-order one-sided derivatives, so that we do not require ghost-nodes:

$$\hat{\zeta}^0_x(L) = \frac{\hat{\zeta}^{0,N_x} - \hat{\zeta}^{0,N_x-1}}{h} + \mathcal{O}(h), \tag{4.53}$$

   and

$$a'_n(0) = \frac{a_n^1 - a_n^0}{h} + \mathcal{O}(h), \tag{4.54}$$

   for $n = 1, ..., N_a$.

The complete linear system that follows from these discretisations is given in Appendix D. The implementation is checked in Appendix E by analysing the error made in approximating the approximations for $F \equiv 0$ with the analytical solution without ice from section 3.2.

# Chapter 5

# Physical Interpretation Framework for the Model Without Ice

In this chapter, a physical interpretation framework for the hydrodynamics described by the equations from section 3.1 is built, where the effects of ice are left out. Section 5.1 introduces the parameter values that are used to model Cook Inlet. In section 5.2, the development of solutions over time is considered. Section 5.3 discusses the effect of bottom friction and vertical eddy vescosity on the profile of the longitudinal water velocity. Then, section 5.4 discusses the effect of bottom friction and an exponentially converging estuary-width on the resonance properties of the tide.

## 5.1 Parameter Values for Cook Inlet

The parameter values that apply to Cook inlet are given in Table 5.1. Unless specified otherwise, these values are used to create the results in the coming chapters.

| **Quantity** | **Symbol** | **Value** | **Source** |
|---|---|---|---|
| Estuary-length | $L$ | $350 \cdot 10^3$ m | The length of Cook Inlet is given by Mulherin et al. (2001, p.2) |
| Convergence-length | $L_b$ | $\frac{L}{3}$ | Approximating the convergence of the cross-sectional area by exponential convergence of the width |
| Eddy-viscosity | $\hat{\mathcal{A}}_\mathrm{v}$ | 0.0155 $\mathrm{m}^2/\mathrm{s}$ | The average of the values in the Ems-estuary found by Chernetsky et al. (2010, p.1228) |
| Bottom friction | $s_F$ | 0.0735 m/s | The average of the values in the Ems-estuary found by Chernetsky et al. (2010, p.1228) |
| Amplitude of the semi-diurnal tide at the entrance | $A_{M_2}$ | 1.8 m | The wave height at the entrance of the inlet according to Mulherin et al. (2001, p.58) |
| Gravitational acceleration | $g$ | 10 $\mathrm{m}/\mathrm{s}^2$ | A rounded value |
| Estuary-depth | $H$ | 85 m | This depth leads to solutions with a mean tidal amplitude of around 4.5 m at the riverine side of Cook Inlet (Mulherin et al., 2001, p.57) |

Table 5.1: The values of the parameters used for modelling the leading order water motion in Cook Inlet.

## 5.2 Time Dependency of the Solutions

As discussed in section 3.1, the solutions to the leading order model can be written as follows.

$$\begin{bmatrix} u^0(x,z,t) \\ \zeta^0(x,t) \end{bmatrix} = \mathrm{Re}\left( \begin{bmatrix} \hat{u}^0(x,z) \\ \hat{\zeta}^0(x) \end{bmatrix} e^{i\sigma t} \right) \tag{5.1}$$

One can rewrite this by singling out the local amplitudes and phases:

$$\begin{bmatrix} u^0(x,z,t) \\ \zeta^0(x,t) \end{bmatrix} = \mathrm{Re}\left( \begin{bmatrix} \left|\hat{u}^0(x,z)\right| e^{i\varphi^u(x,z)} \\ \left|\hat{\zeta}^0(x)\right| e^{i\varphi^\zeta(x)} \end{bmatrix} e^{i\sigma t} \right), \tag{5.2}$$

where $\left|\hat{u}^0(x,z)\right|$ and $\left|\hat{\zeta}^0(x)\right|$ are the local amplitudes of the leading order longitudinal water velocity and waterlevel, and $\varphi^u(x,z)$ and $\varphi^\zeta(x)$ their local phases, respectively. For most of the thesis, the focus will be on the local amplitudes. However, in analysing amplification properties of the tidal waves, it proves useful to consider the time-development of the waterlevel through the system, as will be discussed in section 5.4.

From equation (5.1), it is clear that all solutions are $2\pi/\sigma$-periodic. Figure 5.2 show the time-development of the leading order longitudinal water velocity and waterlevel within one period.

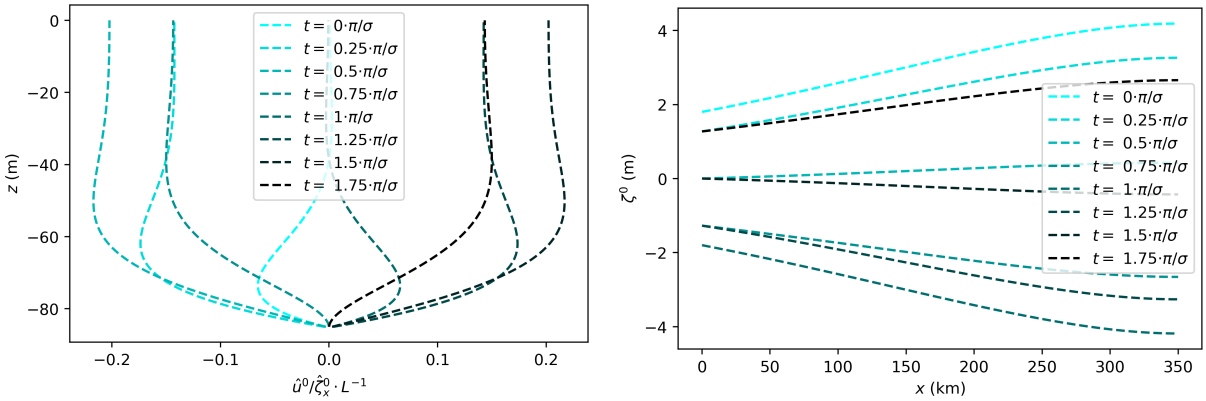


(a) The longitudinal water velocity.

(b) The free surface level.

Figure 5.1: The time-development of the leading order longitudinal water velocity and waterlevel. A darker colour corresponds to a later time-stamp.

## 5.3 The Effect of Bottom Friction and Vertical Eddy Viscosity on the Longitudinal Water Velocity's Profile

The effect of the bottom friction coefficient $s_F$ on the longitudinal water velocity's profile is shown in Figure 5.2a. It is clear that an increased friction cofficient leads to a decreased water velocity near the bottom of the estuary. The extent to which this influences the water velocity's profile is dependent on the value of the vertical eddy viscosity $\hat{\mathcal{A}}_\mathrm{v}$, as shown in Figure 5.2b. The larger the value of $\hat{\mathcal{A}}_\mathrm{v}$, the larger the region of influence of the bottom friction.

## 5.4 The Effect of Bottom Friction and Exponential Convergence on the Resonance Properties of the Waterlevel

In this section, the influence of bottom friction and exponential convergence on the resonance properties of the leading order waterlevel is considered.[1] First of all, section 5.4.1 discusses the amplification properties of the waterlevel in a frictionless system with a constant width. Then, sections and consider the effects of bottom friction and exponential convergence separately. Lastly, the combined effect of the tow is discussed in section 5.4.4.

[1] The term *resonance* is only applicable in systems without friction. However, in this theses, "resonance properties" also refers to the strong amplification of tidal waves.

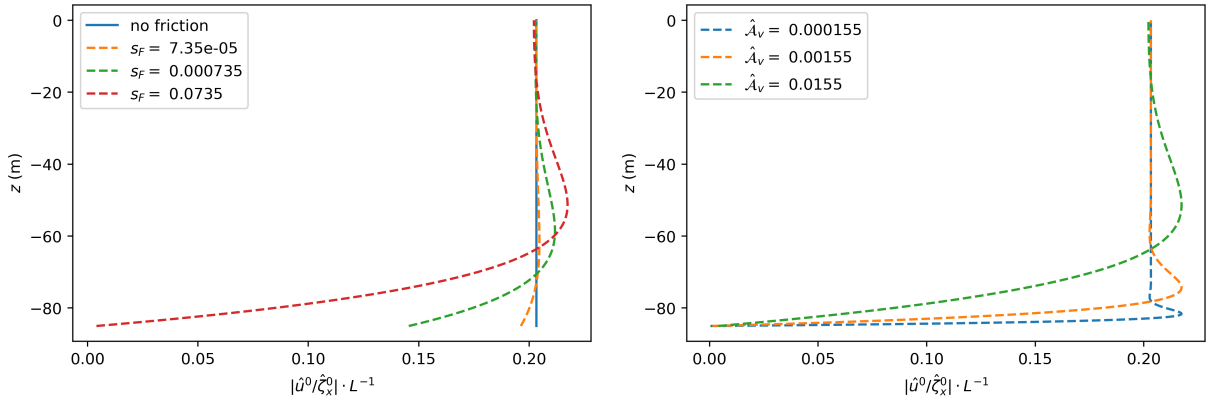


(a) The effect of bottom friction on the longitudinal water velocity's profile.

(b) The effect of vertical eddy viscosity on the longitudinal water velocity's profile.

Figure 5.2: The time-development of the leading order longitudinal water velocity and waterlevel. A darker colour corresponds to a later time-stamp.

### 5.4.1 A Frictionless System with Constant Width

In this section, the influence of bottom friction and exponential convergence on the leading order waterlevel in a system wihtout friction and with a constant width is analysed. We start by writing the solution (4.21) as the sum of an incoming wave and a reflected wave:

$$\zeta^0 = \frac{A_{M_2}\left(e^{-\frac{\sigma(x-L)}{c_0}+i\sigma t} + e^{\frac{\sigma(x-L)}{c_0}+i\sigma t}\right)}{\cos\left(\frac{\sigma L}{c_0}\right)} \tag{5.3}$$

where $c_0 = \sqrt{gH}$ is the frictionless wave velocity. Without friction, the system approaches a state of resonance when the denominator in this expression vanishes:

$$\cos\left(\frac{\sigma L}{c_0}\right) = 0, \tag{5.4}$$

which occurs if

$$\frac{\sigma L}{c_0} = \frac{(2n+1)\pi}{2} \quad \text{for some} \quad n \in \{0, 1, 2, ...\}. \tag{5.5}$$

This resonance condition can be interpreeted physically in multiple ways. One of those is by considering the propagation of a tidal wave through the estuary, and its interaction with the tidal forcing at the seaward side.

Figure 5.3 shows this wave-propagation schematically by distinguishing four steps. We assume that a wave starts at $x = 0$ when the tide at the seaward side is at its highest point. The first step shows the propagation of this wave through the estuary with a given velocity. For a frictionless system, this velocity is given by $c_0$, in which case the time $T_0$ needed to reach $x = L$ is given by

$$T_0 = \frac{L}{c_0}. \tag{5.6}$$

Step 2 shows the reflection of the tidal wave at $x = L$. In step 3, the wave moves back towards $x = 0$, and the time needed for that is again given by $T_0 = L/c_0$. In step 4, the wave has reach the seaward side again. Thus, for a frictionless system, this process takes a total time of $2T = 2L/c_0$ seconds.

For the system to be in resonance, the return of this tidal wave to the seaside (step four) must coincide with the moment at which the tide of the sea is at its lowest point. This occurs after half a tidal oscillation, but also after one and a half oscillations, two and a half oscillations, etc. Since the radial frequency of the tide is given by $\sigma$, a full oscillation takes $2\pi/\sigma$ seconds. Thus for the return of the tidal wave to coincide with a minimum of the tidal forcing at the seaside, one requires that

$$\frac{2L}{c_0} = \frac{(2n+1)\pi}{\sigma} \quad \text{for some} \quad n \in \{0, 1, 2, ...\}. \tag{5.7}$$

Note that this condition is equivalent to the (5.5). One can rewrite this condition by defining the frictionless wavelength $L_g := 2\pi c_0/\sigma$, leading to the well-known *quarter wavelength condition* for frictionless systems (De Swart, 2009, p.37):

$$L = \frac{L_g}{4}, \frac{3L_g}{4}, \frac{5L_g}{4}, ... \tag{5.8}$$

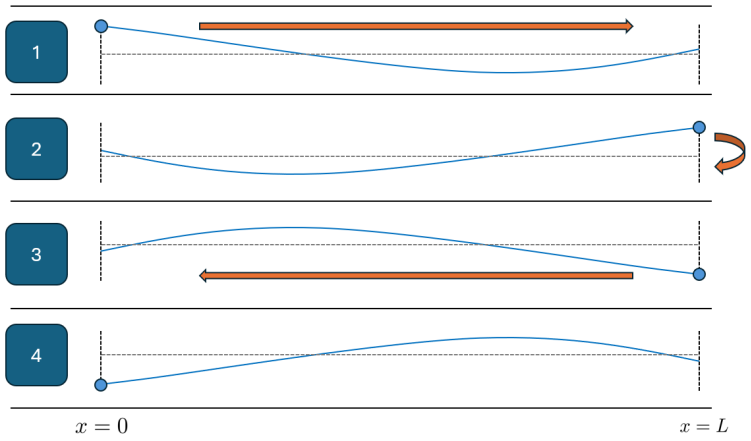


Figure 5.3: A schematic view of a tidal wave propagating through the estuary in four steps.

Figure 5.4 shows the maximum of the leading order waterlevel given by (5.3) as a function of $L$. The horizontal axis denotes $L/L_g$, where $L_g \approx 1305$ km. The figure shows that the amplification of the leading order waterlevel is indeed largest around $L/L_g = 1/4,\ 3/4,\ 5/4$.

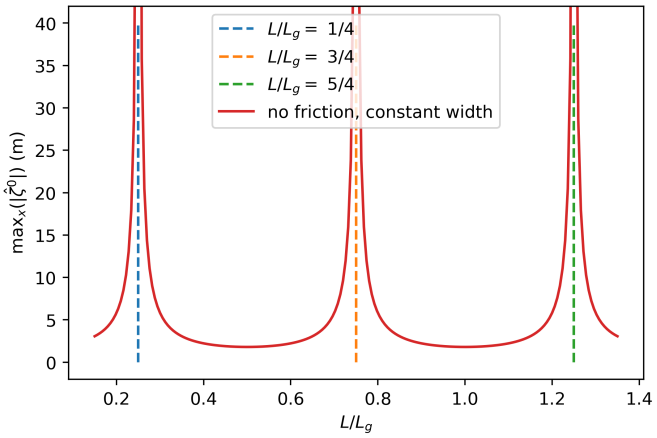


Figure 5.4: The maximum of the leading order waterlevel as a function of $L$ for a frictionless system with a constant width. The horizontal axis is scaled by the frictionless wavelength $L_g \approx 1305$ km.

### 5.4.2 A System with Bottom Friction and Constant Width

When bottom friction is introduced, the leading order waterlevel's expression (5.3) turns into:

$$\zeta^0 = \frac{A_{M_2}\left(e^{-\frac{\sigma(x-L)}{c_F}+i\sigma t} + e^{\frac{\sigma(x-L)}{c_F}+i\sigma t}\right)}{\cos\left(\frac{\sigma L}{c_F}\right)} \tag{5.9}$$

The frictionless wave velocity $c_0$ has been replaced by the complex-valued *frictional wave velocity* $c_F$ (see equation (4.22)). Figure 5.5 shows the effect of the bottom friction parameter $s_F$ on the wave velocity's real and imaginary value.

Due to the imaginary part of $c_F$ being nonzero in the presence of bottom friction, the denominator in (5.9) can no longer vanish. Therefore, true resonance can no longer occur, but the amplification of the waterlevel can still be large. Indeed, the steps for wave propagation in Figure 5.3 still apply, though the tidal wave's velocity is reduced due to energy loss at the bottom. The time for a tidal wave to reach $x = L$, reflect and return is now given by

$$2T_F = \frac{2L}{\mathrm{Re}(c_F)}. \tag{5.10}$$

As can be seen from Figure 5.5, the real part of $c_F$ has decreased, and thus a tidal wave in a system with bottom friction takes longer to propagate through the system than in a frictionless system. For amplification in this system

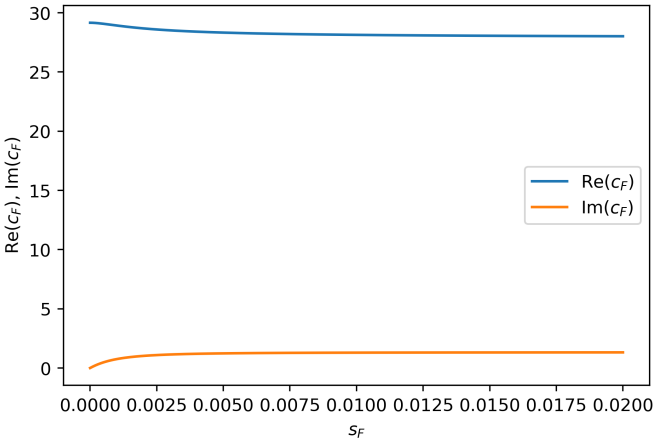


Figure 5.5: The real and imaginary part of the frictional wave velocity $c_F$ as a function of $s_F$.

to be maximal, one requires the following equality, similar to (5.7):

$$\frac{2L}{\mathrm{Re}(c_F)} = \frac{(2n+1)\pi}{\sigma} \quad \text{for some} \quad n \in \{0, 1, 2, ...\}. \tag{5.11}$$

Since the wave propagation in the presence of friction is slower, it follows that the estuary lengths $L$ for which this condition holds must be smaller. This effect is shown in Figure 5.6, in which the maximal amplification of the waterlevel is shown with and without bottom friction.

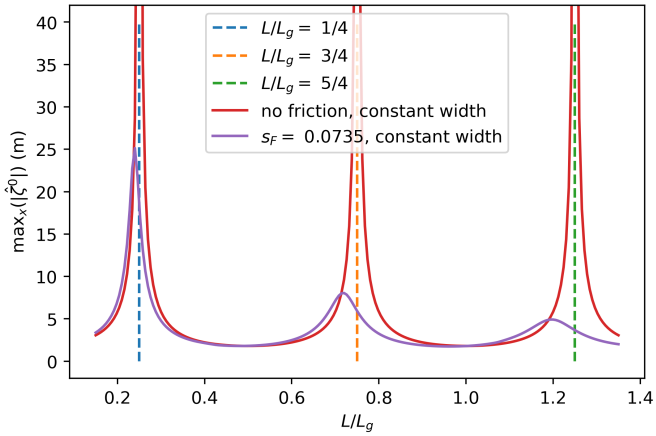


Figure 5.6: The maximum of the leading order waterlevel as a function of $L$ for a frictionless system and a system with friction, both with a constant width. The horizontal axis is scaled by the frictionless wavelength $L_g \approx 1305$ km.

Thus, the effect of the introduction of bottom friction on the amplification properties of the leading order waterlevel is summarised by two effects. One is that resonance no longer occurs, as the introduction of bottom friction damps the oscillations. However, amplification can still be large. Since bottom friction reduces the wave velocity, the maximal amplification in systems with bottom friction occurs for smaller estuary-lengths $L$ than in frictionless systems.

### 5.4.3 A Frictionless System with an Exponentially Convergencing Width

When in a frictionless system, exponential convergence with a convergence length $L_b$ is introduced, the leading order waterlevel's expression (5.9) becomes:

$$\zeta^0 = A_{M_2} \frac{\lambda_1^0 e^{\lambda_2^0(x-L)+i\sigma t} - \lambda_2^0 e^{\lambda_1^0(x-L)+i\sigma t}}{\lambda_1^0 e^{-\lambda_2^0 L} - \lambda_2^0 e^{-\lambda_1^0 L}}, \tag{5.12}$$

where

$$\lambda_{1,2}^0 = \frac{1}{2L_b} \pm i\sqrt{\frac{\sigma^2}{c_0^2} - \left(\frac{1}{2L_b}\right)^2}. \tag{5.13}$$

The effect of exponential convergence on the propagation of tidal waves through the systems is threefold. Firstly, it should be noted that, due to the exponential narrowing of the estuary, the waterlevel is amplified along the longitudinal axis. Secondly, the velocity of the tidal waves propagating through the system is decreased, and is now given by $\sqrt{\frac{\sigma^2}{c_0^2} - \left(\frac{1}{2L_b}\right)^2}$.[2] This has the effect that the time needed for steps 1 and 3 in Figure 5.3 is increased. However, the exponential convergence furthermore introduces a phase difference between the incoming wave and the reflected wave at $x = L$. This phase difference comes to light when determining the condition for resonance to occur by setting the denominator in (5.12) equal to 0:

$$-2L\sqrt{\frac{\sigma^2}{c_0^2} - \left(\frac{1}{2L_b}\right)^2} = \text{Arg}\left(\left(2\left(\frac{1}{2L_b}\right)^2 - \frac{\sigma^2}{c_0^2}\right) + i\left(\frac{1}{L_b}\sqrt{\frac{\sigma^2}{c_0^2} - \left(\frac{1}{2L_b}\right)^2}\right)\right) - 2n\pi \quad \text{for some} \quad n \in \{0, 1, 2, ...\}. \tag{5.14}$$

Thus, the values of $L$ for which resonance occur not only depend on the propagation speed of waves through the estuary, but are also influenced by the phase difference between the incoming and reflected wave that occurs in step 2 in Figure 5.3. Figure 5.6 shows the effect of exponential convergence on the amplification properties of the leading order waterlevel by displaying the leading order waterlevel as a function of the estuary length $L$. Thus,

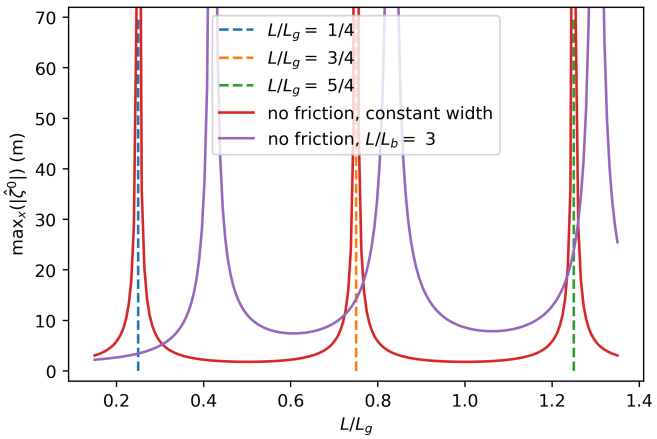


Figure 5.7: The maximum of the leading order waterlevel as a function of $L$ for a frictionless system with a constant width and with an exponentially converging width. The horizontal axis is scaled by the frictionless wavelength $L_g \approx 1305$ km.

an exponentially converging width causes the amplification of the leading order waterlevel to be maximal for larger values of $L$, due to a combination of a slower wave propagation and a phase difference between the incoming and the reflected wave at $x = L$.

### 5.4.4 A System with Bottom Friction and an Exponentially Converging Width

The combined effect of bottom friction and an exponentially converging width leads to the following expression for the leading order waterlevel:

$$\hat{\zeta}^0 = A_{M_2}\frac{\lambda_1^F e^{\lambda_2^F(x-L)+i\sigma t} - \lambda_2^F e^{\lambda_1^F(x-L)+i\sigma t}}{\lambda_1^F e^{-\lambda_2^F L} - \lambda_2^F e^{-\lambda_1^F L}}, \tag{5.15}$$

where

$$\lambda_{1,2}^F = \frac{1}{2L_b} \pm i\sqrt{\frac{\sigma^2}{c_F^2} - \left(\frac{1}{2L_b}\right)^2}. \tag{5.16}$$

Bottom friction causes resonance to turn into strong amplification, and slows down the propagtion of waves, as discussed in section 5.4.2. Exponential convergence also slows down the waves, but furthermore introduces a phase difference between the incoming wave and the reflected wave at $x = L$, as discussed in section 5.4.3. The combined effect of the two is presented in Figure 5.8, where bottom friction and exponential convergence are introduced, and the maximal leading order waterlevel is shown as a function of $L$.

[2] Note that if $\left(\frac{1}{2L_b}\right)^2 > \frac{\sigma^2}{c_0^2}$, the solution is exponential.

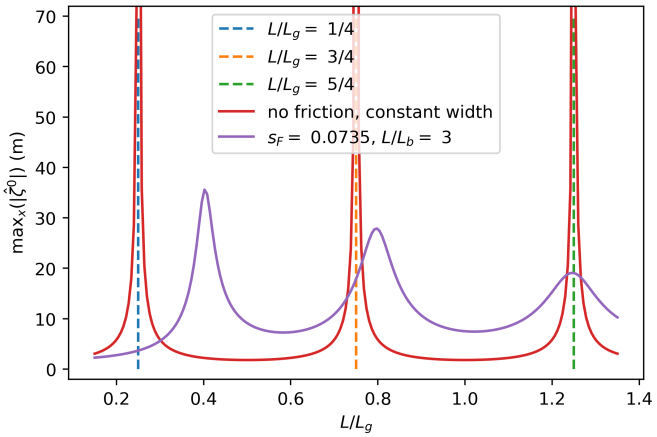


Figure 5.8: The maximum of the leading order waterlevel as a function of $L$ for a frictionless system with a constant width and with an exponentially converging width. The horizontal axis is scaled by the frictionless wavelength $L_g \approx$ 1305 km.

# Chapter 6

# The Effect of Landfast Ice

In this chapter, the effect of landfast ice on the large-scale leading order hydrodynamics is studied. In section 6.1, the effect of several ice coverages on the hydrodynamics in Cook Inlet is analysed. To understand the behaviour shown in Cook Inlet and to understand what effect ice coverage has on general estuaries, the effect of the percentage of ice coverage on resonance properties of the tide is analysed in section 6.2.

## 6.1 Landfast Ice in Cook Inlet: Variable Coverage

According to Mulherin et al. (2001, p.26-34), the ice coverage within Cook Inlet can vary between 10% and 50% from December through March. As a first step in analysing the effect of ice on the tidal hydrodynamics, it is assumed that the ice cover consists of solely landfast ice. The ice cover is assumed to start at $x = x_I$ and reach the landward side of the estuary $x = L$; see Figure 6.1. Table 5.1 gives the values that are applied within the model. Furthermore, it is assumed that the ice friction parameter $s_I$ is equal to the bottom friction parameter $s_F$.

For the leading order longitudinal water velocity at $x/L = 0.3$, $x/L = 0.7$ and $x/L = 0.95$, Figure 6.4 shows its depth-profiles. Two effects of the landfast ice are notable. When ice is present at the water's surface, the water's velocity decreases near the surface in a way that is symmetric to the effect of the bottom friction. This behaviour is expected, since the two partial slip conditions have a symmetric effect - specially when $s_I = s_F$. When no landfast ice is present, the free slip condition requires the vertical gradient of $\hat{u}^0$ to vanish near the surface, leading to a vertically uniform profile outside of the region where the flow is affected by the bottom.

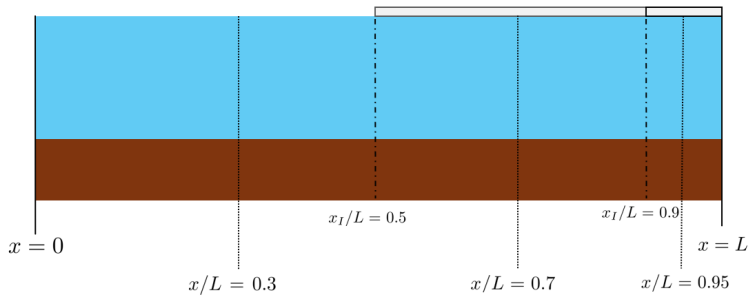


Figure 6.1: A schematic side-view of an estuary that is partially covered by landfast ice. The values for $x/L$ that are used later in the text are indicated, as well as the values that are used for $x_I/L$.

Figure 6.2 shows the leading order waterlevel along the estuary for the parameter values given in Table 5.1 for three cases: no ice, an ice coverage of 10% ($x_I/L = 0.9$), and an ice coverage of 50% ($x_I/L = 0.5$). It can be seen that for a larger ice coverage, the leading order waterlevel is amplified.

To see whether all landfast ice coverages will amplify the waterlevel in Cook Inlet, Figure 6.3 shows

## 6.2 The Influence of Coverage by Landfast Ice in General Estuaries

One might wonder whether the coverage by landfast ice generally results in amplifying the leading order waterlevel. To analyse that, Figure 6.3 shows the maximum of the leading order waterlevel as a function of $x_I/L$. From this

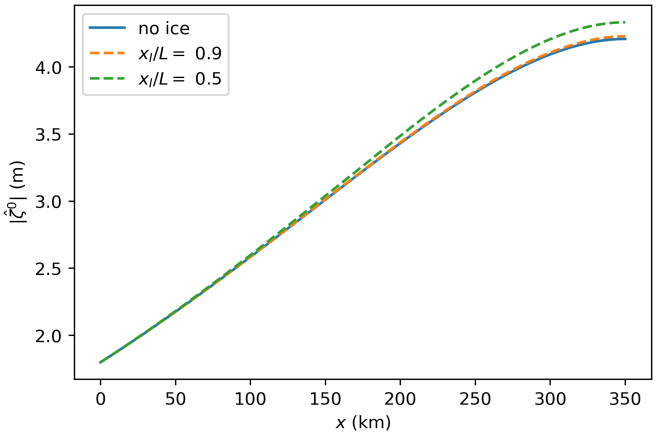


Figure 6.2: The leading order waterlevel in Cook Inlet for several landfast ice coverages. The ice friction parametr $s_I$ is assumed to equal the bottom friction parametr $s_F$.

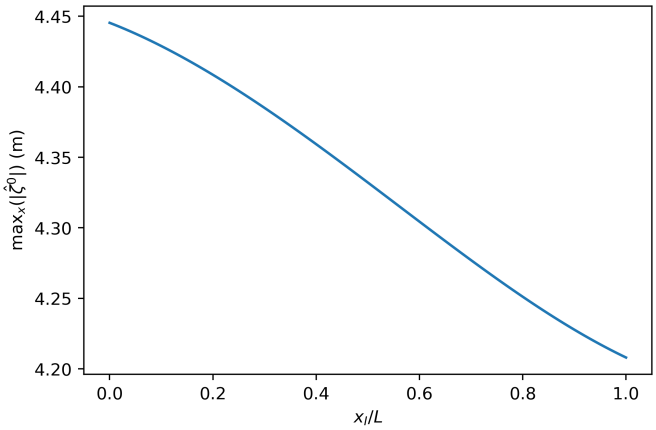


Figure 6.3: The maximal leading order waterlevel as a function of $x_I/L$ in Cook Inlet.

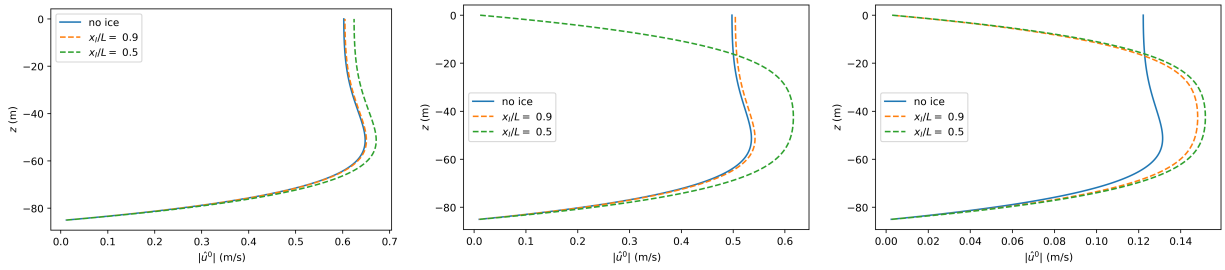


(a) At $x/L = 0.3$. (b) At $x/L = 0.7$. (c) At $x/L = 0.95$.

Figure 6.4: The leading order longitudinal water velocity in Cook Inlet at various $x$-coordinates for three cases: no ice, 10% landfast ice coverage and 50% landfast ice coverage. The $x$-coordinates are indicated in Figure 6.1.

figure, it is clear that an increased landfast ice cover (decreasing $x_I - L$) indeed leads to an amplified leading order waterlevel for the parameter settings given in Table 5.1 and several values of the ice friction parameter $s_I$.

To analyse why the increase of landfast ice coverage leads to an amplified waterlevel, the resonance properties of the system are examined. Figure 6.5 shows the maximum of the leading order waterlevel as a function of the estuary-length $L$, similar to the plots shown in section 5.4. The maximum of the waterlevel is shown for various ice coverages. Furthermore, the estuary-length of Cook Inlet is indicated by the dotted line.

Figure 6.5a shows that the effect of an increased ice coverage is twofold. One effect is that for an increased ice coverage, the heights of the amplification peaks decrease. As can be seen, for estuary-lengths in between $0.375L_g \approx$ 490 km and $0.450L_g \approx 585$ km, this leads to a decrease in the maximal waterlevel. However, another effect is that for an increased ice coverage, the amplification peaks shift towards larger values of $L$. As can be seen in Figure 6.5b,

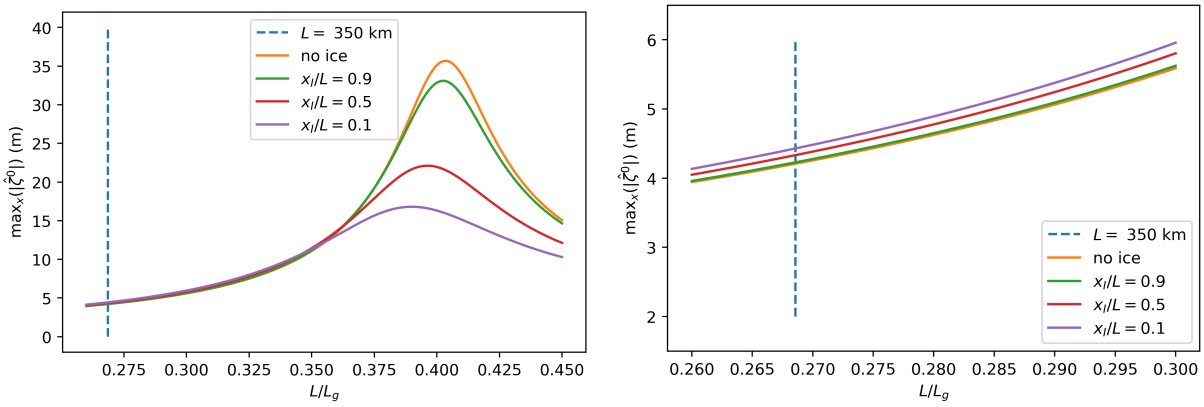


(a) $L$ varies from $0.26L_g$ until $0.44L_g$.

(b) $L$ varies from $0.26L_g$ until $0.3L_g$.

Figure 6.5: The maximal leading order waterlevel as a function of the estuary-length $L$ for various values of $x_I/L$. The horizontal axis is scaled by the frictionless wavelength $L_g \approx 1305$ km.

this is the effect that causes the amplification of the waterlevel in Cook Inlet when more landfast ice is present.

To further analyse the effect of ice coverage on estuaries, Figure 6.6 shows the following information:

1. The estuary-lengths are shown on the horizontal axis, and are scaled with the frictionless wavelength $L_g \approx 1305$ km. The vertical axis shows how much of the estuary is covered by landfast ice, i.e. $x_I/L$.
2. For each combination of estuary-length and ice coverage, the shade of green indicates the maximum of the leading order waterlevel. A darker green corresponds to a larger waterlevel.
3. For al estuary-lengths lengths, the red curve gives the amount of ice coverage that yields the largest waterlevel.
4. For all ice coverages, the blue curve indicates the estuary-length for which amplification is maximal.
5. Cook Inlet's length $L = 350$ km is indicated by the dashed blue line.
6. The dashed grey lines show the values of $x_I/L$ for which the maximum of the waterlevel is shown in Figure 6.5a.

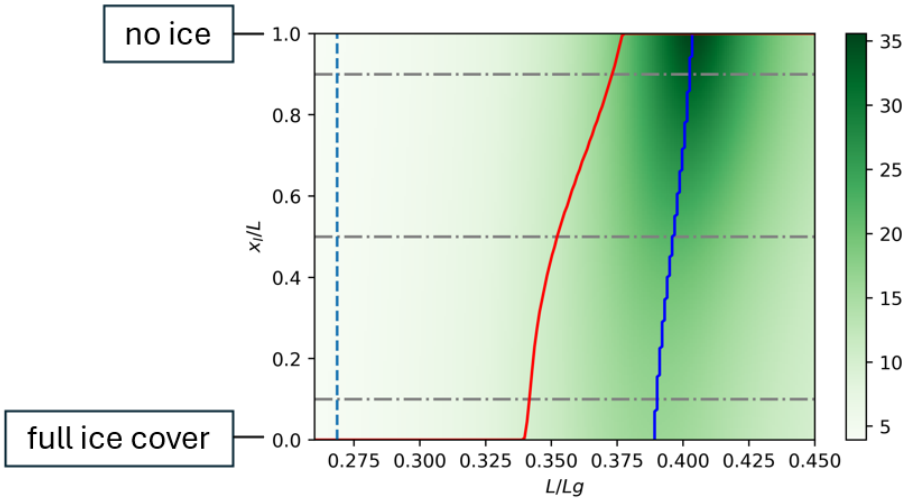


Figure 6.6: A colourplot showing the maximal leading order waterlevel as a function of the estuary-length $L$ and the percentage of coverage $x_I/L$. A darker green colour corresponds to a larger maximal waterlevel. The red curve indicates which ice coverage yields the largest maximal amplitude for each value of $L$. The blue curve indicates for each ice coverage what the value of $L$ is for which the amplification is maximal. The dashed blue line corresponds to Cook Inlet's estuary-length $L = 350$ km. The dashed grey lines correspond to the ice-coverages that are shown in Figur 6.5. The horizontal axis is scaled with the frictionless wavelength $L_g$, where $L_g \approx 1305$ km.

The blue curve in Figure 6.6 indicates that indeed, for increased landfast ice coverages, the amplification peak shifts

towards smaller values of $L$. Furthermore, the red curve confirms that for $L$ smaller than approximately $0.3L_g \approx$ 390 km, the amplification of the tide is maximal when the estuary is fully coverd in ice, and for $L$ larger than $0.375L_g \approx$490 km, the amplification is maximal without an ice cover. When the length of the estuary is in between these values, there is a nontrivial landfast ice coverage for which the amplification of the tide is maximal.

The decrease of the amplification peaks for increasing ice coverages can be explained by the energy-loss caused by the ice-friction. The shift of these peaks towards smaller values of $L$ can be explained by considering the propagation of tidal waves through the estuary, as explained in section 5.4. Indeed, for a given ice coverage, the tidal wave has wave velocity $\mathrm{Re}(c_F)$ for $0 < x < x_I$ and $\mathrm{Re}(c_{FI})$ for $x_I < x < L$, where $c_F$ and $c_{FI}$ are given in (B.2) and (4.22).

Figure 6.7 shows the dependency of $\mathrm{Re}(c_{FI})$ on the ice friction parameter $s_I$. It can be seen that due to ice friction, the real part of $c_{FI}$ decreases. In other words, the velocity at which the wave propagates through the system decreases due to ice friction. Therefore the time $T_{FI}^{x_I}$ needed for a tidal wave to propagate through the system increases when the landfast ice cover is larger. From section 5.4, we know that the requirement for maximal amplification of the tide is given by

$$2T_{FI}^{x_I} = \frac{(2n+1)\pi}{\sigma} \quad \text{for some} \quad n \in \{0, 1, 2, ...\}, \tag{6.1}$$

where $2T_{FI}^{x_I}$ denotes the time needed for a tidal wave to propagate to the landward side and back towards the seaward side. For every estuary-length $L$, this time increases as the percentage of ice coverage increases. Therefore, the estuary length that satisfies the condition (6.1) must shrink as the ice coverage increases. Furthermore, it should

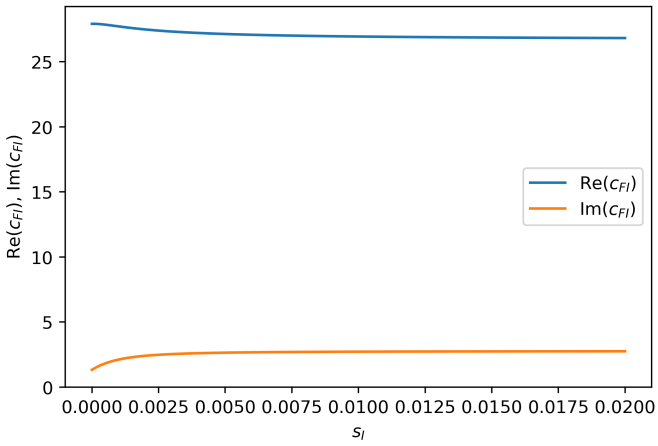


Figure 6.7: The real and imaginary part of the frictional wave velocity $c_{FI}$ as a function of $s_I$.

be noted that $T_{FI}^{x_I}$ also depends on the convergence length $L_b$. When an estuary has a different convergence length, its resonance properties are changed, and therefore, the effect of an increased landfast ice coverage is expected to be different.

Summarising, we have found that for increasing ice covers, the effect on the amplification of tidal waves in estuaries is twofold. Due to increased energy-loss, the maximal amplification of the tides decreases. Furthermore, due to tidal waves propagating at a lower velocity when the ice cover is increased, the estuary-lengths for which these maximal amplifications occur decrease as well. The combined effect of the two determines whether an increased ice coverage increases or decrases the waterlevel in a given estuary, depending on the length of the estuary and on the convergence length.

# Chapter 7

# The Effect of Ice Floes in the Horizontal Shear Region

In this chapter, the effect of ice floes in the horizontal shear region of the leading order tidal waves and currents is analysed. In section 7.1, the parameter values that correspond to the effect of ice floes are given. In section 7.2, the influence of several ice floe coverages in Cook Inlet is analysed. These results are clarified in section 7.3 by considering the effect of ice coverage on the resonance properties of more general estuaries. All approximations in this chapter are computed using $N_x = 200$ and $N_a = 6$.

## 7.1 Parameter Values

The parameter values used in the experiments below are given in Table 7.1, together with the values in Table 5.1. The values, given in the former table, are used to calculate $\eta$, which indicates the strength of the horizontal viscosity due to the ice floes.

This section presents the effect ice floes is various settings on the leading order longitudinal water velocity and the waterlevel in a model for Cook Inlet. The parameter values from Table 5.1 are used, in addition to the values in Table 7.1. Based on the values form the table, the ice's horizontal shear is taken to be

$$\eta = \frac{5 \cdot 10^9}{16} e^{-20(1-A)}. \tag{7.1}$$

In contrast to the setting in the previous chapter, it is assumed that the ice covers in Cook Inlet only consists of ice floes. For that, we introduce the following functions for the thickness of the ice and the top-layer parametrisation $F$.

1. The ice thickness is modelled by the following function:

$$h_I(x_I, x) := \frac{\tanh\left((x - x_I) \cdot 10^{-4}\right) + 1}{2}, \tag{7.2}$$

   where we have assumed that the thickness varies between 0 and 1. Figure 7.1a shows the function for various ice coverages.

2. The thickness of the layer near the surface of the region in which ice floes cause an increased viscosity is assumed to be 1/10th of the estuary's depth. Therefore, the parameter $F$ is modelled as:

$$F(z) = \frac{\tanh\left(z + \frac{H}{10}\right) + 1}{2}, \tag{7.3}$$

   Figure 7.1b whows $F$ as a function of the depth.

Furthermore, it is assumed that the ice floes' compactness satsfies $A = 0.9$ and that the maximum viscous creep parameter is equal to $D_0 = 10^{-6}$.

| Quantity | Symbol | Value | Source |
|---|---|---|---|
| Compressive strength of compact ice of unit thickness | $P^*$ | $5 \cdot 10^3$ N/m | Hibler III (1979, p.825) |
| Strength reduction constant for lead opening | $C$ | 20 | Hibler III (1979, p.825) |
| Maximum viscous creep parameter | $D_0$ | $10^{-7}$ to $10^{-6}$ s$^{-1}$ | Vasulkar (2024, p.81) |
| Aspect ratio of the yield ellipse of the ice's rheology | $e_c$ | 2 | Hibler III (1979, p.825) |
| Horizontal eddy viscosity | $\hat{\mathcal{A}}_{\mathrm{h}}$ | 0.1-10 m$^2$/s | De Swart (2009, p.21) |
| Ice thickness | $h_I$ | 0.5-2 m | Mulherin et al. (2001, p.13) |
| The ice's horizontal shear | $\eta = \frac{P^* h_I e^{-C(1-A)}}{4 D_0 e_c^2}$ | $\frac{0.25}{16} \cdot 10^9 - \frac{10}{16} \cdot 10^{10}$ m$^2$/s if $A = 1$, and smaller if $0 < A < 1$ | equation (2.19) |

Table 7.1: The values of the parameters used for modelling the effect of ice floes in Cook Inlet.

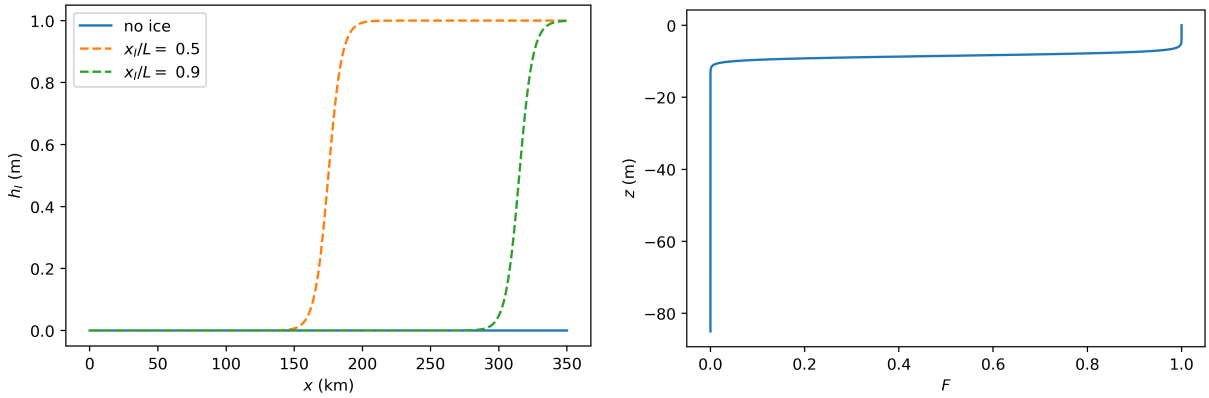


(a) The ice-thickness function for various values of $x_I/L$. (b) The parametrisation of the top-layer in which ice floes cause an increased horizontal viscosity.

Figure 7.1: The functions that are applied to model the effect of ice floes in the horizontal shear zone.

## 7.2 The Effect of Ice Floe Coverages in Cook Inlet

To illustrate the influence of a 10% and a 50% ice floe cover on the leading order waterlevel in the model for Cook Inlet, the amplitude of the free surface elevation is shown in Figure 7.2 as a function of $x$. It is clear that the 10% ice cover mostly influences the waterlevel by a small increase of the amplitude near the head of the inlet. This effect is enhanced when the estuary is covered for 50% by ice floes.

The effect of these ice floe covers on the leading order longitudinal water velocity is shown in Figure 7.3. As can be seen, the introduction of ice floes has the effect of increasing the velocity in the middle of the core region and decreasing the velocity within the ice-floe region near the surface. This effect on the water velocity's profile bears a similarity with the effect of landfast ice, as shown in Figure 6.4. However, the ice floes reduce the velocity in a larger layer below the surface than landfast ice. This implies that the energy-loss due to ice floes with a compactness of $A = 0.9$ is generally larger than the energy-loss due to landfast ice with friction parameter $s_I = 0.07350$.

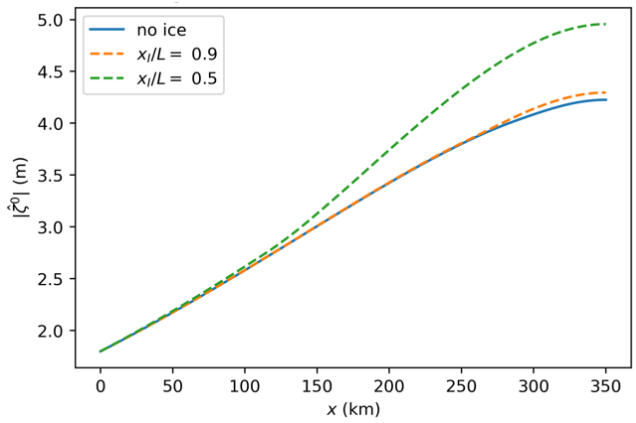


Figure 7.2: The influence of a 10% and a 50% ice floe cover on the leading order waterlevel in Cook Inlet.

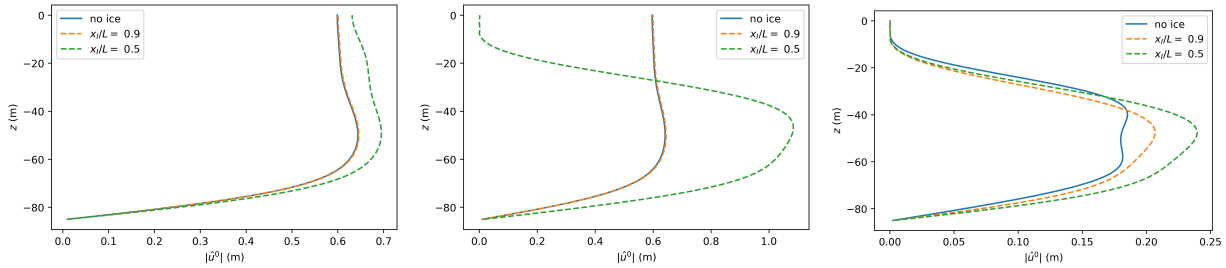


(a) At $x/L = 0.3$. (b) At $x/L = 0.7$. (c) At $x/L = 0.95$.

Figure 7.3: The leading order longitudinal water velocity at various $x$-coordinates for three cases: no ice, 10% ice floe coverage and 50% ice floe coverage. The presented $x$-coordinates are indicated in the schematic view in Figure 6.1.

## 7.3 The Influence of Coverage by Ice Floes in General Estuaries

To explain why the ice floe coverages cause an amplification of the free surface level in Cook Inlet, we turn to the resonance properties of estuaries under the influence of ice floe covers. Indeed, similar to Figure 6.5a, Figure 7.5 shows the maximal waterlevel in estuaries as a function of the estuary-length $L$ for several ice coverages. It is clear that the effect of ice floes on the resonance peaks is similar to the effect of landfast ice: for a larger ice cover, the maximal amplification peak decreases and shifts towards smaller values of $L$. This effect is can likely be explained by the energy-loss due to the enhanced horizontal viscosity in the upper layer of the water column due to ice floes, leading to a damping of the tide. Furthermore, the increased viscosity leads to a smaller wave velocity, so that - following the explanation from section 5.4 - the time required for a tidal wave to propagate from $x = 0$ to $x = L$, reflect, and move back to $x = 0$ is longer, thus requiring a shorter estuary-length to satisfy the requirement of maximal amplification given by (6.1).

To extend these results to general ice coverages, Figure 7.5 shows a colourplot of the maximum of the free surface elevation. Like in figure 6.6, the following information is shown:

1. The estuary-lengths are shown on the horizontal axis, and are scaled with the frictionless wavelength $L_g \approx 1305$ km. The vertical axis shows how much of the estuary is covered by landfast ice, i.e. $x_I/L$.
2. For each combination of estuary-length and ice coverage, the shade of green indicates the maximum of the leading order waterlevel. A darker green corresponds to a larger waterlevel.
3. For al estuary-lengths lengths, the red curve gives the amount of ice coverage that yields the largest waterlevel.
4. For all ice coverages, the blue curve indicates the estuary-length for which amplification is maximal.
5. Cook Inlet's length $L = 350$ km is indicated by the dashed blue line.
6. The dashed grey lines show the values of $x_I/L$ for which the maximum of the waterlevel is shown in Figure 7.5.

The blue curve in this figure indeed shows the decreasing trend of the estuary-lengths $L$ for which amplification

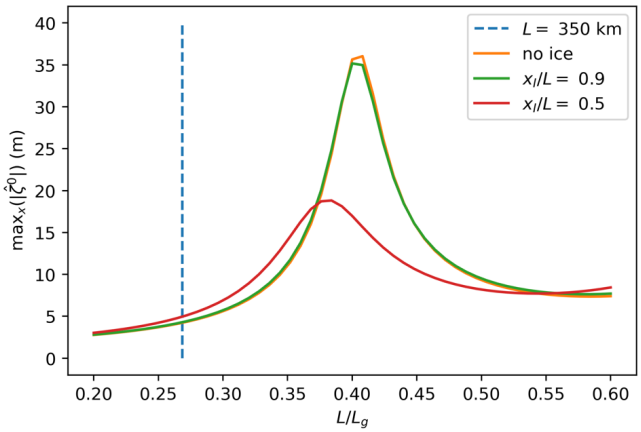


Figure 7.4: The maximal leading order waterlevel as a function of the estuary-length $L$ for various values of $x_I/L$. The horizontal axis is scaled by the frictionless wavelength $L_g \approx 1305$ km.

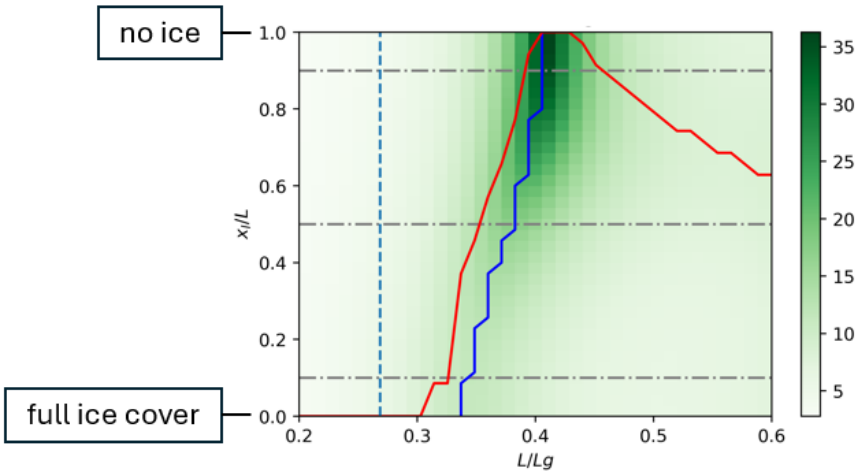


Figure 7.5: A colourplot showing the maximal leading order waterlevel as a function of the estuary-length $L$ and the percentage of coverage $x_I/L$. A darker green colour corresponds to a larger maximal waterlevel. The red curve indicates which ice coverage yields the largest maximal amplitude for each value of $L$. The blue curve indicates for each ice coverage what the value of $L$ is for which the amplification is maximal. The dashed blue line corresponds to Cook Inlet's estuary-length $L = 350$ km. The dashed grey lines correspond to the ice-coverages that are shown in Figur 6.5. The horizontal axis is scaled with the frictionless wavelength $L_g$, where $L_g \approx 1305$ km.

of the free surface level is maximal. Furthermore, the red curve shows that for estuary-lengths $L$ smaller than approximately $0.3L_g \approx 390$ km, amplification of the tide is maximal for a full ice floe cover, and for estuary-lengths close to $0.4L_g \approx 520$ km, amplification is maximal without ice. For all other estuary-lengths in Figure 7.5, there is a specific value for which the waterlevel is maximally amplified. For the values larger than $0.4L_g$, this is likely cause by the shift of a second resonance peak towards smaller values of $L$.

Concluding, we have found that the effect of ice floe coverage on the amplification or attenuation of the tides in estuaries is similar to that of landfast ice coverage: the maximal amplification peak shifts towards smaller values of $L$, and the height of these peaks decreases due to energy-loss as a consequence of the ice floes. However, this effect is larger for ice floes with compactness $A = 0.9$ than for landfast ice with ice friction coefficient $s_I = 0.07350$. This is probably a consequence of the fact that the ice floes reduce the longitudinal water velocity for a larger part than landfast ice, as is seen by comparing Figures 7.3 and 6.4.

# Chapter 8

# Conclusion

In this thesis, a two-dimensional model describing the effect of landfast ice and ice floes on the large-scale hydrodynamics in an estuary was developed. The linear effect of the $M_2$-tide on the width-averaged leading order longitudinal water velocity and waterlevel has been analysed in two cases: when only landfast ice is present, and when only ice floes with a negligible vertical shear force are present. The effect of landfast ice was modelled by a partial slip condition at the water's surface, and the ice floes were modelled by an increased horizontal viscosity in the top-layer of the water.

The two different cases were solved independently. Solutions to the model with only landfast ice were found analytically in the frequency-domain by computing the depth-profile of the leading order longitudinal water veolcity in terms of the local waterlevel's gradient, using the partial slip conditions due to bottom- and ice-friction. Subsequently integrating the continuity equation over the depth of the estuary led to an ODE for the leading order waterlevel, which was solved analytically under the assumptions of a constant estuary-depth and -width. For the ice floe model, solutions in the frequency-domain were approximated using a combination of a spectral method and a finite difference method. The spectral method was applied in the $z$-direction, allowing for a representation of the depth-profile of the longitudinal velocity in terms of eigenfunctions that satisfy the partial slip condition at the bottom. The finite-difference method was applied to solve the the longitudinal direction of the coupled leading order water velocity and waterlevel.

The effect of landfast ice coverage in Cook Inlet was studied by analysing the influence of the degree of ice coverage on the leading order waterlevel. For the case of Cook Inlet in particular, an increasing percentage of landfast ice coverage led to an increased waterlevel. This effect was explained by the fact that for increasing ice coverage, the system got closer to resonance. Furthermore, it was shown that for general estuaries, the effect of the degree of landfast ice coverage is highly dependent on the length of the estuary and the degree of (exponential) convergence, since these factors determine whether the systems moves away from or closer to resonance when the ice coverage is increased.

The influence of ice floe coverage in the horizontal shear region in Cook Inlet was studied by analysing the effect of the percentage of ice coverage by ice floes. Again, the model for Cook Inlet led to an increase of the leading order waterlevel as the ice coverage increased, as a consequence of the system getting closer to resonance. The influence of this ice floe coverage on the amplification of the tide was also highly dependent on the length of the estuary, which has a great influence on whether the system moves closer to resonance or away from it.

# Chapter 9

# Discussion and Future Work

The model that was introduced in this thesis and the results that follow from it give insight in the influence of ice coverage on the water motions in estuaries such as Cook Inlet. There are, however, limitations to the work done here. Recommendations for further invstigation are given below, along with discussions on the relevance of the results presented in this thesis.

1. **Calibrate the model parameters by using data from Cook Inlet.** The choice of parameters for modelling Cook Inlet is only verified by comparing the waterlevel at the head of the Inlet to the modelled leading order waterlevel, and by noticing that depths of 85 m do occur in Cook Inlet. The convergence length $L_b = L/3$ has been estimated by capturing the development of the cross-sectional area in the exponential convergence of the width. These estimations are rough, and therefore, the accuracy of the results in this thesis is not optimal. Still, the results and methods are of value for predicting the influence of ice coverages on the estuary's amplification properties, as the variation of parameters and the explanation of the results give insight in the effects of ice covers. A more elaborate comparison with measurements can lead to a better calibration for the convergence length, vertical eddy viscosity, bottom friction parameter and width-averaged estuary-depth. Since Chapters 6 and 7 explain what the effect of the convergence length and degree of ice coverage is on the amplification properties of the tidal waves, the attenuation or amplification properties of tidal waves with this new calibration can be predicted using that same analysis.

2. **Systematically analyse the effect of different parameters describing the estuary's and the water's characteristics.** In addition to a better calibration of the parameters, it can prove useful to systematically analyse the effect of the (constant) parameters $H$, $\hat{\mathcal{A}}_{\mathrm{v}}$ and $s_F$ on the effects of ice on the water velocity and waterlevel. Indeed, a better understanding of the effect of these parameters can lead to a better understanding of the amplification properties of the water, as it will be clear whether and how the choice of these parameters influence the results presented in Chapters 6 and 7.

3. **Systematically analyse the effect of different parameters describing the ice floes' characteristics.** The influence of ice floes in the horizontal shear zone is only done for certain parameter settings, where a decision is made for the value of $D_0$, the ice compactness $A$, the ice thickness $h_I$, and the thickness of the top-layer in which ice floes induce an amplified horizontal viscosity. Although these values have been taken within their physically relevant ranges, their effects are greatly generalised in doing so, and thus may be over- or underestimated. Therefore, it is recommended that in future research, these parameters are systematically varied, so that the consequences of choosing a certain parameter setting can be understood. Furthermore, by spatially varying the ice compactness and the ice thickness in different ways, the effect of more specific ice floe coverages can be modelled, allowing for a better understanding of the influence of these parameters.

4. **Investigate the effect of combined landfast ice and ice floe coverages.** In this thesis, a clear distinguishment is made between the effects of landfast ice and the effect of ice floes in the horizontal shear region on the leading order hydrodynamics in estuaries. However, in practice, these different types of ice do occur simultaneously in estuaries such as Cook Inlet. Therefore, to better predict the effect of different ice coverages on estuaries, the combined effect of the landfast ice and ice floes - both in the horizontal shear and the vertical shear region - must be analysed. This can be done by, for example, applying a spectral method similar to the method described in section 4.2 to a model in which the shear friction at the surface is not neglected.

5. **Investigate the effect of $x$-dependent parameters.** The effects on the large-scale hydrodynamics that were presented and discussed in this thesis are limited by the assumptions made in creating the two-dimensional model, distinguishing between the influence of types of ice, and finding solutions and approximations describing

the tidal water motion influenced by ice. As mentioned before, by further calibrating the model parameters, it can be verified whether the effect of ice is well-captured by the solutions and approximations shown in this thesis. Furthermore, combining the effect of landfast ice and ice floes will increase the chances of capturing the large-scale effects of ice well. In case one wants to proceed in using the model presented in this thesis to capture large-scale effect of ice in more specific situations, it is recommended to start by making parameters, such as the depth $H$ and the bottom friction parameter $s_F$, dependent on the longitudinal coordinate, and making the width $\Delta$ dependent on the longitudinal coordinate in a different way than by exponential convergence. This does have the consequence that, for general functions $H(x)$, $s_F(x)$ and $\Delta(x)$, the solution to the ODE for the leading order waterlevel (4.12) must be approximated numerically.

In line with this, one can choose to make the ice friction parameter $s_I$ dependent on $x$, allowing for the effect of different kinds of landfast ice coverages to be modelled, instead of the ice coverage only being able to start at $x = x_I$. Furthermore, this allows for the effect of different landfast ice-thicknesses and -roughnesses to be taken into account. However, also for general functions $s_I(x)$, the ODE for the leading order waterlevel (4.12) cannot be solved analytically, and a numerical method must be applied.

6. **Increase the accuracy of the model by making less simplifications of the Navier-Stokes Equations.** It is important to note that, due to the strong idealised nature of the model, its results will not be able to capture the effects of ice coverage on the even more detailed, small-scale water motion. To model those effects, it is recommended that one makes less or no assumptions to simplify the Navier-Stokes Equations (2.1).

7. **Include more complex behaviour of the ice floes' rhoelogy and their interaction with the estuary's boundaries.** In parametrising the effect of ice floes on the water motion in an estuary, the rheology of ice floes is greatly simplified by only taking into account the linear viscous term. Furthermore, when width-averaging, it is assumed that the boundary has a negligible effect on the large-scale width-averaged hydrodynamics. It is interesting to investigate further whether leaving out some of these assumptions has a notable influence on the results shown in this thesis.

8. **Investigate the effect of ice on the residual flow by solving the first order model.** The perturbative method described in Chapter 3 allows one to capture the effect of ice of the large-scale hyrdodynamics induced by a semidiurnal tides. Though the focus of this thesis has been to analyse the effect of this dominant tide by solving the leading order model, when one is interested in the effect of ice on the residual flow of particulate matter or sediment, the first order model (i.e. the model corresponding to order $\mathcal{O}(\epsilon)$ must be analysed. A method to do so is described by Chernetsky et al. (2010, p.127-130), for a case without ice.

9. **Analyse the convergence properties of the spectral method in case ice floes are present.** For the spectral method that is applied to approximate the hydrodynamics under the influence of ice floes in the horizontal shear region, the convergence of the approximation towards the analytical solution is shown only in case no ice is present. However, when ice is present, the convergence of the solution is not analysed. The convergence without ice does not give an indication as to whether the convergence when ice floes are included is equally reliable, and this convergence is highly dependent on the interaction between the top-layer parametrisation $F$ and the eigenfunctions. Further research on this convergence behaviour is necessary to establish more trust in the results.

10. **Reduce computational costs for the solution method of the model describing ice floes in the horizontal shear region.** The numerical method that was used for approximating solutions to the model describing the effect of ice floes in the horizontal shear zone is computationally quite expensive. Applying methods, such as preconditioning, to reduce computational costs allows for a more systmatic and less time-consuming way to analyse the effect of ice floes.

# Appendix A

# Averaging Procedures

In this Appendix, the Reynolds- and width-averaging procedures are written out.

## A.1 Reynolds-Averaging

We wish to rewrite the system (**??**) into a Reynolds-averaged system of equations. For this, we make use of the Reynoldsdecomposition, being defined by an ensemble average (see (2.2)). For any function $\alpha(x, y, z, t)$, the averaging procedure satisfies the following *Reynolds decomposition*:

$$a = \langle a \rangle + a', \tag{A.1}$$

where $\langle a \rangle$ is the Reynolds average and $a' := a - \langle a \rangle$ denotes the (statistical) fluctuations with respect to the Reynolds average. We will apply the operation $\langle \cdot \rangle$ to the equations in (**??**). In order to do so, we make use of the following properties (Rozendaal (2019), p. 8):

$$\langle \langle a \rangle \rangle = \langle a \rangle, \quad \langle \gamma a + \zeta b \rangle = \gamma \langle a \rangle + \zeta \langle b \rangle, \quad \langle \langle a \rangle b \rangle = \langle a \rangle \langle b \rangle, \quad \langle \partial_s a \rangle = \partial_s \langle a \rangle, \tag{A.2}$$

for $s = x, y, z, t$. Note that it follows that

$$\begin{aligned} \langle a' \rangle &= \langle a - \langle a \rangle \rangle && \text{(A.3)} \\ &= \langle a \rangle - \langle \langle a \rangle \rangle && \text{(A.4)} \\ &= \langle a \rangle - \langle a \rangle && \text{(A.5)} \\ &= 0. && \text{(A.6)} \end{aligned}$$

### A.1.1 Continuity Equation

We take the Reynolds average of the continuity equation

$$\begin{aligned} & \langle \partial_x u + \partial_y v + \partial_z w \rangle = \langle 0 \rangle && \text{(A.7)} \\ \Leftrightarrow \quad & \partial_x \langle u \rangle + \partial_y \langle v \rangle + \partial_z \langle w \rangle = 0 && \text{(A.8)} \end{aligned}$$

### A.1.2 Momentum Balances

1. Time-derivatives.
$$\langle \partial_t u_i \rangle = \partial_t \langle u_i \rangle, \quad \text{voor} \quad i = 1, 2, 3. \tag{A.9}$$

2. Body forces.
$$\begin{aligned} \langle f u_i \rangle &= f \langle u_i \rangle, \quad \text{voor} \quad i = x, y, && \text{(A.10)} \\ \left\langle \frac{\rho}{\rho_0} g \right\rangle &= \frac{g \langle \rho \rangle}{\rho_0}, && \text{(A.11)} \end{aligned}$$

3. Pressure gradients.
$$\left\langle \frac{1}{\rho_0} \partial_i p \right\rangle = \frac{1}{\rho_0} \partial_i \langle p \rangle, \quad \text{voor} \quad i = x, y, z. \tag{A.12}$$

4. Viscosity terms.

$$\langle \nu \partial_{ii} u_j \rangle = \nu \partial_{ii} \langle u_j \rangle, \quad \text{voor} \quad i = x, y, z. \tag{A.13}$$

5. We need a bit more attention when Reynolds-averaging the advection terms. First of all, using the continuity equation (**??**), we must rewrite the advection terms in their *conservative form* for $i = 1, 2, 3$:

$$\begin{aligned} u\partial_x u_i + v\partial_y u_i + w\partial_z u_i &= u\partial_x u_i + v\partial_y u_i + w\partial_z u_i + u_i \left(\partial_x u + \partial_y v + \partial_z w\right) && \text{(A.14)} \\ &= \partial_x(uu_i) + \partial_y(vu_i) + \partial_z(wu_i) && \text{(A.15)} \end{aligned}$$

We can average these term-by-term:

$$\begin{aligned} \langle \partial_j(u_i u_j) \rangle &= \langle \partial_j((\langle u_i \rangle + u_i')(\langle u_j \rangle + u_j')) \rangle && \text{(A.16)} \\ &= \langle \partial_j(\langle u_i \rangle \langle u_j \rangle) \rangle + \langle \partial_j(\langle u_i \rangle u_j') \rangle + \langle \partial_j(u_i' \langle u_j \rangle) \rangle + \langle \partial_j(u_i' u_j') \rangle && \text{(A.17)} \\ &= \partial_j(\langle u_i \rangle \langle \langle u_j \rangle \rangle) + \partial_j(\langle u_i \rangle \langle u_j' \rangle) + \partial_j(\langle u_i' \rangle \langle u_j \rangle) + \partial_j(\langle u_i' u_j' \rangle) && \text{(A.18)} \\ &= \partial_j(\langle u_i \rangle \langle u_j \rangle) + 0 + 0 + \partial_j(\langle u_i' u_j' \rangle) && \text{(A.19)} \\ &= \partial_j(\langle u_i \rangle \langle u_j \rangle) + \partial_j \langle u_i' u_j' \rangle. && \text{(A.20)} \end{aligned}$$

As is described in **??**, we parametrise the effect of the correlation terms $\partial_j \langle u_i' u_j' \rangle$ by means of the Boussinesq closeure hypothesis (Rozendaal (2019), p. 9):

$$\begin{aligned} &\langle u'u' \rangle = -2A_{\mathrm{h}} \partial_x \langle u \rangle, && \langle v'v' \rangle = -2A_{\mathrm{h}} \partial_y \langle v \rangle, && \langle w'w' \rangle = -2A_{\mathrm{v}} \partial_z \langle w \rangle, && \text{(A.21)} \\ &\langle u'v' \rangle = -A_{\mathrm{h}}(\partial_y \langle u \rangle + \partial_x \langle v \rangle), && \langle u'w' \rangle = -A_{\mathrm{v}} \partial_z \langle u \rangle - A_{\mathrm{h}} \partial_x \langle w \rangle, && \langle v'w' \rangle = -A_{\mathrm{v}} \partial_z \langle v \rangle - A_{\mathrm{h}} \partial_y \langle w \rangle. && \text{(A.22)} \end{aligned}$$

Substituting this parametrisation into the Reynoldsaveraging of (**??**) and applying the width-averaged continuity equation (A.8), leads to the following **Reynolds-averaged Navier-Stokes Equations**:

$$\begin{cases} \partial_x \langle u \rangle + \partial_y \langle v \rangle + \partial_z \langle w \rangle & = 0, \\ \partial_t \langle u \rangle + \partial_x \langle u \rangle^2 + \partial_y(\langle v \rangle \langle u \rangle) + \partial_z(\langle w \rangle \langle u \rangle) & = f\langle v \rangle - \frac{1}{\rho_0} \partial_x \langle p \rangle + \partial_x(\mathcal{A}_{\mathrm{h}} \partial_x \langle u \rangle) + \partial_y(\mathcal{A}_{\mathrm{h}} \partial_y \langle u \rangle) + \partial_z(\mathcal{A}_{\mathrm{v}} \partial_z \langle u \rangle), \\ \partial_t \langle v \rangle + \partial_x(\langle u \rangle \langle v \rangle) + \partial_y \langle v \rangle^2 + \partial_z(\langle w \rangle \langle v \rangle) & = -f\langle u \rangle - \frac{1}{\rho_0} \partial_y \langle p \rangle + \partial_x(\mathcal{A}_{\mathrm{h}} \partial_x \langle v \rangle) + \partial_y(\mathcal{A}_{\mathrm{h}} \partial_y \langle v \rangle) + \partial_z(\mathcal{A}_{\mathrm{v}} \partial_z \langle v \rangle), \\ \partial_t \langle w \rangle + \partial_x(\langle u \rangle \langle w \rangle) + \partial_y(\langle v \rangle \langle w \rangle) + \partial_z \langle w \rangle^2 & = -\frac{g\langle \rho \rangle}{\rho_0} - \frac{1}{\rho_0} \partial_z \langle p \rangle + \partial_x(\mathcal{A}_{\mathrm{h}} \partial_x \langle w \rangle) + \partial_y(\mathcal{A}_{\mathrm{h}} \partial_y \langle w \rangle) + \partial_z(\mathcal{A}_{\mathrm{v}} \partial_z \langle w \rangle), \end{cases} \tag{A.23}$$

where $\mathcal{A}_{\mathrm{h}} := A_{\mathrm{h}} + \nu$ en $\mathcal{A}_{\mathrm{v}} := A_{\mathrm{v}} + \nu$.

## A.2 Width-Averaging

### A.2.1 The Width-Averaging Operator's Properties

The width-averaging operator $\{\cdot\}$ is defined in the beginning of section 2.3. Similar to the Reynolds decomposition (A.1), we can define a width-averaging decomposition: $\alpha = \{\alpha\} + \alpha^*$, where $\alpha^* := \{\alpha\} - \alpha$ describe the fluctuations of $\alpha$ with respect to the width-averaged quantity. Again, these fluctuations satisfy

$$\{a^*\} = 0. \tag{A.24}$$

Applying Leipniz' Integral Rule (Rozendaal (2019), p. 14),

$$\left( \int_{B_1(x)}^{B_2(x)} \alpha(x, y, z, t) dy \right)_x = (B_2)_x \, \alpha|_{y=B_2} - (B_1)_x \, \alpha|_{y=B_1} + \int_{B_1(x)}^{B_2(x)} \alpha_x(x, y, z, t) dy, \tag{A.25}$$

the Fundamental Theorem of Calculus, and the product rule, we can prove that the following identities are true.

1. The width-average of a derivative w.r.t $x$.

$$\{\alpha_x\} = \frac{1}{\Delta} \left[ (\Delta\{\alpha\})_x + (B_1)_x \, \alpha|_{y=B_1} - (B_2)_x \, \alpha|_{y=B_2} \right] \tag{A.26}$$

2. The width-average of a derivative w.r.t $y$.

$$\{\alpha_y\} = \frac{1}{\Delta} \left[ (vu)|_{y=B_2} - (vu)|_{y=B_1} \right] \tag{A.27}$$

3. The width-average of a derivative w.r.t $z$.

$$\{\alpha_z\} = \{\alpha\}_z. \tag{A.28}$$

4. The width-average of a derivative w.r.t $t$.

$$\{\alpha_t\}_t = \{\alpha\}_t. \tag{A.29}$$

Since we assume that all lateral variations have a negligible influence on the width-averaged hydrodynamics in the vertical and longitudinal direction - as described in section 2.3 - we assume that the width-averaged lateral velocity component vanishes:

$$\{v\} = 0. \tag{A.30}$$

in line with this assumption, the influence of the lateral momentum balance vanishes as well. Therefore, the width-averaged model does not contain this lateral balance, and we will focus on the continuity equation and the longitudinal momentum balance from the Shallow Water Equations (2.7a).

### A.2.2 Width-Averaging of the Shallow Water Equations

**Continuity Equation**

Applying the above properties to the terms in the continuity equation in (2.7a) leads to the following expression:

$$\frac{1}{\Delta}\left(\Delta\{u\}\right)_x + \partial_z\{w\} = \frac{1}{\Delta}\left[\left(\partial_x B_1\ u|_{y=B_1} - \partial_y B_1\ v|_{y=B_1}\right) - \left(\partial_x B_2\ u|_{y=B_2} + \partial_y B_2\ v|_{y=B_2}\right)\right] \tag{A.31}$$

Making use of the boundary condition given in (2.12), it follows that the right-hand side of this equation vanishes, leading to the width-averaged continuity equation:

$$\frac{1}{\Delta}\left(\Delta\{u\}\right)_x + \{w\}_z = 0. \tag{A.32}$$

**Longitudinal Momentum Balance**

We will width-average the longitudinal momentum balance in (2.7a) term-by-term.

1. The time-derivative.

$$\{u_t\} = \{u\}_t. \tag{A.33}$$

2. The Coriolis term.

$$\{fv\} = f\{v\} = 0. \tag{A.34}$$

3. The advective terms. For $i = 1, 2, 3$, we can show that

$$\{u_i u\} = \{u_i\}\{u\} + \{u_i^* u^*\}. \tag{A.35}$$

Using this, it follows that

$$\{\left(u^2\right)_x\} = \frac{1}{\Delta}\left[\left(\Delta\{u\}^2\right)_x + \left(B_1\right)_x\ u^2\big|_{y=B_1} - \left(B_2\right)_x\ u^2\big|_{y=B_2} + \left(\Delta\{u^* u^*\}\right)_x\right], \tag{A.36}$$

$$\{(vu)_y\} = \frac{1}{\Delta}\left[(vu)|_{y=B_2} - B_1\ (vu)|_{y=B_1}\right], \tag{A.37}$$

$$\{(wu)_z\} = \left(\{w\}\{u\}\right)_z + \{w^* u^*\}_z. \tag{A.38}$$

Applying the impermeable wall condition (2.12) leads to the following sum of the width-averaged advection-terms.

$$\{\left(u^2\right)_x + (vu)_y + (wu)_z\} = \frac{1}{\Delta}\left[\left(\Delta\{u\}^2\right)_x + \underline{\left(\Delta\{u^* u^*\}\right)_x}\right] + \left(\{w\}\{u\}\right)_z + \underline{\{w^* u^*\}_z}. \tag{A.39}$$

4. The eddy-visosity terms. Similar to the advective terms, we can derive that

$$\{(\mathcal{A}_\mathrm{h} u_x)_x\} = \frac{1}{\Delta}\left(\{\mathcal{A}_\mathrm{h}\}\left(\Delta(x)\{u\}\right)_x\right)_x + \underbrace{\frac{1}{\Delta}\left(\{\mathcal{A}_\mathrm{h}\}\left[\left(B_1\right)_x\ u|_{y=B_1} - \left(B_2\right)_x\ u|_{y=B_2}\right]\right)_x} \tag{A.40}$$

$$+ \frac{1}{\Delta}\left[\underbrace{\left(B_1\right)_x\ \left(\mathcal{A}_\mathrm{h} u_x\right)|_{y=B_1} - \left(B_2\right)_x\ \left(\mathcal{A}_\mathrm{h} u_x\right)|_{y=B_2}} + \underline{\left(\Delta\{\mathcal{A}_\mathrm{h}^*(u_x)^*\}\right)_x}\right], \tag{A.41}$$

$$\{(\mathcal{A}_\mathrm{h} u_y)_y\} = \underbrace{\frac{1}{\Delta}\left[\left(\mathcal{A}_\mathrm{h} u_y\right)|_{y=B_2} - \left(\mathcal{A}_\mathrm{h} u_y\right)|_{y=B_1}\right]}, \tag{A.42}$$

$$\{(\mathcal{A}_\mathrm{v} u_z)_z\} = \partial_z(\{\mathcal{A}_\mathrm{v}\}\{u\}_z) + \underline{\{\mathcal{A}_\mathrm{v}^*(u_z)^*\}_z}. \tag{A.43}$$

5. The pressure gradient. First of all, we will consider the pressure gradient as it appears in the longitudinal momentum balance (2.4a).

$$\{p_x\} = \frac{1}{\Delta}\left[(\Delta\{p\})_x + (B_1)_x\, p|_{y=B_1} - (B_2)_x\, p|_{y=B_2}\right]. \tag{A.44}$$

Given the expression of the hydrostatic pressure (**??**), we find that

$$\{p\} = p_{\text{atm}} + g\left\{\int_z^{\zeta(x,y,t)} \rho(x,y,\hat{z},t)\, d\hat{z}\right\} \tag{A.45}$$

Now write $F(a) := \int_z^\zeta \rho\, d\hat{z}$. using this, we Taylor-expand around $a = \{\zeta\}$ and evaluate in $a = \zeta$:

$$\{F(\zeta)\} = \{F(\{\zeta\})\} + \left\{\zeta^* \partial_a\, F|_{a=\{\zeta\}}\right\} + \mathcal{O}\left((\zeta^*)^2\right). \tag{A.46}$$

Now define $R(x,z,t) := \left\{\zeta^* \partial_a\, F|_{a=\{\zeta\}}\right\} + \mathcal{O}\left((\zeta^*)^2\right)$. Using a variant of Leibniz'Integral Rule (A.25), we find the following expression for the width-averaged pressure term.

$$\left\{\frac{1}{\rho_0} p_x\right\} = \frac{1}{\rho_0 \Delta}\left[\Delta_x\left(p_{\text{atm}} + g\int_z^{\{\zeta\}} \{\rho\}\, d\hat{z}\right) + \underline{(\Delta R)_x} + \underwave{(B_1)_x\, p|_{y=B_1} - (B_2)_x\, p|_{y=B_2}}\right] \tag{A.47}$$

$$+ \frac{g\{\zeta\}_x\, \{\rho\}|_{z=\{\zeta\}}}{\rho_0} + \frac{g}{\rho_0}\left(\int_z^{\{\zeta\}(x,t)} \{\rho\}_x\, d\hat{z}\right) \tag{A.48}$$

### A.2.3 Simplification

The width-averaged expressions for the advective terms, the eddy-viscosity terms and the pressure gradient still contain terms concerning the lateral fluctuations and boundaries. Since these terms are difficult to determine, we will make the following assumptions in order to further simplify the expressions.

1. All boundary terms that are left have a negligible influence on the width-averaged hydrodynamics. These terms are indicated with a waving underline, and will be set to 0.
2. The influence of the terms that depend on the lateral variations is small, and can be modelled as an effective dissipation. Therefore, we define $\hat{\mathcal{A}}_{\text{h}}$ and $\hat{\mathcal{A}}_{\text{v}}$ as eddy viscosity terms that - in contrast to $\mathcal{A}_{\text{h}}$ and $\mathcal{A}_{\text{v}}$ - contain the dissipative influence of width-variations. The terms that are taken into these eddy-coefficients are given a straight underline.
3. We assume that the following term is negligible:

$$\frac{\Delta_x}{\Delta}\frac{\left(p_{\text{atm}} + g\int_z^{\{\zeta\}} \{\rho\}\, d\hat{z}\right)}{\rho_0}. \tag{A.49}$$

This leads to the following width-averaged longitudinal momentum balance.

$$\{u\}_t + \frac{1}{\Delta(x)}\left(\Delta(x)\{u\}^2\right)_x + (\{w\}\{u\})_z + g\{\zeta\}_x + \frac{g}{\rho_0}\int_z^{\{\zeta\}} \{\rho\}_x\, d\hat{z} = \left(\hat{\mathcal{A}}_{\text{h}}\{u\}_x\right)_x + \left(\hat{\mathcal{A}}_{\text{v}}\{u\}_z\right)_z. \tag{A.50}$$

Applying the product rule and the width-averaged coninuity equation, we find tits non-conservative form:

$$u_t + uu_x + wu_z + g\zeta_x + \frac{g}{\rho_0}\int_z^{\zeta} \rho_x\, d\hat{z} = \left(\hat{\mathcal{A}}_{\text{h}} u_x\right)_x + \left(\hat{\mathcal{A}}_{\text{v}} u_z\right)_z \tag{A.51}$$

### A.2.4 Width-Averaging of the Ice Floe Friction Term

We want to width-average the following term:

$$F_1 := \left(\eta_x^I\right)_x + \frac{1}{2}\left(\eta\left(u_y^I + v_x^I\right)\right)_y. \tag{A.52}$$

1. First, we focus on the second term, which is

$$\frac{1}{2}\left(\eta\left(u_y^I + v_x^I\right)\right)_y. \tag{A.53}$$

We width-average:

$$\left\{\frac{1}{2}\left(\eta\left(u_y^I + v_x^I\right)\right)_y\right\} = \frac{1}{2}\left\{\left(\eta\left(u_y^I + v_x^I\right)\right)_y\right\} \tag{A.54}$$

$$= \frac{1}{2\Delta}\left[B_2\left(\eta\left(u_y^I + v_x^I\right)\right)\Big|_{y=B_2} - B_1\left(\eta\left(u_y^I + v_x^I\right)\right)\Big|_{y=B_1}\right]. \tag{A.55}$$

2. Now, we look at the first term. For that, we write $\gamma := \eta u_x$, so that

$$\left(\eta u_x^I\right)_x = F\gamma_x. \tag{A.56}$$

We width-average:

$$\left\{\left(\eta u_x^I\right)_x\right\} = \{\gamma_x\} \tag{A.57}$$

$$= \frac{1}{\Delta}\left[\left(\Delta\{\gamma\}\right)_x + B_1'\,\gamma|_{y=B_1} - B_2'\,\gamma|_{y=B_2}\right]. \tag{A.58}$$

In here, we require an expression for $\{\gamma\}$, i.e.

$$\{\gamma\} = \{\eta u_x^I\} \tag{A.59}$$

$$= \{\eta\}\{u_x^I\} + \eta^*\{u_x^I\}. \tag{A.60}$$

Assuming that $\eta^*$, the width-variations of the horizontal ice-viscosity, is negigible compared to $\{\eta\}$, we proceed:

$$\{\gamma\} \approx \{\eta\}\{u_x^I\} \tag{A.61}$$

$$= \frac{\{\eta\}}{\Delta}\left[\left(\Delta\{u^I\}\right)_x + B_1'\,u^I\big|_{y=B_1} - B_2'\,u^I\big|_{y=B_2}\right]. \tag{A.62}$$

Therefore, the width-average of the first term is given by

$$\left\{\left(\eta u_x^I\right)_x\right\} = \frac{1}{\Delta}\left[\left(\Delta\{\gamma\}\right)_x + B_1'\,\gamma|_{y=B_1} - B_2'\,\gamma|_{y=B_2}\right] \tag{A.63}$$

$$= \frac{1}{\Delta}\left[\left(\frac{\Delta\{\eta\}}{\Delta}\left[\left(\Delta\{u^I\}\right)_x + B_1'\,u^I\big|_{y=B_1} - B_2'\,u^I\big|_{y=B_2}\right]\right)_x + B_1'\,\gamma|_{y=B_1} - B_2'\,\gamma|_{y=B_2}\right] \tag{A.64}$$

$$= \frac{1}{\Delta}\left[\left(\{\eta\}\left[\left(\Delta\{u^I\}\right)_x + B_1'\,u^I\big|_{y=B_1} - B_2'\,u^I\big|_{y=B_2}\right]\right)_x + B_1'\,\gamma|_{y=B_1} - B_2'\,\gamma|_{y=B_2}\right]. \tag{A.65}$$

As a first step for modelling ice floes, we assume that the influence of the boundary on the large-scale ice-dynamics is negligible. With this, we find that the width-average of the second term and many of the terms in the width-average of the first term vanish, leading to the following width-average of the ice floe longitudinal friction term:

$$\{F_1\} = \frac{1}{\Delta}\left(\{\eta\}\left(\Delta\left\{u^I\right\}\right)_x\right)_x \tag{A.66}$$

# Appendix B

# Description of the Numerical Model for Landfast Ice

The most general equation for the waterlevel is given by:

$$c_{FI}^2\,\hat{\zeta}^0_{xx} + \left(\left(c_{FI}^2\right)_x + \frac{\Delta_x}{\Delta}c_{FI}^2\right)\hat{\zeta}^0_x + \sigma^2\hat{\zeta}^0 = 0, \tag{B.1}$$

where

$$c_{FI}^2 := gH + \frac{g}{\beta}\left[\alpha_1\sinh(-\beta H) + \alpha_2\left(\cosh(-\beta H) - 1\right)\right]. \tag{B.2}$$

These coefficients can be $x$-dependent, which makes it very general. Furthermore, we have the following boundary conditions:

$$\begin{cases} \hat{\zeta}^0(0) &= A_{M_2}, \\ \hat{\zeta}^0_x(L) &= 0. \end{cases} \tag{B.3}$$

A finite-difference method is applied to discretisce this equation. The grid is defined by $x_j := \frac{j}{N}$ for $j = 0, 1, 2, ..., N$, and $h := \frac{L}{N}$.

For the inner grid points, central differences are applied, leading to the following equations:

$$c_{FI}^2\,\frac{\hat{\zeta}^{0,j+1} - 2\hat{\zeta}^{0,j} + \hat{\zeta}^{0,j-1}}{h^2} + \left(\left(c_{FI}^2\right)_x + \frac{\Delta_x}{\Delta}c_{FI}^2 - gH_x\,a_{FI}|_{z=-H}\right)\frac{\hat{\zeta}^{0,j+1} - \hat{\zeta}^{0,j-1}}{2h} + \sigma^2\hat{\zeta}^{0,j} = 0, \tag{B.4}$$

where $\hat{\zeta}^{0,j} := \hat{\zeta}^0(x_j)$.

If we accumulate this per term, we find:

$$B_{-1}\,\hat{\zeta}^{0,j-1} + B_0\,\hat{\zeta}^{0,j} + B_1\,\hat{\zeta}^{0,j+1} = 0, \quad \text{for} \quad j = 1, 2, ..., n-1, \tag{B.5}$$

where:

$$\begin{cases} B_{-1} &= \frac{c_{FI}^2}{h^2} - \frac{\left(c_{FI}^2\right)_x + \frac{\Delta_x}{\Delta}c_{FI}^2 - gH_x\,a_{FI}|_{z=-H}}{2h}, \\ B_0 &= \frac{-2c_{FI}^2}{h^2} + \sigma^2, \\ B_1 &= \frac{c_{FI}^2}{h^2} + \frac{\left(c_{FI}^2\right)_x + \frac{\Delta_x}{\Delta}c_{FI}^2 - gH_x\,a_{FI}|_{z=-H}}{2h}. \end{cases} \tag{B.6}$$

The Neumann boundary condition at the landward side is approximated by a second-order (i.e. $\mathcal{O}(h^2)$) left-sided approximation, given by

$$\frac{\hat{\zeta}^{0,N-2} - 4\hat{\zeta}^{0,N-1} + 3\hat{\zeta}^{0,N}}{2h} = 0. \tag{B.7}$$

The above discretisation leads to a linear system of the form

$$\underline{\mathbf{A}}_{\mathrm{L}}\,\mathbf{v}_{\mathrm{L}} = \mathbf{b}_{\mathrm{L}}, \tag{B.8}$$

where the L stands for Landfast. Here, we define

$$\mathbf{v}_{\mathrm{L}} = \begin{bmatrix} \hat{\zeta}^{0,0} \\ \hat{\zeta}^{0,1} \\ \vdots \\ \hat{\zeta}^{0,N-1} \\ \hat{\zeta}^{0,N} \end{bmatrix} \tag{B.9}$$

and

$$(\mathbf{b}_{\mathrm{L}})_k = \begin{cases} A_{M_2}, & \text{if} \quad k = 1, \\ 0, & \text{if} \quad k \neq 1, \end{cases} \tag{B.10}$$

and

$$\underline{\mathbf{A}}_{\mathrm{L}} = \begin{bmatrix} 1 & 0 & 0 & 0 & \cdots & 0 & 0 & 0 \\ B_{-1} & B_0 & B_1 & 0 & \cdots & 0 & 0 & 0 \\ 0 & B_{-1} & B_0 & B_1 & \cdots & 0 & 0 & 0 \\ \vdots & \vdots & \vdots & \vdots & \ddots & \vdots & \vdots & \vdots \\ 0 & 0 & 0 & 0 & \cdots & B_{-1} & B_0 & B_1 \\ 0 & 0 & 0 & 0 & \cdots & \frac{1}{2h} & -\frac{4}{2h} & \frac{3}{2h} \end{bmatrix} \tag{B.11}$$

# Appendix C

# Landfast Ice: Agreement of the Partial Cover Solution to the Full Ice Cover Solution for Constant Width

We can compare our partial-landfast-ice model, as given by the boundary condition (**??**), to the full-landfast-ice-cover model, as given by the boundary condition (2.18), in several ways: By setting $s_I = 0$, $x_I = L$ and $x_I = 0$, where the former two should lead to the situation without ice, and the latter to the situation with a full ice cover. We will apply all three to the solution given in (4.1) and compare it to the solution given in (**??**).

## C.1 The Limit $s_I \downarrow 0$

If $s_I = 0$, then the ice that has been introduced in our split model does not cause eny friction. Therefore, we expect that the solution this yields corresponds to the solution without ice (which follows from setting $s_I = 0$ in the boundary condition (2.18)). Note that, with our notation, taking $s_I = 0$ merely leads to $c_{FI}$ being equal to $c_F$, and thus

$$\hat{\zeta}^0 = a_1 \cos\left(\frac{\sigma(x - x_I)}{c_F}\right) + a_2 \sin\left(\frac{\sigma(x - x_I)}{c_F}\right), \tag{C.1}$$

with

$$a_1 = \frac{c_F A_{M_2} \cos\left(\frac{\sigma(L-x_I)}{c_F}\right)}{c_F \cos\left(-\frac{\sigma x_I}{c_F}\right)\cos\left(\frac{\sigma(L-x_I)}{c_F}\right) + c_F \sin\left(-\frac{\sigma x_I}{c_F}\right)\sin\left(\frac{\sigma(L-x_I)}{c_F}\right)}, \tag{C.2}$$

$$a_2 = \frac{c_F A_{M_2} \sin\left(\frac{\sigma(L-x_I)}{c_F}\right)}{c_F \cos\left(-\frac{\sigma x_I}{c_F}\right)\cos\left(\frac{\sigma(L-x_I)}{c_F}\right) + c_F \sin\left(-\frac{\sigma x_I}{c_F}\right)\sin\left(\frac{\sigma(L-x_I)}{c_F}\right)}, \tag{C.3}$$

which can be simplified to

$$a_1 = \frac{A_{M_2} \cos\left(\frac{\sigma(L-x_I)}{c_F}\right)}{\cos\left(-\frac{\sigma x_I}{c_F}\right)\cos\left(\frac{\sigma(L-x_I)}{c_F}\right) + \sin\left(-\frac{\sigma x_I}{c_F}\right)\sin\left(\frac{\sigma(L-x_I)}{c_F}\right)}, \tag{C.4}$$

$$a_2 = \frac{A_{M_2} \sin\left(\frac{\sigma(L-x_I)}{c_F}\right)}{\cos\left(-\frac{\sigma x_I}{c_F}\right)\cos\left(\frac{\sigma(L-x_I)}{c_F}\right) + \sin\left(-\frac{\sigma x_I}{c_F}\right)\sin\left(\frac{\sigma(L-x_I)}{c_F}\right)}. \tag{C.5}$$

Furthermore, we can rewrite the denominator of these two coefficients:

$$d_0 = \cos\left(-\frac{\sigma x_I}{c_F}\right)\cos\left(\frac{\sigma\,(L-x_I)}{c_F}\right) + \sin\left(-\frac{\sigma x_I}{c_F}\right)\sin\left(\frac{\sigma\,(L-x_I)}{c_F}\right) \tag{C.6}$$

$$= \frac{1}{2}\cos\left(\frac{\sigma\,(L-2x_I)}{c_F}\right) + \frac{1}{2}\cos\left(\frac{\sigma L}{c_F}\right) + \frac{1}{2}\cos\left(\frac{\sigma L}{c_F}\right) - \frac{1}{2}\cos\left(\frac{\sigma\,(L-2x_I)}{c_F}\right) \tag{C.7}$$

$$= \cos\left(\frac{\sigma L}{c_F}\right). \tag{C.8}$$

This allows us to further rewrite our expression:

$$\hat{\zeta}^0 = \frac{A_{M_2}}{\cos\left(\frac{\sigma L}{c_F}\right)}\left[\cos\left(\frac{\sigma\,(L-x_I)}{c_F}\right)\cos\left(\frac{\sigma(x-x_I)}{c_F}\right) + \sin\left(\frac{\sigma\,(L-x_I)}{c_F}\right)\sin\left(\frac{\sigma(x-x_I)}{c_F}\right)\right] \tag{C.9}$$

$$= \frac{A_{M_2}}{\cos\left(\frac{\sigma L}{c_F}\right)}\cos\left(\frac{\sigma\,(L-x)}{c_F}\right) \tag{C.10}$$

$$\hat{\zeta}^0 = \frac{A_{M_2}\cos\left(\frac{\sigma(L-x)}{c_F}\right)}{\cos\left(\frac{\sigma L}{c_F}\right)}, \tag{C.11}$$

which agrees with (**??**) if we set $c_{FI} = c_F$. A plot for the agreement of the two solutions can be seen in Figure C.1.

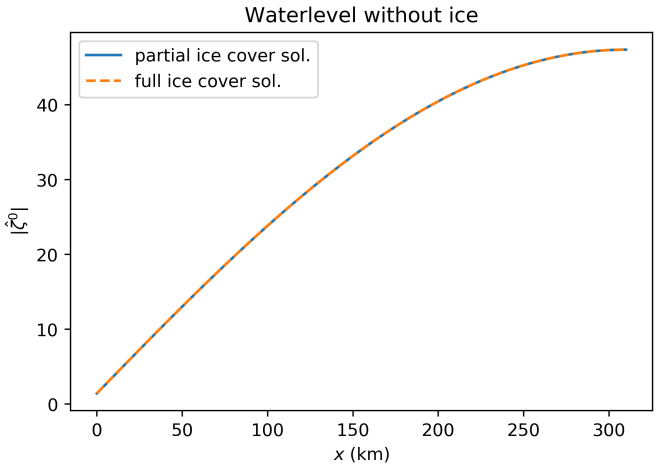


Figure C.1: An example of the agreement of the waterlevel for $s_I = 0$.

## C.2 The Limit $x_I \uparrow L$

If $x_I = L$, we expect that the solution to our partial-ice model agrees with our no-ice model. Let us fill in $x_I = L$.

$$\hat{\zeta}^0 = \begin{cases} a_1\cos\left(\frac{\sigma(x-L)}{c_F}\right) + a_2\sin\left(\frac{\sigma(x-L)}{c_F}\right), & \text{if } 0 < x < L, \\ a_1\cos\left(\frac{\sigma(x-L)}{c_{FI}}\right) + \frac{c_{FI}}{c_F}a_2\sin\left(\frac{\sigma(x-L)}{c_{FI}}\right), & \text{if } L < x < L. \end{cases} \tag{C.12}$$

$$= a_1\cos\left(\frac{\sigma(x-L)}{c_F}\right) + a_2\sin\left(\frac{\sigma(x-L)}{c_F}\right). \tag{C.13}$$

We also substitute $x_I = L$ into the coefficients.

$$a_1 = \frac{c_{FI}A_{M_2}\cos\left(\frac{\sigma(L-L)}{c_{FI}}\right)}{c_{FI}\cos\left(-\frac{\sigma L}{c_F}\right)\cos\left(\frac{\sigma(L-L)}{c_{FI}}\right) + c_F\sin\left(-\frac{\sigma L}{c_F}\right)\sin\left(\frac{\sigma(L-L)}{c_{FI}}\right)} \tag{C.14}$$

$$= \frac{c_{FI}A_{M_2}}{c_{FI}\cos\left(-\frac{\sigma L}{c_F}\right)} \tag{C.15}$$

$$= \frac{A_{M_2}}{\cos\left(-\frac{\sigma L}{c_F}\right)}. \tag{C.16}$$

and

$$a_2 = \frac{c_F A_{M_2} \sin\left(\frac{\sigma(L-L)}{c_{FI}}\right)}{c_{FI}\cos\left(-\frac{\sigma L}{c_F}\right)\cos\left(\frac{\sigma(L-L)}{c_{FI}}\right) + c_F \sin\left(-\frac{\sigma L}{c_F}\right)\sin\left(\frac{\sigma(L-L)}{c_{FI}}\right)} \tag{C.17}$$

$$= 0 \tag{C.18}$$

Thus now,

$$\hat{\zeta}^0 = \frac{A_{M_2}\cos\left(\frac{\sigma(x-L)}{c_F}\right)}{\cos\left(-\frac{\sigma L}{c_F}\right)}. \tag{C.19}$$

As we saw before, this again is what we expect to happen. See Figure C.2 for a visual representation of the agreement.

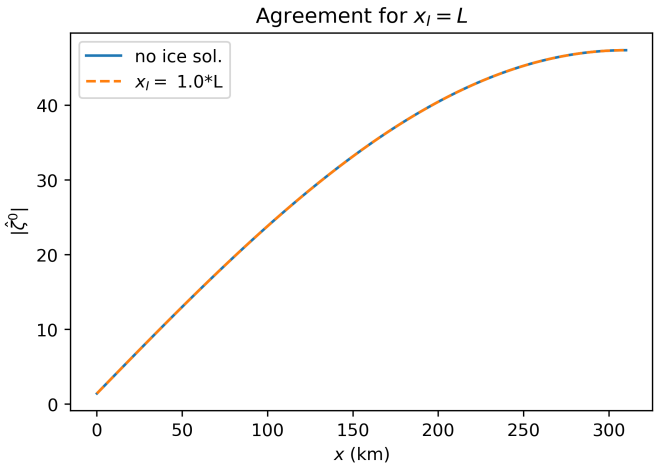


Figure C.2: An example of the agreement of the waterlevel for $x_I = L$.

## C.3 The limit $x_I \downarrow 0$

If $x_I = 0$, we expect that the solution to our partial-ice model agrees with our full-ice model. Let us fill in $x_I = 0$.

$$\hat{\zeta}^0 = \begin{cases} a_1\cos\left(\frac{\sigma x}{c_F}\right) + a_2\sin\left(\frac{\sigma x}{c_F}\right), & \text{if } 0 < x < 0, \\ a_1\cos\left(\frac{\sigma x}{c_{FI}}\right) + \frac{c_{FI}}{c_F}a_2\sin\left(\frac{\sigma x}{c_{FI}}\right), & \text{if } 0 < x < L. \end{cases} \tag{C.20}$$

$$= a_1\cos\left(\frac{\sigma x}{c_{FI}}\right) + \frac{c_{FI}}{c_F}a_2\sin\left(\frac{\sigma x}{c_{FI}}\right) \tag{C.21}$$

We also substitute $x_I = 0$ into the coefficients.

$$a_1 = \frac{c_{FI}A_{M_2}\cos\left(\frac{\sigma L}{c_{FI}}\right)}{c_{FI}\cos(0)\cos\left(\frac{\sigma L}{c_{FI}}\right) + c_F\sin(0)\sin\left(\frac{\sigma L}{c_{FI}}\right)} \tag{C.22}$$

$$= \frac{c_{FI}A_{M_2}\cos\left(\frac{\sigma L}{c_{FI}}\right)}{c_{FI}\cos\left(\frac{\sigma L}{c_{FI}}\right)} \tag{C.23}$$

$$= \frac{A_{M_2}\cos\left(\frac{\sigma L}{c_{FI}}\right)}{\cos\left(\frac{\sigma L}{c_{FI}}\right)}. \tag{C.24}$$

$$a_2 = \frac{c_F A_{M_2} \sin\left(\frac{\sigma L}{c_{FI}}\right)}{c_{FI}\cos(0)\cos\left(\frac{\sigma L}{c_{FI}}\right) + c_{FI}\sin(0)\sin\left(\frac{\sigma L}{c_{FI}}\right)} \tag{C.25}$$

$$= \frac{c_F A_{M_2} \sin\left(\frac{\sigma L}{c_{FI}}\right)}{c_{FI}\cos\left(\frac{\sigma L}{c_{FI}}\right)} \tag{C.26}$$

$$= \frac{c_F}{c_{FI}} \frac{A_{M_2} \sin\left(\frac{\sigma L}{c_{FI}}\right)}{\cos\left(\frac{\sigma L}{c_{FI}}\right)} \tag{C.27}$$

We fill this in in our solution.

$$\hat{\zeta}^0 = \frac{A_{M_2}\cos\left(\frac{\sigma L}{c_{FI}}\right)}{\cos\left(\frac{\sigma L}{c_{FI}}\right)}\cos\left(\frac{\sigma x}{c_{FI}}\right) + \frac{c_{FI}}{c_F}\frac{c_F}{c_{FI}}\frac{A_{M_2}\sin\left(\frac{\sigma L}{c_{FI}}\right)}{\cos\left(\frac{\sigma L}{c_{FI}}\right)}\sin\left(\frac{\sigma x}{c_{FI}}\right) \tag{C.28}$$

$$= \frac{A_{M_2}}{c_F\cos\left(\frac{\sigma L}{c_{FI}}\right)}\left[\cos\left(\frac{\sigma L}{c_{FI}}\right)\cos\left(\frac{\sigma x}{c_{FI}}\right) + \sin\left(\frac{\sigma L}{c_{FI}}\right)\sin\left(\frac{\sigma x}{c_{FI}}\right)\right] \tag{C.29}$$

$$\hat{\zeta}^0 = \frac{A_{M_2}\cos\left(\frac{\sigma(x-L)}{c_{FI}}\right)}{\cos\left(\frac{\sigma L}{c_{FI}}\right)}. \tag{C.30}$$

This is as expected. See Figure C.3 for a visualisation.

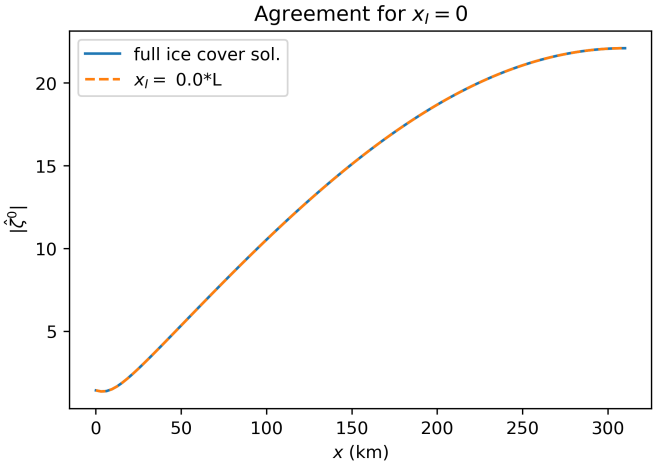


Figure C.3: An example of the agreement of the waterlevel for $x_I = 0$.

# Appendix D

# The Linear System for the Numerical Ice Floe Model

The method described in Section 4.2 leads to the following discretisiations of the longitudinal momentum balances and the continuity equation. In our computations, we set the horizontal eddy viscosity $\hat{\mathcal{A}}_{\mathrm{v}}$ to 0, since it is negligible in the momentum balance (see section 3.2)

1. The longitudinal momentum balance; for $m = 1, ..., N_a$:

$$\left(i\sigma + \hat{\mathcal{A}}_{\mathrm{v}}\lambda_m\right) a_m(x)\langle\phi_m, \phi_m\rangle + \hat{\mathcal{A}}_{\mathrm{h}} a_m''(x)\langle\phi_m, \phi_m\rangle + g\langle 1, \phi_m\rangle\, \hat{\zeta}_x^0 \tag{D.1}$$

$$-\sum_{n=1}^{N_a}\left[\left(\eta_x\Delta_x + \eta\Delta_{xx}\right) a_n(x) + \left(\eta_x\Delta + 2\eta\Delta_x\right) a_n'(x) + \eta\Delta a_n''(x)\right]\frac{\langle F\phi_n, \phi_m\rangle}{\Delta} = 0, \tag{D.2}$$

2. The continuity equation:

$$\sum_{n=1}^{N_a}\left[\langle 1, \phi_n(z)\rangle\left(\frac{a_n^{j+1} - a_n^j}{h}\right)\right] + i\sigma\hat{\zeta}^{0,j} = 0. \tag{D.3}$$

Furthermore, we have the following boundary conditions. For $m = 1, .., N_a$,

$$\frac{a_n^1 - a_n^0}{h} = 0, \tag{D.4}$$

$$a_m^{N_a} = 0, \tag{D.5}$$

and

$$\hat{\zeta}^{0,0} = A_{M_2}, \tag{D.6}$$

$$\frac{\hat{\zeta}^{0,N_a} - \hat{\zeta}^{0,N_a-1}}{h} = 0. \tag{D.7}$$

The above discretisation leads to a linear system of the form

$$\underline{\mathbf{A}}_{\mathrm{F}}\mathbf{v}_{\mathrm{F}} = \mathbf{b}_{\mathrm{F}}, \tag{D.8}$$

where the F stands for Floes. Here, we have used the following definitions

$$\mathbf{v}_{\text{floes}} = \begin{bmatrix} \mathbf{a}_0 \\ \mathbf{a}_1 \\ \vdots \\ \mathbf{a}_K \\ \hat{\boldsymbol{\zeta}}^0 \end{bmatrix} = \begin{bmatrix} a_0^0 \\ \vdots \\ a_0^N \\ a_1^0 \\ \vdots \\ a_1^N \\ \vdots \\ a_K^0 \\ \vdots \\ a_K^N \\ \hat{\zeta}^{0,0} \\ \vdots \\ \hat{\zeta}^{,N} \end{bmatrix} \tag{D.9}$$

and

$$(\mathbf{b}_{\text{floes}})_k = \begin{cases} 0, & \text{if} \quad k \neq 1 + K(N+1), \\ A_{M_2}, & \text{if} \quad k = 1 + K(N+1). \end{cases} \tag{D.10}$$

The matrix is defined as follows.

$$\underline{\mathbf{A}}_{\text{F}} = \begin{bmatrix} \underline{\mathbf{A}}^a_{1,1} & \underline{\mathbf{A}}^a_{1,2} & \underline{\mathbf{A}}^a_{1,3} & \cdots & \underline{\mathbf{A}}^a_{1,N_a} & \underline{\mathbf{A}}^{\hat{\zeta}^0}_1 \\ \underline{\mathbf{A}}^a_{2,1} & \underline{\mathbf{A}}^a_{2,2} & \underline{\mathbf{A}}^a_{2,3} & \cdots & \underline{\mathbf{A}}^a_{2,N_a} & \underline{\mathbf{A}}^{\hat{\zeta}^0}_2 \\ \underline{\mathbf{A}}^a_{3,1} & \underline{\mathbf{A}}^a_{3,2} & \underline{\mathbf{A}}^a_{3,3} & \cdots & \underline{\mathbf{A}}^a_{3,N_a} & \underline{\mathbf{A}}^{\hat{\zeta}^0}_3 \\ \vdots & \vdots & \vdots & \ddots & \vdots & \vdots \\ \underline{\mathbf{A}}^a_{N_a,1} & \underline{\mathbf{A}}^a_{N_a,2} & \underline{\mathbf{A}}^a_{N_a,3} & \cdots & \underline{\mathbf{A}}^a_{N_a,N_a} & \underline{\mathbf{A}}^{\hat{\zeta}^0}_{N_a} \\ \underline{\mathbf{B}}^a_1 & \underline{\mathbf{B}}^a_2 & \underline{\mathbf{B}}^a_3 & \cdots & \underline{\mathbf{B}}^a_{N_a} & \underline{\mathbf{B}}^{\hat{\zeta}^0} \end{bmatrix}, \tag{D.11}$$

and is built from sub-matrices, which are given below.

1. The interaction of $a_m$ with itself, for $m = 1, ..., N_a$.

$$\underline{\mathbf{A}}^a_{m,m} = \begin{bmatrix} -\frac{1}{h} & \frac{1}{h} & 0 & 0 & \cdots & 0 & 0 & 0 \\ \tilde{D}^{-1}_m & \tilde{D}^0_m & \tilde{D}^1_m & 0 & \cdots & 0 & 0 & 0 \\ 0 & \tilde{D}^{-1}_m & \tilde{D}^0_m & \tilde{D}^1_m & \cdots & 0 & 0 & 0 \\ \vdots & \vdots & \vdots & \ddots & \vdots & \vdots & \vdots & \\ 0 & 0 & 0 & 0 & \cdots & \tilde{D}^{-1}_m & \tilde{D}^0_m & \tilde{D}^1_m \\ 0 & 0 & 0 & 0 & \cdots & 0 & 0 & 1 \end{bmatrix} \tag{D.12}$$

$$+ \begin{bmatrix} 0 & 0 & 0 & 0 & \cdots & 0 & 0 & 0 \\ D^{-1}_{m,m}(x_1) & D^0_{m,m}(x_1) & D^1_{m,m}(x_1) & 0 & \cdots & 0 & 0 & 0 \\ 0 & D^{-1}_{m,m}(x_2) & D^0_{m,m}(x_2) & D^1_{m,m}(x_2) & \cdots & 0 & 0 & 0 \\ \vdots & \vdots & \vdots & \ddots & \vdots & \vdots & \vdots & \\ 0 & 0 & 0 & 0 & \cdots & D^{-1}_{m,m}(x_{N_x-1}) & D^0_{m,m}(x_{N_x-1}) & D^1_{m,m}(x_{N_x-1}) \\ 0 & 0 & 0 & 0 & \cdots & 0 & 0 & 0 \end{bmatrix} \tag{D.13}$$

2. The interaction of $a_m$ with $a_n$, where $m \neq n$, for $n, m = 1, ..., N_a$.

$$\underline{\mathbf{A}}^{a}_{m,n} = \begin{bmatrix} 0 & 0 & 0 & 0 & \cdots & 0 & 0 & 0 \\ D_1^{-1}(x_1) & D^0_{m,n}(x_1) & D^1_{m,n}(x_1) & 0 & \cdots & 0 & 0 & 0 \\ 0 & D_1^{-1}(x_2) & D^0_{m,n}(x_2) & D^1_{m,n}(x_2) & \cdots & 0 & 0 & 0 \\ \vdots & \vdots & \vdots & \ddots & \vdots & \vdots & \vdots & \\ 0 & 0 & 0 & 0 & \cdots & D^{-1}_{m,n}(x_{N_x-1}) & D^0_{m,n}(x_{N_x-1}) & D^1_{m,n}(x_{N_x-1}) \\ 0 & 0 & 0 & 0 & \cdots & 0 & 0 & 0 \end{bmatrix} \tag{D.14}$$

3. The interaction with $\hat{\zeta}^0$, for $m = 1, ..., N_a$.

$$\underline{\mathbf{A}}^{\hat{\zeta}^0}_{m} = \begin{bmatrix} 0 & 0 & 0 & 0 & \cdots & 0 & 0 & 0 \\ E_m^{-1} & 0 & E_m^1 & 0 & \cdots & 0 & 0 & 0 \\ 0 & E_m^{-1} & 0 & E_m^1 & \cdots & 0 & 0 & 0 \\ \vdots & \vdots & \vdots & \vdots & \ddots & \vdots & \vdots & \vdots \\ 0 & 0 & 0 & 0 & \cdots & E_m^{-1} & 0 & E_m^1 \\ 0 & 0 & 0 & 0 & \cdots & 0 & 0 & 0 \end{bmatrix} \tag{D.15}$$

**Continuity**

1. The terms in the sum, for $n = 1, ..., N_a$.

$$\underline{\mathbf{B}}^{a}_{n} = \begin{bmatrix} 0 & 0 & 0 & 0 & \cdots & 0 & 0 & 0 \\ 0 & C_n^0 & C_n^1 & 0 & \cdots & 0 & 0 & 0 \\ 0 & 0 & C_n^0 & C_n^1 & \cdots & 0 & 0 & 0 \\ \vdots & \vdots & \vdots & \vdots & \ddots & \vdots & \vdots & \vdots \\ 0 & 0 & 0 & 0 & \cdots & 0 & C_n^0 & C_n^1 \\ 0 & 0 & 0 & 0 & \cdots & 0 & 0 & 0 \end{bmatrix} \tag{D.16}$$

2. The part with $\hat{\zeta}^0$.

$$\underline{\mathbf{B}}^{\hat{\zeta}^0} = \begin{bmatrix} 1 & 0 & 0 & 0 & \cdots & 0 & 0 & 0 \\ 0 & i\sigma & 0 & 0 & \cdots & 0 & 0 & 0 \\ 0 & 0 & i\sigma & 0 & \cdots & 0 & 0 & 0 \\ \vdots & \vdots & \vdots & \vdots & \ddots & \vdots & \vdots & \vdots \\ 0 & 0 & 0 & 0 & \cdots & 0 & i\sigma & 0 \\ 0 & 0 & 0 & 0 & \cdots & 0 & 0 & i\sigma \end{bmatrix} \tag{D.17}$$

**Notation**

Above, we used the following definitions:

$$C_n^0 = -\frac{\langle 1, \phi_n \rangle}{h} + \frac{\Delta_x \langle 1, \phi_n \rangle}{\Delta}, \tag{D.18}$$

$$C_n^1 = \frac{\langle 1, \phi_n \rangle}{h}, \tag{D.19}$$

and

$$\tilde{D}_m^{-1} = \frac{\hat{\mathcal{A}}_{\mathrm{h}}\langle\phi_m,\phi_m\rangle}{h^2} \tag{D.20}$$

$$\tilde{D}_m^{0} = \left(i\sigma + \hat{\mathcal{A}}_{\mathrm{v}}\lambda_m\right)\langle\phi_m,\phi_m\rangle + \frac{-2\hat{\mathcal{A}}_{\mathrm{h}}\langle\phi_m,\phi_m\rangle}{h^2}, \tag{D.21}$$

$$\tilde{D}_m^{1} = \frac{\hat{\mathcal{A}}_{\mathrm{h}}\langle\phi_m,\phi_m\rangle}{h^2} \tag{D.22}$$

$$D_{m,n}^{-1}(x_j) = -\left[\frac{\eta(x_j)\Delta(x_j)}{h^2}\right]\frac{\langle F\phi_n,\phi_m\rangle}{\Delta(x_j)}, \tag{D.23}$$

$$D_{m,n}^{0}(x_j) = -\left[\eta_x(x_j)\Delta_x(x_j) + \eta(x_j)\Delta_{xx}(x_j) - \frac{\eta_x(x_j)\Delta(x_j) + 2\eta(x_j)\Delta_x(x_j)}{h} + \frac{-2\eta(x_j)\Delta(x_j)}{h^2}\right]\frac{\langle F\phi_n,\phi_m\rangle}{\Delta(x_j)}, \tag{D.24}$$

$$D_{m,n}^{1}(x_j) = -\left[\frac{\eta_x(x_j)\Delta(x_j) + 2\eta(x_j)\Delta_x(x_j)}{h} + \frac{\eta(x_j)\Delta(x_j)}{h^2}\right]\frac{\langle F\phi_n,\phi_m\rangle}{\Delta(x_j)}. \tag{D.25}$$

and

$$E_m^{-1} = -\frac{g\langle 1,\phi_m\rangle}{2h}, \tag{D.26}$$

$$E_m^{1} = \frac{g\langle 1,\phi_m\rangle}{2h}. \tag{D.27}$$

# Appendix E

# Error Analysis for the Numerical Ice Floe Model

In this Appendix, the error made in approximating the leading order waterlevel and longitudinal water velocity without ice is analysed. This is done by setting $F \equiv 0$, so that the influence of ice floes' viscosity is negligible. Since $\hat{\mathcal{A}}_{\mathrm{h}}$ lead to a negligible contribution as well, we set it to 0. The approximated solutions should converge to the analytical solution without ice given in section 4.1, if one is far enough away from the seaward boundary.

## E.1 Examples of Approximations

For $N_x = 400$ and several values of $N_a$, the approximations of the depth-profile of the leading order longitudinal water velocity and waterlevel are shown in Figure E.1, along with the analytical solution.

## E.2 Error Computation

Let $\hat{\boldsymbol{\zeta}}^0_{(N_x,N_a)} = [\hat{\zeta}^{0,0}, ..., \hat{\zeta}^{0,N_x}]$ and $\hat{\mathbf{u}}^{0,j}_{(N_x,N_a)} = [\hat{u}^{0,j}(z), ..., \hat{u}^{0,j}(z)]$ be approximations for the leading order waterlevel and longitudinal water velocity without ice, where $\hat{u}^{0,j}(z)$ approximates $\hat{u}^0(z, x_j)$ and $\hat{\zeta}^{0,0}$ approximates $\hat{\zeta}^0(x_j)$. To assess the accuracy of our numerical solution, we compute the maximal relative errors: for the waterlevel, by maximising the relative error over the length of the estuary, and for the water velocity, by choosing a grid point $x_j$ and maximising over the depth. This will give insight in the convergence behaviour and accuracy of the solution for different combinations of $N_a$ and $N_x$. We describe the definition of these relative errors and the maximisation procedure below.

1. For the waterlevel, for each grid-point $x_j$, we compute the relative error as follows:

$$E^{\zeta}_j = \left| \frac{\hat{\zeta}^0(x_j) - \hat{\zeta}^{0,j}}{\hat{\zeta}^0(x_j)} \right|. \tag{E.1}$$

   For the waterlevel, we define the *maximal relative longitudinal error* by taking the maximum over all grid-points:

$$E^{\zeta} = \max\left\{ E^{\zeta}_j : \quad j = 0, ..., N_x \right\}. \tag{E.2}$$

2. For the longitudinal water velocity, we will compute the *maximal relative vertical error*, which is defined per grid point $x_j$. Specifically, we will not consider the relative error in $\hat{u}^0$ itself, but in $\hat{u}^0/\hat{\zeta}^0_x$. This relative error at point $x_j$ and depth $z$ is defined as

$$E^u_j(z) = \left| \frac{\frac{\hat{u}^0(x_j,z)}{\hat{\zeta}^0_x(x_j)} - \frac{\hat{u}^{0,j}(z)}{\hat{\zeta}^{0,j}_x}}{\frac{\hat{u}^0(x_j,z)}{\hat{\zeta}^{0,j}_x}} \right|. \tag{E.3}$$

   The approximation of the waterlevel's gradient is done by a central difference, i.e.

$$\hat{\zeta}^{0,j}_x := \frac{\hat{\zeta}^{0,j+1} - \hat{\zeta}^{0,j-1}}{2h}. \tag{E.4}$$

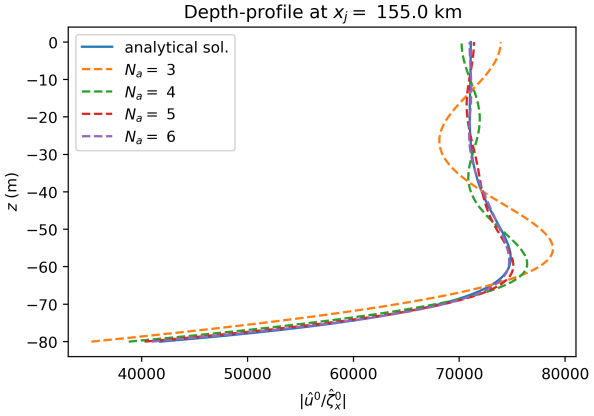


(a) The longitudinal water velocity's depth-profile at $x = L/2$.

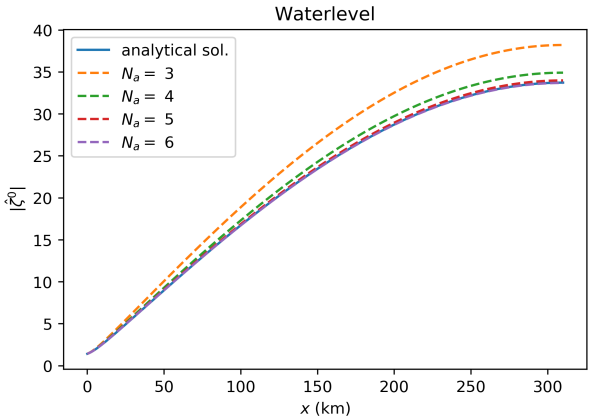


(b) The waterlevel for a constant width.

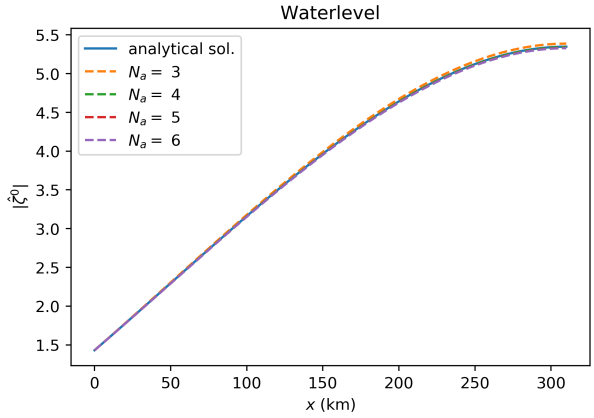


(c) The waterlevel for an exponentially converging width with convergence length $1/L_b = 1/L$.

Figure E.1: A number of approximations for $N_x = 400$ compared to the analytical solution without ice.

The maximal error is computed by maximising over $z$, i.e.

$$E_j^u = \max\left\{E_j^u(z): \quad z \in [-H, 0]\right\}. \tag{E.5}$$

Furthermore, we will compute the relative errors for all grid points. Doing this will give insight in whether there are places in along the length of the estuary where the error remains particularly large.

1. For the water velocity, we will simply compute the relative error defined in equation (E.1) for $j = 1, ..., N_x$. This leads to the following array of errors:

$$\mathbf{E}^\zeta = \left[E_0^\zeta, ..., E_{N_x}^\zeta\right]. \tag{E.6}$$

2. For the longitudinal water velocity, we will choose a value of $z$ and compute the relative error at each grid point $x_j$. Thus, the array of errors that we compute is defined as follows:

$$\mathbf{E}^u(z) = \left[\left|\frac{\hat{u}^{0,0}(z) - \hat{u}^0(x_0, z)}{\hat{u}^{0,0}(z)}\right|, ..., \left|\frac{\hat{u}^{0,N_x}(z) - \hat{u}^0(x_{N_x}, z)}{\hat{u}^{0,N_x}(z)}\right|\right]. \tag{E.7}$$

We expect that this error will not necessarily converge to 0 around $x = 0$, since the boundary condition stating that $\hat{u}_x = 0$ does not apply to the analytical solution given in (4.2).

### Error Plots

Using the numerical method described above, for a number of values of $N_a$, the relative errors in approximating $\hat{\zeta}^0$ and $\hat{u}^0$ are computed as a function of $h = L/N_x$. The results are shown in Figures E.2, E.3, E.4, E.5.

In Figure E.2, the maximal relative longitudinal error for the leading order waterlevel as given in (E.2) is shown. By comparing the subfigures corresponding to different values of $N_a$, it becomes clear that the maximal relative errors for the waterlevel decrease for increasing $N_a$. It is notable that for $N_a = 3$ and $N_a = 4$, taking a finer grid for the longitudinal axis does not necessarily improve the accuracy of the approximation. However, for $N_a = 5$ and $N_a = 6$, decreasing the mesh does lead to a decreasing error. However, the errors do not follow a linear trend in $h$, which might be related to $N_a$ or the size of $h$.

Figure E.3 shows the maximal relative vertical error for the leading order longitudinal water velocity as given by (E.5). It can be seen that - as expected - this error is independent of the mesh-size.

In Figure E.4, the relative error for the leading order waterlevel (E.6) as a function of $x$ is shown. The error gnerally shows a decreasing trend for a decreasing mesh-size. However, the error near $x = 0$ does not decrease for increasing $N_a$, which is likely caused by the boundary condition at $x = 0$, which does not apply to our analytical solution. Furthermore, by comparing the subfigures, one sees that the approximations for $N_a = 5$ and $N_a = 6$ are more accurate than those for $N_a = 3$ and $N_a = 4$. For the larger values of $N_a$, we see again that the error is larger near $x = 0$.

Figure E.5 shows the relative error for the leading order water velocity (E.7) as a function of $x$. As Figure E.2 showed for the leading order waterlevel, for $N_a = 3$ and $N_a = 4$, the relative error is not necessarily decreasing for a decreasing mesh-size, and the same is seen when $N_a = 5$, but for $N_a = 6$, the error does decrease as $h$ decreases. Furthermore, for $N_a = 6$, the error tends to be larger near $x = 0$, which can be explained in a similar way as for the leading order waterlevel.

Overall, we see that the approximations found with $N_a = 5$ and $N_a = 6$ yield relative errors that are smaller than 0.05 when $N_x = 200$ and $N_x = 400$, if one ignores the approximations for $x < 30$ km.

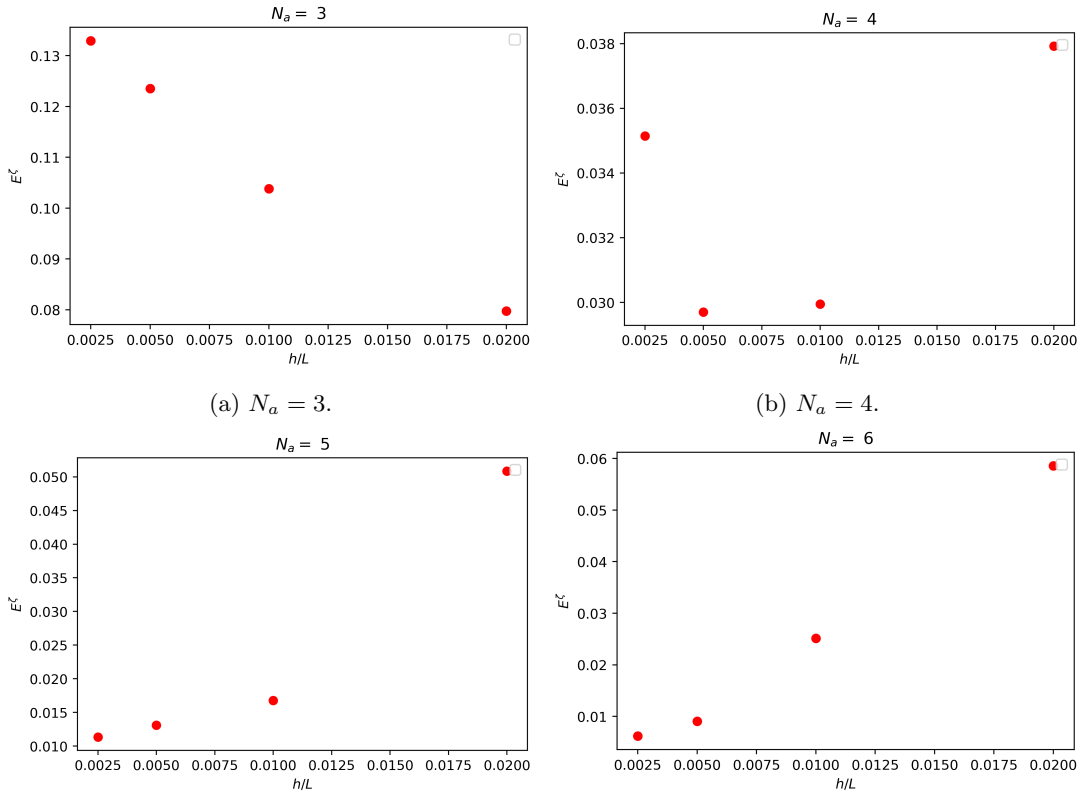


(a) $N_a = 3$.

(b) $N_a = 4$.

(c) $N_a = 5$.

(d) $N_a = 6$.

Figure E.2: The maximal relative error for the waterlevel as a function of the mesh-size.

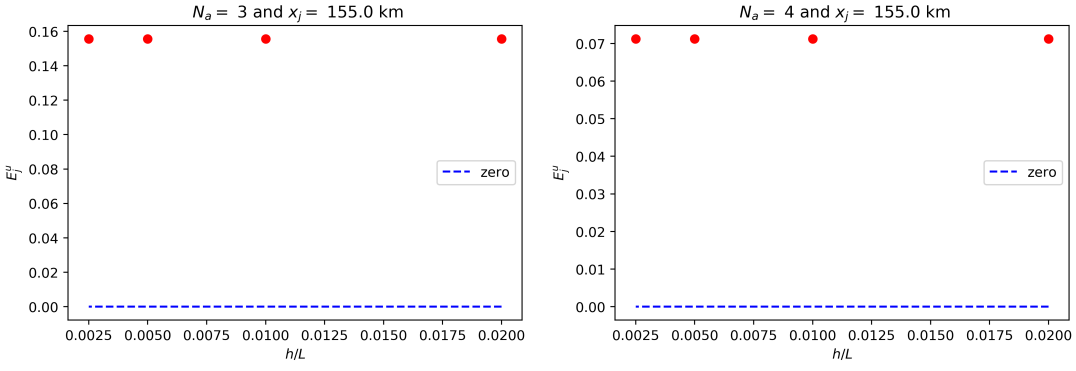


(a) $N_a = 3$. (b) $N_a = 4$.

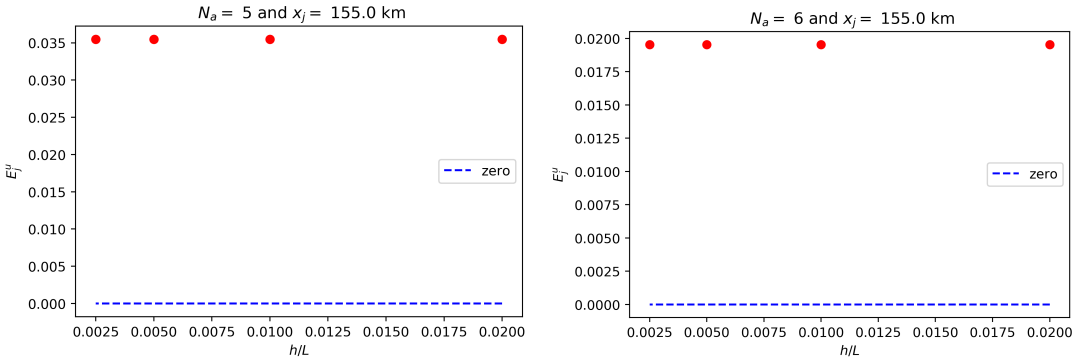


(c) $N_a = 5$. (d) $N_a = 6$.

Figure E.3: The maximal relative error for the longitudinal water velocity's depth-profile at $x = L/2$ as a function of the mesh-size.

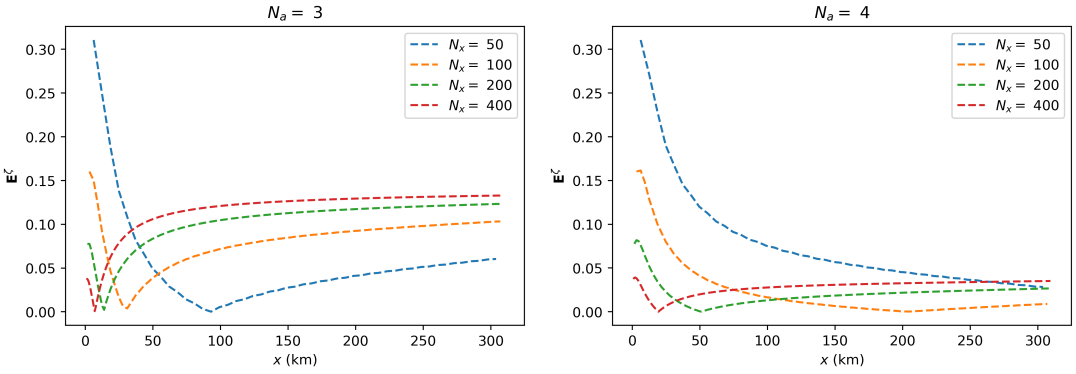


(a) $N_a = 3$. (b) $N_a = 4$.

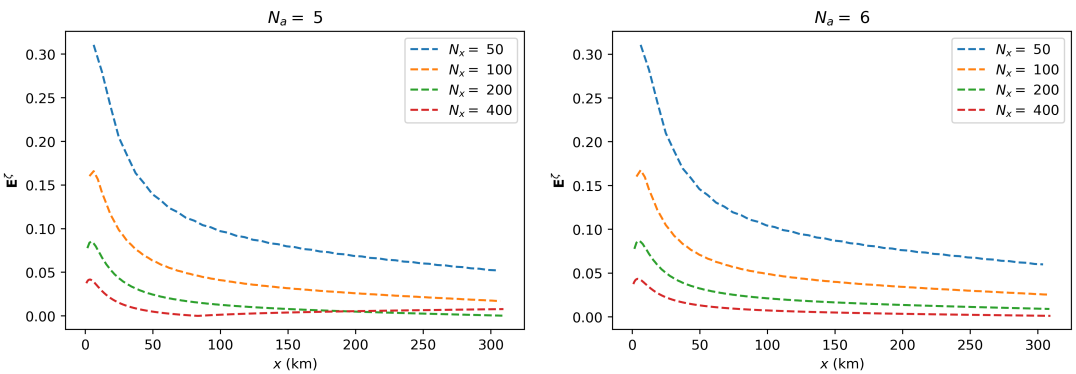


(c) $N_a = 5$. (d) $N_a = 6$.

Figure E.4: The relative error for the waterlevel as a function of $x$.

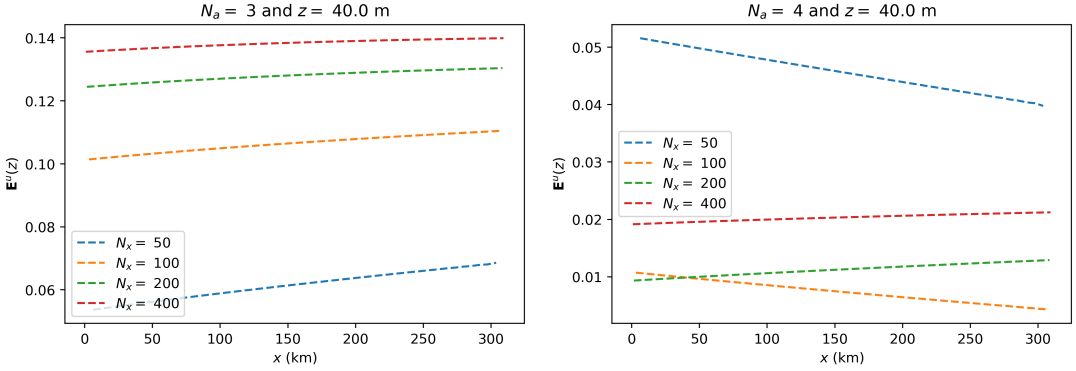


(a) $N_a = 3$.

(b) $N_a = 4$.

(c) $N_a = 5$.

(d) $N_a = 6$.

Figure E.5: The relative error for the longitudinal water velocity at $z = H/2$ as a function of $x$.

# Bibliography


Alaska, H. (2025). Foto van cook inlet — alaska handbook. Geraadpleegd op 8 september 2025.

Batchelor, G. K. (2000). *An introduction to fluid dynamics*. Cambridge university press.

Burchard, H., Bolding, K., Lange, X., and Osadchiev, A. (2023). Decomposition of estuarine circulation and residual stratification under landfast sea ice. *Journal of Physical Oceanography*, 53(1):57–80.

Chernetsky, A. (2012). Trapping of sediment in tidal estuaries.

Chernetsky, A. S., Schuttelaars, H. M., and Talke, S. A. (2010). The effect of tidal asymmetry and temporal settling lag on sediment trapping in tidal estuaries. *Ocean Dynamics*, 60(5):1219–1241.

Cushman-Roisin, B. and Beckers, J.-M. (2011). *Introduction to geophysical fluid dynamics: physical and numerical aspects*, volume 101. Academic press.

De Swart, H. (2009). Physics of coastal systems.

Guide, o. t. W. (2025). Alaska map – guide of the world. Geraadpleegd op 8 september 2025.

Hibler III, W. (1979). A dynamic thermodynamic sea ice model. *Journal of physical oceanography*, 9(4):815–846.

HISTORY, T. N. (2025). Afbeelding van history tv nederland website. Geraadpleegd op 8 september 2025.

Ianniello, J. P. (1977). Tidally induced residual currents in estuaries of constant breadth and depth.

Irrgang, A. M., Bendixen, M., Farquharson, L. M., Baranskaya, A. V., Erikson, L. H., Gibbs, A. E., Ogorodov, S. A., Overduin, P. P., Lantuit, H., Grigoriev, M. N., et al. (2022). Drivers, dynamics and impacts of changing arctic coasts. *Nature Reviews Earth & Environment*, 3(1):39–54.

Leppäranta, M. (2005). *The drift of sea ice*. Springer.

Mulherin, N. D., Tucker, W. B., Smith, O. P., Lee, W. J., et al. (2001). Marine ice atlas for cook inlet, alaska. Technical report.

Murray, A. B. (2003). Contrasting the goals, strategies, and predictions associated with simplified numerical models and detailed simulations. *Geophysical Monograph-American Geophysical Union*, 135:151–168.

Nieuwstadt, F. T., Westerweel, J., and Boersma, B. J. (2016). *Turbulence: introduction to theory and applications of turbulent flows*. Springer.

Overeem, I., Nienhuis, J. H., and Piliouras, A. (2022). Ice-dominated arctic deltas. *Nature Reviews Earth & Environment*, 3(4):225–240.

Pedlosky, J. (2013). *Geophysical fluid dynamics*. Springer Science & Business Media.

Pritchard, D. W. (1967). What is an estuary: physical viewpoint. American Association for the Advancement of Science.

Rozendaal, M. P. (2019). *An idealised morphodynamic model of a tidal inlet and the adjacent sea*. PhD thesis, Master's thesis, Delft University of Technology, Delft, Netherlands.

Schuttelaars, H. M., de Jonge, V. N., and Chernetsky, A. (2013). Improving the predictive power when modelling physical effects of human interventions in estuarine systems. *Ocean & coastal management*, 79:70–82.

Vasulkar, A. (2024). Arctic sea ice in tide models.